

Collagen 1 fibers and hypoxic tumor microenvironments in  
breast cancer and their effect on transport of molecules within  
the tumor matrix

Dissertation

zur Erlangung des Grades eines  
Doktors der Naturwissenschaften  
- Dr. rer. nat. -

dem Fachbereich 2  
Biologie/Chemie  
der Universität Bremen

2013

vorgelegt von

**Samata Kakkad**



Tag des Promotionskolloquiums: 23.10.2013

1. Gutachter: Prof. Dr. Dieter Leibfritz
2. Gutachter: Prof. Dr. Kristine Glunde



## Table of Contents

<b>Acknowledgement</b> .....	<b>9</b>
<b>Zusammenfassung</b> .....	<b>13</b>
<b>Chapter 1</b> .....	<b>19</b>
Introduction.....	19
The breast cancer epidemic.....	20
Hypoxia, the tumor microenvironment, the ECM and collagen I.....	23
Imaging modalities and quantification.....	27
<i>Second harmonic generation microscopy to characterize collagen I fibers</i> .....	28
<i>Optical imaging to detect hypoxia</i> .....	30
<i>Magnetic Resonance imaging</i> .....	32
<i>Magnetic Resonance imaging to characterize macromolecular transport</i> .....	33
<i>Co-registration of optical imaging and MRI data</i> .....	34
<i>Magnetic Resonance imaging to characterize water diffusion</i> .....	34
Thesis outline.....	37
<b>Chapter 2</b> .....	<b>51</b>
Hypoxic tumor microenvironments reduce collagen I fiber density.....	51
Abbreviations footnote.....	52
Abstract.....	53
Introduction.....	54
Materials and Methods.....	57
<i>Cell Lines and Tumor Models</i> .....	57
<i>SHG and Confocal Microscopy</i> .....	58
<i>Image and Statistical Analysis</i> .....	60
Results.....	62
Discussion.....	70
Acknowledgments.....	74
References.....	74

<b>Chapter 3 .....</b>	<b>83</b>
Collagen I fiber density increases in lymph node positive breast cancers in a pilot study .....	83
Abstract.....	84
Introduction.....	84
Materials and Methods.....	86
<i>Ethics Statement</i> .....	86
<i>Breast Cancer Specimens</i> .....	88
<i>SHG Imaging</i> .....	89
<i>Coll Fiber Quantification</i> .....	90
Results.....	93
Discussion .....	99
Conclusions.....	103
Declaration of Competing Interests .....	103
Authors' contributions.....	104
Acknowledgements and Funding.....	104
References.....	105
<b>Chapter 4 .....</b>	<b>113</b>
Hypoxic tumor environments exhibit disrupted collagen I fibers and low macromolecular transport .	113
Abbreviations footnote.....	114
Abstract.....	115
Introduction.....	116
Materials and Methods.....	118
<i>Ethics statement</i> .....	118
<i>Tumor model and inoculation</i> .....	118
<i>MRI acquisition</i> .....	119
<i>Fluorescence and multiphoton microscopy</i> .....	120
<i>Quantitative image analysis</i> .....	121
Results.....	124
Discussion .....	132
Acknowledgement .....	136
References.....	136

<b>Chapter 5 .....</b>	<b>141</b>
Collagen fibers mediate water diffusion and anisotropy.....	141
Abbreviation footnote .....	142
Abstract.....	143
Introduction.....	144
Methods.....	146
<i>Clinical Specimens</i> .....	149
<i>Breast Cancer Xenografts</i> .....	149
<i>SHG and Confocal Microscopy</i> .....	150
<i>Ex Vivo DTI Acquisition</i> .....	152
<i>In Vivo DTI Acquisition</i> .....	152
<i>Co-registration Strategy for Ex Vivo and In Vivo Localization Quantification</i> .....	153
Results.....	156
<i>Human Sample Ex Vivo Studies</i> .....	156
<i>Breast Cancer Xenograft Ex Vivo Studies</i> .....	159
<i>Breast Cancer Xenograft In Vivo-Ex Vivo Studies</i> .....	161
Discussion.....	164
Acknowledgements.....	166
<b>Curriculum vitae.....</b>	<b>172</b>
<b>List of publications.....</b>	<b>173</b>





## Acknowledgement

Firstly, I thank Prof. Dr. Dieter Leibfritz for accepting me under his guidance for the PhD program at the University of Bremen. It has been a wonderful experience working with him. Dr. Leibfritz has been very kind and a great tutor while discussing important aspects of this project. I thank Dr. Zaver Bhujwalla for providing me with the opportunity to work in her division at The Johns Hopkins University School of Medicine. She has been an amazing mentor and guide; inspiring me to work with self-confidence. I have gained a lot of experience and learnt so much from her that I would treasure. I thank Dr. Kristine Glunde for training me for SHG image acquisition at the homebuilt microscope. Kristine has always been encouraging; her attitude of exploring new ideas is very motivating. She is a great mentor to work with.

I am grateful to all my co-authors for their contribution in this work. Without their help and inputs, it would not have been possible to achieve such a high level of research and publish this work.

I would like to thank members of the University of Bremen, for being warm, friendly and so helpful. I would like to thank Dr. Markus Plaumann for his encouraging and helpful nature. He was very prompt in helping me even on a weekend. I would also like to mention Mrs. Marion Schilling for her help with all the paper work.

I would like to mention the ICMIC lab members at The Johns Hopkins University School of medicine. I thank Dr. Marie-France Penet, as when I first arrived at the ICMIC laboratory she trained me with the animal work in which I had no experience. It has been wonderful to work with her. I would like to mention Dr. Arvind Pathak, for his guidance in the macromolecular contrast agent project. I would like to mention Dr. Pedram Argani, for providing us with the human breast cancer biopsy samples for the lymph node study. He has being very helpful with the pathology sections. I would like to thank Dr. Jiangyang Zhang for his expertise and help for the DTI project. I would like to acknowledge Mr. Meiyappan Soliyapann and Dr. Alireza Akhbardeh for their computational expertise throughout the

thesis work. I would like to thank Mr. Desmond Jacob for helping me with the SHG imaging on the new Olympus system. I would like to thank and appreciate all efforts of Dr. Vadappuram Chacko with technical issues at the MRI system. I would like to thank Dr. Michael Jacobs for his advice, discussions, and encouragement. I would like to thank Mr. Gary Cromwell for maintaining all the cancer cell lines and tumor inoculations, without whom none of these experiments would have been possible. I would like to thank Mrs. Flonne Wildes for her ever ready helping nature, enthusiasm and help in monitoring tumor growth. I would like to thank Mrs. Tiffany Greenwood and Mrs. Yelena Mironchik for their help.

Among the other lab members from the ICMIC group, I would like mention here Dr. Balaji Krishnamachary. He has been the 'to go to person' whenever I had difficulty in my project. He always had time to answer and help clear all my doubts and queries. I do really appreciate his help. I would like to make a special mention of Dr. Lu Jiang. She has been more than a colleague, a friend, someone with whom I could discuss any problems I ran into. She has been a great motivating factor. I would like to thank our administrators at the The Johns Hopkins University. Mrs. Martha Seay has been absolutely wonderful and Mrs. Angela Wainwright has been very helpful and made dealing with paper work so easy.

I would like to thank my friends for their support and encouragement. I am sorry for being a spoiler for not having enough time for everyone; I thank them for being understanding. I would like to mention Dr. Khyati Shah, who has shared her experiences with me that have helped me a long way. I also cannot thank Mr. Kunal Doshi enough; for always supporting me and his belief in my ability to achieve my goals.

My family has always been incredibly supportive. I would like to thank my grandparents. I am thankful to my dad Mr. Mukesh Kakkad for motivating me through tough times and making me believe that nothing is impossible to achieve. Thanks mommy, Mrs. Bharati Kakkad for bearing my tantrums and for the love you gave me. She always believed that nature has its way of working things out for me. My little sister Dr. Kavita Kakkad has been my walking medical dictionary. Thanks for choosing your

medical program in the same city and living with me so I do not get homesick. I would like to thank my aunts and uncles who have always been very supportive. I would like to thank my parents' in-law Mr. Pradeep Bhatia and Mrs. Pratima Bhatia for all their love and care. They have been very encouraging and supportive. I also thank my sister in-law Mrs. Sonam Bhatia Mukherjee for her always encouraging sweet kind words of support. Finally, I would like to thank my fiancé Mr. Sahil Bhatia for his love and support. He has been my strength and greatest source of encouragement. He has been by my side during my ups and downs. Thanks for being my punching bag when I was frustrated. Thank you very much for being by my side and not giving up on me.

Lastly and definitely not the least, I thank the reader for going through my thesis.



## **Zusammenfassung**

Mehr als 90% der Mortalität durch Brustkrebs wird durch Metastasen verursacht und nicht durch den primären Tumor in der Brust [1]. Es ist wichtig, die Mechanismen der Metastasenbildung aufzuklären und dadurch Biomarker für metastasierten Brustkrebs zu identifizieren, die dabei helfen können, Patienten besser zu behandeln. Krebszellen überleben unter Extrembedingungen in der Tumor-Mikroumgebung (TMU), die durch Hypoxie, einen sauren extrazellulären pH Wert und Nährstoffmangel charakterisiert ist, und sie können in dieser feindlichen Umgebung wachsen [2]. Krebszellen kommunizieren kontinuierlich mit der sie umgebenden extrazellulären Matrix (EZM) durch Integrine, die dann bei der Metastasenbildung mitwirken [3]. Kollagen I (Koll1) Fasern sind eine wesentliche strukturelle Komponente der EZM im Brustkrebs [4]. Eine erhöhte Koll1 Faserdichte verursacht den Beginn des Tumorwachstums, die Fortschreitung des Krebses und die Metastasenbildung [5]. Sternförmig ausgerichtete Koll1 Fasern sind ein prognostischer Marker für die Aggressivität des Tumors. Es wurde gezeigt, dass Tumorzellen sich entlang dieser sternförmig ausgerichteten Fasern fortbewegen [6]. Wenn ein Tumor wächst, kann es passieren, dass die Gefäßversorgung des Tumors vorübergehend nicht mehr mit dem Tumorwachstum mithalten kann und sich dadurch hypoxische Regionen im Tumor bilden [7]. Hypoxische Tumor-Milieus sind dafür bekannt, dass sie gegen Behandlungen resistent sind und dass sie dem Krebs einen aggressiven Phänotyp verleihen [8].

Im Mittelpunkt dieser Doktorarbeit steht das Verstehen der Rolle der Koll1 Fasern, die die Hauptkomponente der EZM im Tumor bilden, und ihr Zusammenhang mit der

Metastasenbildung, der Hypoxie, dem makromolekularen Transport, der Wasserdiffusion und der fraktionalen Anisotropie. Die Untersuchungen in dieser Doktorarbeit wurden mit klinischen Brustkrebsproben und menschlichen Brustkrebszellen, die als Xenograft-Tumore in immungeschwächten Mäusen wuchsen, durchgeführt. Diese Xenograft-Tumore wurden gentechnisch dahingehend verändert, dass sie unter hypoxischen Bedingungen fluoreszieren. Es wurde eine multimodale Bildgebung benutzt, bei der optische und kernspintomographische Methoden kombiniert wurden. Koll1 Fasern wurden dabei durch eine mikroskopische Methode, die die zweite Oberschwingung der Koll1 Fasern misst, sichtbar gemacht. Dies wurde mit optischer Bildgebung zur Detektion von fluoreszierenden, hypoxischen Tumorregionen kombiniert. Dies wurde wiederum entweder mit dynamischer, kontrastmittelverstärkter Kernspintomographie kombiniert, um die funktionelle Rolle der Koll1 Fasern im makromolekularen Transport zu charakterisieren, oder mit Diffusions-Tensor-Bildgebung, um die Funktion der Koll1 Fasern während der Wasserdiffusion im Tumor zu beschreiben.

Wir haben beobachtet, dass Koll1 Fasern innerhalb des Tumors heterogen verteilt sind, wobei eine geringere Faserdichte in Tumorregionen mit hypoxischen Bedingungen festgestellt wurde im Vergleich zu normoxischen Regionen im Tumor (Kapitel 2) [9]. Für diese Untersuchungen wurden die oben beschriebenen Brustkrebs-Xenograft-Modelle verwendet. Primärtumorproben von Patientinnen mit Metastasen in den Lymphknoten hatten eine wesentlich höhere Koll1 Faserdichte als Proben von Patientinnen, deren Krebs sich noch nicht bis zu den Lymphknoten ausgebreitet hatte (Kapitel 3) [10]. Wir haben auch die funktionellen Aspekte der unterschiedlichen Koll1 Faserausprägungen in normoxischen und hypoxischen Regionen im oben beschriebenen MDA-MB-231 Brustkrebs-Xenograft-Modell untersucht (Kapitel 4) [11]. In

hypoxischen Regionen mit niedriger Faserdichte herrschte ein geringerer, makromolekularer Transport vor, was, im Vergleich mit normoxischen Regionen mit hoher Koll Faserdichte in diesem Xenograft Modell, durch weniger Dränage und weniger Zufluss von makromolekularem Kontrastmittel innerhalb des Tumors nachgewiesen wurde. Diese hypoxischen Regionen waren ebenfalls durch eine erniedrigte Wasserdiffusion und geringere Anisotropie gekennzeichnet [11, 12]. Hohe Faserdichten korrelierten mit einer erhöhten Wasserdiffusion und Faser-Anisotropie in Brustkrebspräparaten von Patientinnen [12].

Die Studien dieser Doktorarbeit haben dazu beigetragen, strukturelle und funktionelle Veränderungen, die im Tumor in Koll Fasern unter dem Einfluss hypoxischer Bedingungen entstehen, in klinischen Brustkrebspräparaten und in vorklinischen Brusttumor-Xenograft-Modellen aufzuklären. Diffusions-Tensor-Bildgebung wurde als mögliche, nicht-invasive Bildgebungsmethode geprüft, um Koll Fasern indirekt, über ihre Auswirkungen auf die Wasserdiffusion, zu detektieren. Die Daten, die in dieser Doktorarbeit präsentiert wurden, könnten in der Zukunft bei der Behandlungsplanung von Brustkrebspatientinnen und bei der Überwachung der Medikamentenverabreichung in diesen Patientinnen helfen.

## **Literatur**

1. Saxe, C.K. *Unlocking the Mysteries of Metastasis*. 2013 [cited 2013; Available from: <http://www.cancer.org/cancer/news/expertvoices/post/2013/01/23/unlocking-the-mysteries-of-metastasis.aspx>.

2. Stasinopoulos, I., M.F. Penet, Z. Chen, S. Kakkad, K. Glunde, and Z.M. Bhujwalla (2011). Exploiting the tumor microenvironment for theranostic imaging. *NMR Biomed.* 24(6): 636-47.
3. Wolf, K. and P. Friedl (2009). Mapping proteolytic cancer cell-extracellular matrix interfaces. *Clin Exp Metastasis.* 26(4): 289-98.
4. Lochter, A. and M.J. Bissell (1995). Involvement of extracellular matrix constituents in breast cancer. *Semin Cancer Biol.* 6(3): 165-73.
5. Provenzano, P.P., D.R. Inman, K.W. Eliceiri, J.G. Knittel, L. Yan, C.T. Rueden, J.G. White, and P.J. Keely (2008). Collagen density promotes mammary tumor initiation and progression. *BMC Med.* 6: 11.
6. Provenzano, P.P., K.W. Eliceiri, J.M. Campbell, D.R. Inman, J.G. White, and P.J. Keely (2006). Collagen reorganization at the tumor-stromal interface facilitates local invasion. *BMC Med.* 4: 38.
7. Jain, R.K. (1988). Determinants of Tumor Blood-Flow - a Review. *Cancer Research.* 48(10): 2641-2658.
8. Brown, J.M. and W.R. William (2004). Exploiting tumour hypoxia in cancer treatment. *Nature Reviews Cancer.* 4(6): 437-447.
9. Kakkad, S.M., M. Solaiyappan, B. O'Rourke, I. Stasinopoulos, E. Ackerstaff, V. Raman, Z.M. Bhujwalla, and K. Glunde (2010). Hypoxic Tumor Microenvironments Reduce Collagen I Fiber Density. *Neoplasia.* 12(8): 608-617.
10. Kakkad, S.M., M. Solaiyappan, P. Argani, S. Sukumar, L.K. Jacobs, D. Leibfritz, Z.M. Bhujwalla, and K. Glunde (2012). Collagen I fiber density increases in lymph node positive breast cancers: pilot study. *Journal of Biomedical Optics.* 17(11).



11. Kakkad, S.M., M.-F. Penet, A. Akhbardeh, A.P. Pathak, M. Solaiyappan, V. Raman, D. Leibfritz, K. Glunde, and Z.M. Bhujwalla (2013). Hypoxic tumor environments exhibit disrupted collagen I fibers and low macromolecular transport. *PLoS One*. 12;8(12)
12. Kakkad, S.M., J. Zhang, A. Akhbardeh, D. Jacob, M. Solaiyappan, M. Jacobs, V. Raman, D. Leibfritz, K. Glunde, and Z.M. Bhujwalla (Manuscript in preparation). Collagen fibers influence water diffusion and anisotropy. *JNCI*.



# Chapter 1

---

## Introduction

The work presented in this thesis represents a culmination of four years of research work focused on understanding the role of collagen I (Col1) fibers, a major component of the tumor extracellular matrix. We have investigated the relationship of Col1 fibers with metastasis, hypoxia, macromolecular transport, water diffusion and fractional anisotropy using clinical breast cancer specimens and human breast cancer xenografts genetically engineered to fluoresce under hypoxia. In the subsequent sections we have provided brief introductory overviews of the rationale for our studies, which have been either published or submitted as four separate papers.

### **The breast cancer epidemic**

The incidence of breast cancer has shown a three-fold increase over the past 30 years [1]. Based on forecasted changes in population demographics at the current global cancer rate the incidence of breast cancer is expected to show a further two-fold increase by 2030, reaching epidemic proportions [1]. While mortality rates are decreasing slightly in Western countries, breast cancer continues to have a devastating effect in terms of mortality and quality of life, especially in the case of recurrent or metastatic disease. Local or regional recurrences and metastatic disease have an unfavorable prognosis, and distant metastases are mostly treated with palliative rather than curative approaches. The 5-year survival rate of breast cancer patients drops from 96% to 75% with regional spread, and to 20% with distant spread [2], with axillary lymph node-positive patients more likely to develop distant metastasis. It is therefore imperative to search for new possibilities in the etiology, progression and treatment of breast cancer, and to understand causes for recurrence and metastasis. In 2013, 232,000 female and 2,240 male new cases were detected with breast cancer in the USA alone, with 39,620 female and 410 male

deaths (National Cancer Institute – NCI) [3]. The two most common types of breast cancer are lobular carcinomas, which arise from the milk-producing lobules and ductal carcinomas, which arise from the milk-carrying ducts. A summary of breast cancer staging based on tumor size and lymphatic and metastatic spread is outlined in Table 1 [3].

**Table 1:** Summary of breast cancer staging

Staging	Description
Stage 0	The cancer is confined to its tissue. Ductal carcinoma in situ (DCIS) – cancer confined to the breast ductal lining; lobular carcinoma in situ (LCIS) – cancer confined to the lobules of the breast; Paget disease – cancer confined to the nipple.
Stage IA	The tumor is 2 cm or smaller and has not spread outside the breast.
Stage IB	Cluster of tumor no more than 2 mm is found in the lymph node with either no tumor found in the breast or tumor less than 2 cm in the breast.
Stage IIA	<ol style="list-style-type: none"> <li>1. Cancer is larger than 2 mm and found in 1-3 axillary lymph nodes or lymph nodes near the breastbone with either no tumor in the breast or tumor smaller than 2 cm; OR</li> <li>2. Tumor is larger than 2 cm but smaller than 5 cm and has not spread to the lymph nodes.</li> </ol>
Stage IIB	<ol style="list-style-type: none"> <li>1. Breast tumor is larger than 2 cm but smaller than 5 cm and small clusters of cancer of less than 2 mm are found in the lymph nodes; OR</li> <li>2. Breast tumor is larger than 2 cm but smaller than 5 cm with cancer spread to 1-3 axillary lymph nodes or to lymph nodes near breastbone; OR</li> <li>3. Breast tumor is larger than 5 cm and cancer has not spread to the lymph nodes.</li> </ol>
Stage IIIA	<ol style="list-style-type: none"> <li>1. No tumor is found in the breast or the tumor is of any size with 4-9 axillary lymph nodes or lymph nodes near the breastbone; OR</li> <li>2. Tumor is larger than 5 cm and small cluster of cancer less than 2 mm is found in the lymph nodes; OR</li> <li>3. The tumor is larger than 5 cm and cancer has spread to 1-3 axillary lymph nodes or lymph nodes near breastbone.</li> </ol>
Stage IIIB	The cancer can be of any size and has spread to the chest wall and/or breast skin and also may have spread either to up to 9 axillary lymph nodes or lymph nodes near breastbone.
Stage IIIC	No tumor or breast tumor of any size with cancer spread to the breast skin with swelling and/or spread to the chest wall, and has also spread to 10 or more axillary lymph nodes; OR to lymph nodes above or below collarbone; OR axillary lymph node and lymph node near breastbone.
Stage IV	Cancer has spread to other parts of the body.

Early detection of breast cancer increases the chances of detecting the primary tumor prior to metastatic dissemination. Detection at later stages increases the incidence of recurrence, which is associated with poor prognosis. Metastasis is a leading cause of mortality from breast cancer. Understanding the mechanisms that contribute to or drive metastatic dissemination in breast cancer is of critical importance in reducing mortality from this disease. In the **second paper** (Chapter 3) we have focused on understanding the role of Col1 fibers in the metastatic dissemination of breast cancer.

A typical course of treatment includes surgical removal of the breast tumor, followed in many cases by radiation- or chemotherapy or both. In breast cancers that overexpress estrogen receptors (ER), anti-estrogen therapy is commonly given to prevent tumor recurrence from any remaining residual cancer cells [4]. Targeted therapy comprises a different group of treatments that may be given to treat breast cancer. Targeted therapy specifically targets cancer cells by selectively blocking a pathway or receptor that is exclusively expressed or activated in cancer cells, such as for example targeting of the human epidermal growth factor receptor 2 (HER2) receptor in breast cancer [5]. A subset of breast cancers that do not express ER, progesterone receptors (PR) or HER2 are commonly referred to as triple-negative breast cancers. Triple-negative breast cancers are the most difficult to treat. Conventional chemotherapy such as treatment with anthracyclines, taxanes, or platinum-based agents, which non-specifically inhibit cell growth of fast proliferating cells [6] is the primary option for treating triple-negative and late stage breast cancers. Conventional chemotherapy results in deleterious side effects due to normal tissue damage. Another problem with treating breast cancers is that chemotherapeutic or targeted agents are often not effectively delivered within the tumor due to the abnormal and

chaotic vasculature frequently found in tumors [7]. Such abnormal vascular and lymphatic networks in tumors impose additional physiological abnormalities in the tumor microenvironment, such as hypoxia, an acidic extracellular pH (pHe), and an increased interstitial pressure [8]. These changes are often observed in addition to metabolic alterations in breast tumors such as an altered glucose, glutamine, choline, and glycine metabolism [9-12].

### **Hypoxia, the tumor microenvironment, the ECM and collagen I**

The existence of hypoxia in tumors and its implications for failure of radiation therapy was predicted by Thomlinson and Gray in 1955 [13], based on observations that necrosis in human lung carcinomas occurred at approximately 150  $\mu\text{m}$ , which is the calculated diffusion distance of oxygen from the nearest capillary. Six decades later, hypoxia and the hypoxia inducible factors (HIF-1 and -2) are being associated with the transcriptional activation of an ever-increasing number of genes that regulate several phenotypic characteristics of cancer [14]. Tumor hypoxia can be diffusion-limited or chronic, or can arise acutely from vascular collapse [15, 16]. Most treatments, especially radiation therapy, result in reoxygenation [17, 18].

HIF-1 is a heterodimeric protein that consists of a constitutively expressed  $\beta$ -subunit and an oxygen-dependent  $\alpha$ -subunit that is rapidly degraded through polyubiquitination and proteasomal degradation under well-oxygenated conditions [19]. Under hypoxic conditions, HIF-1 $\alpha$  or HIF-2 $\alpha$  undergo heterodimerization with HIF-1 $\alpha$  and bind to hypoxia response elements (HRE) to activate the transcription of several target genes [20]. These target genes

control angiogenesis, cell survival, resistance to chemo- and radiation therapy, metabolism, pH regulation, invasion and metastasis, increased genetic instability, and de-differentiation [14, 21].

The tumor microenvironment is critically important in the evolution of the malignant phenotype [22]. Cancer cells have a remarkable ability to adapt to their environment [23]. The extracellular matrix (ECM), cancer associated fibroblasts (CAFs), adipocytes, pericytes, multiple immune cells such as tumor-associated macrophages (TAMs), and vascular and lymphatic endothelial cells (**Figure 1**) that surround and support cancer cells, comprise the tumor microenvironment [24]. Cancer cells' genomic plasticity and their interaction with the tumor microenvironment give rise to several lethal phenotypic traits to survive and adapt to hostile physiological environments such as hypoxia, acidic pH, and substrate deprivation [24]. In addition, cancer cells have the ability to survive lethal treatments [24]

The tumor microenvironment interacts with cancer cells and plays a dual role by creating tumor-promoting and tumor-restricting environments [24, 25]. Cancer cells recruit myofibroblasts, CAFs and adipocytes, TAMs, which cause tumor-associated changes in the ECM [24, 25]. Unlike normal myofibroblasts in wound healing, in pathology their existence persists leading to fibrosis by excessive production of collagen [26]. CAFs support tumor growth by secreting vascular endothelial growth factor (VEGF), fibroblast growth factors (FGFs), platelet-derived growth factor (PDGF), and promoting angiogenesis [27]. Cancer associated adipocytes (CAAs) acquire a fibroblast-like shape and have been shown to stimulate cancer cell migration [28]. TAMs are recruited in cancer in response to inflammation and promote angiogenesis by



secreting VEGF, FGFs, PDGF, and collect in hypoxic regions of the tumor [27]. During invasion, cancer cells are embedded within this complex stroma, and both cell-cell and cell-matrix adhesions by integrins, cadherins, and can regulate tumor dissemination by collective cell migration [24, 29]. Cancer cells secrete degrading enzymes such as cysteine, aspartic and serine proteases, and matrix metalloproteinases to degrade and remodel the ECM, which enables their invasion into the surrounding tissue [24].

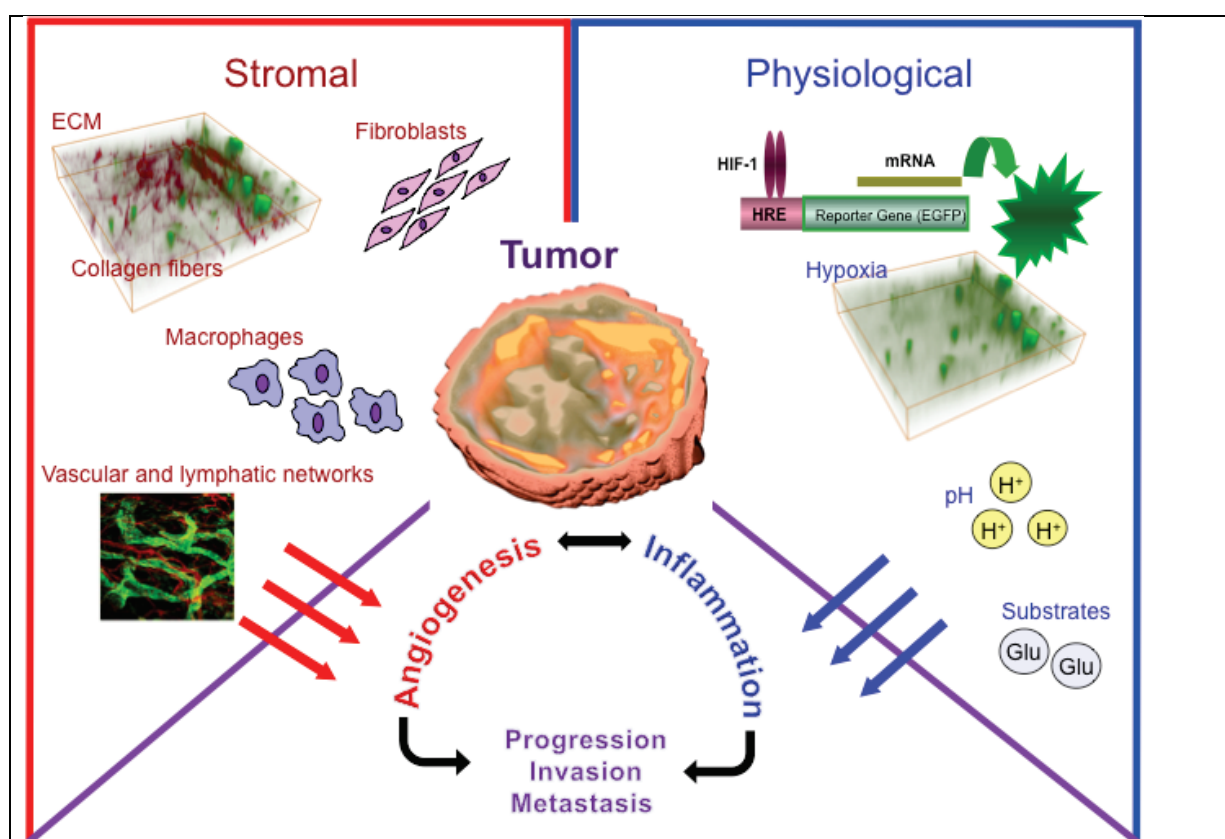


**Figure 1:** Schematic to show the different components of the tumor microenvironment. The image of collagen 1 fibers overlaid with hypoxic regions was obtained from an MDA-MB-231 tumors expressing enhanced green fluorescent protein (EGFP) under control of HREs. Collagen I fiber images were acquired with second harmonic generation (SHG) microscopy. The 3D display of the tumor is a parametric image of extracellular transport of a macromolecular contrast agent. The vascular and lymphatic network image is from [http://www.imm.ox.ac.uk/wimm-research/mrc-human-immunology-unit/david-jackson/fig3.jpg/image\\_preview](http://www.imm.ox.ac.uk/wimm-research/mrc-human-immunology-unit/david-jackson/fig3.jpg/image_preview).

From: Stasinopoulos, Penet, Chen, Kakkad, Glunde and Bhujwala; NMR in Biomedicine, 2011[24]

Tumors actively secrete proteolytic enzymes that continuously remodel the ECM, which is comprised of collagens, glycoproteins and proteoglycans [30, 31]. Lysosomal cathepsins proteolytically degrade the ECM both intracellularly following endocytosis of ECM components or extracellularly following cathepsin secretion, which has a profound effects on tumor ECM components such as fibrillar Col1 [32], laminin [33], and fibronectin [24, 34, 35].

Col1 fibers are a major structural component of the ECM in breast cancer and play an important role for drug delivery in tumors [36, 37]. There are more than 20 types of collagen proteins, but Col1 is the most abundant collagen in the human body [38]. Col1 fibers belong to the fibrillar collagen family and their main role is to provide strength and support to tissues [38]. Col1 fiber synthesis is a versatile multi-step process, which starts inside the cell with the formation of the pro-collagen I triple helix from the Col1A1 and Col1A2 genes [39]. Pro-collagen I is secreted and converted to tropocollagen, which in turn self-assembles and is cross-linked to form mature Col1 fibers. The final size of mature Col1 fibers can be up to 500 nm by 1 cm [40]. Malignant breast cancers are characterized by significantly higher Col1 fiber density and altered Col1 fiber architecture [41]. High mammary Col1 density was shown to cause mammary tumor initiation, progression and metastasis [41]. Overexpression of integrins such as  $\alpha 2\beta 1$  integrin facilitates breast cancer cell attachment to Col1 fibers [42].

In the **second paper** (Chapter 3), we have applied second harmonic generation (SHG) microscopy to detect differences in Col1 fibers in hypoxic *versus* normoxic tumor regions, using human breast tumor xenografts stably expressing enhanced green fluorescent protein (EGFP)

under the control of HREs in the promoter of VEGF [43]. Hypoxic tumor regions were found to contain fewer Col1 fibers than normoxic tumor regions [44]. Magnetic resonance imaging (MRI) of the macromolecular contrast agent (MMCA) albumin-GdDTPA can be used to characterize the extravascular transport of macromolecules through the ECM of solid tumors *in vivo* [45, 46]. Macromolecular transport can be characterized by quantifying tumor regions, from which the MMCA is either draining, or in which it is pooling [45]. With this method, it was possible to detect an increased drainage in more invasive breast tumors that had a greater capacity to degrade the ECM [46]. In the **third paper** (Chapter 4), we have related macromolecular transport through the ECM in tumors to Col1 fiber volume and distribution in these tumors, to characterize the functional impact of Col1 fiber patterns in normoxic and hypoxic tumor regions [47]. Finally, we have further sought to expand our understanding of the relationship between transport through the ECM and Col1 fibers by investigating the relationship between Col1 fibers and water diffusion and anisotropy in the **fourth paper** (Chapter 5) in this thesis [48].

### **Imaging modalities and quantification**

The work presented here has integrated optical imaging with magnetic resonance imaging to take a combined structural, molecular and functional approach in understanding the role of Col1 fibers in metastatic dissemination, the relationship between hypoxia and Col1 fibers, and the role of Col1 fibers in macromolecular transport and water diffusion.

*Second harmonic generation microscopy to characterize collagen I fibers.* Second harmonic generation (SHG) microscopy is a valuable tool for understanding the remodeling of the Col1 fiber matrix in intact tissue [49]. SHG is a nonlinear optical process that requires a molecule without a center of symmetry to produce a signal [50]. These molecules exhibit optical  $\chi^2$  nonlinearity when the exciting light is polarized non-linearly, and based on the phase matching, it gives rise to twice the incident frequency (half the wavelength) referred to as the second harmonic [51]. High depth penetration (up to  $\sim 0.50$  mm) with minimum photobleaching and phototoxicity is achieved by SHG microscopy [52]. SHG is an intrinsic signal and does not require any external labeling. The SHG excitation wavelength range is 766 nm to 1,064 nm [53]. Col1 fibers have a molecular structure that lacks a center of symmetry and can give rise to a second harmonic signal. Therefore, Col1 fibers can be detected from fresh tissue sections or even *in vivo* via an intra-vital endoscope. In our studies, to detect Col1 fibers, we have used a 25 $\times$  lens to acquire z-stacks of approximately 100  $\mu\text{m}$  thickness with a z-interval of approximately 5  $\mu\text{m}$ . During this thesis work, we have developed an in-house MATLAB (MATLAB 7.4.0, The MathWorks, Natick, MA) code for quantifying the Col1 fiber distribution (Chapter 2). Parameters such as percent fiber volume and inter-fiber distance were calculated to quantify Col1 fiber content and distribution [44]. Percent fiber volume was calculated as described in equation 1.

$$\text{Percent fiber volume} = \frac{\text{Total number of fiber voxels in a FOV}}{\text{Area of FOV}} \times 100 \quad [\text{Equation 1}]$$

Inter-fiber distance was calculated by measuring the Euclidean distance from every non-fiber voxel to the nearest fiber [44]. The equation for calculating the Euclidean distance in a three-dimensional matrix between two points  $p$  and  $q$  is given by equation 2 [54].

$$d(p, q) = \sqrt{(p_1 - q_1)^2 + (p_2 - q_2)^2 + (p_3 - q_3)^2} \quad \text{[Equation 2]}$$

The resulting distance matrix maps the distance that represents the space in between Coll fibers. The percent fiber volume and inter-fiber distance parameters of fiber quantification were compared in hypoxic *versus* normoxic tumor regions [44]. We also developed a texture analysis technique to understand the fiber patterns seen in these heterogeneous tumor microenvironments (see Chapter 5). We employed statistics based texture analysis to calculate the co-occurrence matrix [55]. The co-occurrence matrix calculates the co-occurring gray-level value at a defined distance and direction and is given by equation 3 [56].

$$C_{\Delta x, \Delta y}(i, j) = \sum_{p=1}^n \sum_{q=1}^m \begin{cases} 1, & \text{if } I(p, q) = i \text{ and } I(p + \Delta x, q + \Delta y) = j \\ 0, & \text{otherwise} \end{cases} \quad \text{[Equation 3]}$$

In equation 3,  $C$  represents the co-occurrence matrix,  $I$  is the image of size  $(m \times n)$ ,  $i$  and  $j$  are the gray level image intensities,  $p$  and  $q$  are the spatial positions, and  $\Delta x$  and  $\Delta y$  are the offsets defined by distance and direction at which the gray level is computed [56]. To derive some interpretable features from this large co-occurrence matrix, Robert Haralick in 1973 extracted

features today known as the Haralick texture features [57] that are calculated from the 2D histogram of the image, also referred to as the co-occurrence matrix. Haralick features include energy, entropy, correlation, contrast, variance, sum mean, inertia, cluster shade, cluster tendency, homogeneity, max probability, inverse variance and angular second moments [57]. All feature images were displayed and features that did not differentiate between the varying fiber patterns were eliminated from further analysis. The fuzzy c-mean clustering technique [58] was used to cluster different fiber textures into different categories such as straight fiber texture, mixed fiber texture, and wavy fiber texture.

*Optical imaging to detect hypoxia.* To detect hypoxia by optical fluorescence imaging, we have generated human breast and prostate cancer cells that express enhanced green fluorescent protein (EGFP) or red fluorescent protein (RFP) under hypoxic conditions as a hypoxia-inducible factor 1 (HIF-1)–driven hypoxia sensor. The cancer cells were stably transfected with a construct that contains five copies of the hypoxia response element (HRE) from the promoter of the human VEGF-A gene ligated to the complementary DNA of EGFP or RFP, which produced MDA-MB-231–5HRE-EGFP (Chapter 2) or MDA-MB-231-HRE-RFP (Chapters 4, 5) and PC-3–5HRE-EGFP (Chapter 2) as previously described [43, 59]. In brief, the HIF- $\alpha$  subunit is unstable in the presence of oxygen and eventually proteolysis, but under hypoxic conditions, the HIF- $\alpha$  subunit stabilizes and dimerizes with its  $\beta$  subunit to form stabilized HIF, which then binds HRE sites. This binding of HIF to HRE sites acts as a transcriptional activator of all genes in whose promoter sequence the HREs can be found. So when HIF binds to the HRE sites in the above-mentioned cell lines, the expression of EGFP or RFP is transcriptionally activated and these cells start fluorescing in green or red, respectively, under hypoxic conditions [60]. The advantage of

using EGFP is that it is a long-lived protein and can be used for high-resolution imaging [61]. EGFP is excited at wavelengths of 450 to 490 nm and emits at 500 nm to 510 nm. In our first paper, we performed our studies using the MDA-MB-231-5HRE-EGFP and PC-3-5HRE-EGFP cancer cell lines (Chapter 2, [38]).

Biological tissues contain melanin, oxyhemoglobin, deoxyhemoglobin, and water, which have a high optical absorption for wavelengths below 650 nm, while water also has a high optical absorption for wavelengths above 900 nm [62]. Wavelengths between 650 nm and 900 nm are known to have the least tissue absorption and are best suited for imaging optically labeled dyes, called the optical imaging window or the therapeutic window (Figure 2, [63, 64]). With a higher wavelength as compared to EGFP [65], the tdTomato fluorescence signal would give a better depth penetration with excitation wavelengths of 543 nm and emission wavelengths of 570 nm to 620 nm [44, 47, 48], which are closer to the optical imaging window of low tissue absorption. TdTomato has a higher quantum yield of 0.69 as compared to other fluorescent proteins in the red wavelength range as well as EGFP (quantum yield = 0.60) [65]. We performed our studies in our third and fourth paper using the MDA-MB-231-HRE-RFP breast cancer cell line, which expresses the tdTomato RFP (Chapters 4, 5).

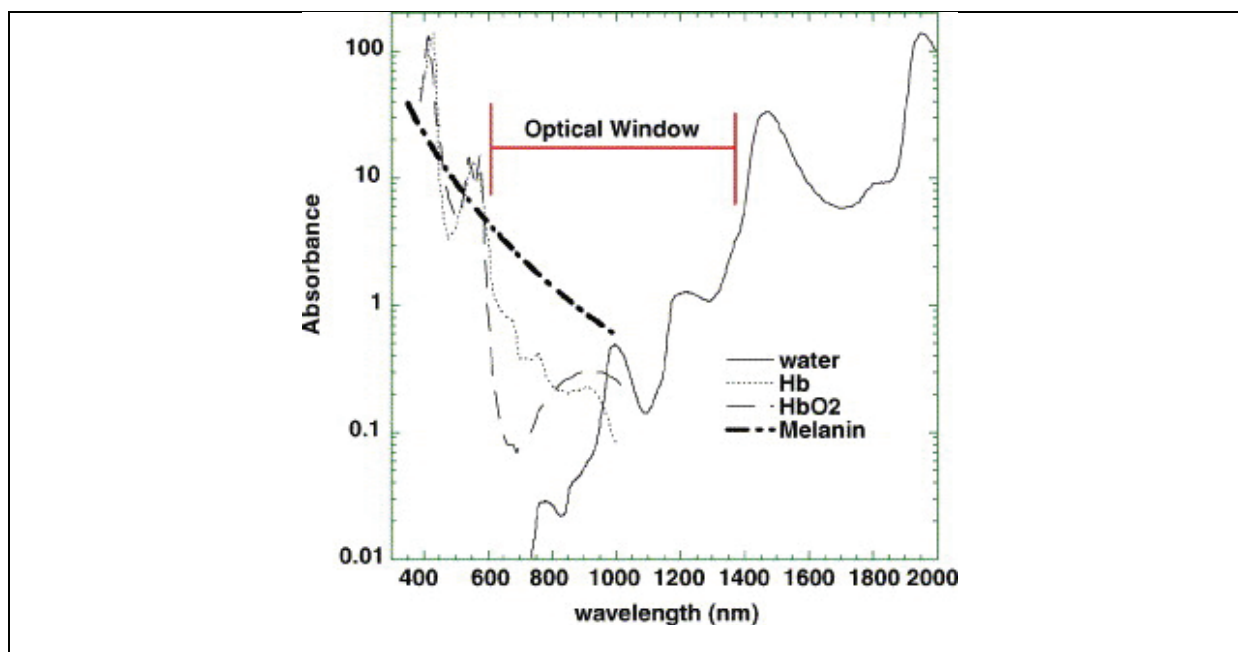


**Figure 2:** Optical window in tissue. Absorption spectra of important tissue chromophores such as water, oxy- and deoxyhemoglobin and melanin are plotted on a logarithmic scale. From: Mechanisms in photodynamic therapy: part one—photosensitizers, photochemistry and cellular localization. Ana P. Castanoa, b, Tatiana N. Demidovaa, c, Michael R. Hamblin, PhD [64].

*Magnetic Resonance imaging.* Magnetic resonance imaging (MRI) is a noninvasive imaging modality routinely used in the clinical setting for cancer diagnoses and treatment monitoring [66]. As a research imaging modality, it non-invasively helps understand tumor architecture and phenotype characteristics, which can easily be translated into the clinic [67]. MRI provides multiple anatomical parameters such as T1-weighted images, T2-weighted images, and proton density (PD) images, as well as functional parameters such as vascular volume, vascular permeability surface area product, interstitial fluid transport parameters and water diffusion. In principle, a radiofrequency (RF) pulse is applied to excite nuclear spins in the molecules that comprise the tissue to a higher energy level in the presence of a uniform, static magnetic field. The nuclear spins undergo relaxation to initial energy levels when the RF pulse is turned off and in the process emit RF signal that is detected as an MRI signal [68]. The detected MR signal



describes characteristic tissue properties since its signal strength depends on the concentration of the nuclear spins and the magneto-chemical environment of the excited nuclei in a given magnetic field [68]. MRI has the ability to give 3D high-resolution anatomical images from intrinsic contrast mechanisms such as T1 and T2.

*Magnetic Resonance imaging to characterize macromolecular transport.* To study functional effects by MRI, we intravenously injected a macromolecular contrast agent (MMCA) in breast cancer bearing mice and acquired MR images over time at regular intervals to study the delivery of the MMCA to the tumor and its wash out, which is an imaging technique referred to as dynamic contrast enhanced MRI (DCE-MRI). Different DCE-MRI models have been developed, and a model developed by Pathak *et al* [45] was used in this thesis, which is described in detail in Chapter 4. Briefly, images were acquired in two “phases” corresponding to the biphasic kinetics of the macromolecular contrast agent (MMCA) [45], which starts with the “early phase” acquisition and ends with the “late phase” acquisition. The initial 30 minutes of “early phase” acquisition included a pre-contrast image and post-contrast images, which were repeatedly acquired every 5 minutes [45]. This “early phase” acquisition was processed to characterize tumor vascular parameters since the contrast agent was confined within the vascular vessels during this time [45]. Tumor vascular parameters such as vascular volume (VV) and permeability surface area product (PS) were calculated from the “early phase” acquisition [45]. The drainage of macromolecules in and around tumors either by convection or by the lymphatics is a slow event [45]. Hence, the second block of MRI data referred to as the “late phase” was acquired for up to 123 minutes post-contrast [45]. The “late phase” acquisition was used to characterize the interstitial transport parameters through the ECM [45]. Transport parameters

calculated included the number of draining and pooling voxels, draining and pooling rates, and exudate volumes (see Chapter 4) [45, 46, 47]. MRI quantification analysis was done using software written in house, which was programmed in IDL (ITT Exelis Visual Information Solutions, VA USA) and AFNI (NIH software).

*Co-registration of optical imaging and MRI data.* To combine the DCE-MR images, hypoxia images and Coll fiber distribution, we first co-registered the MR images and  $1\times$  optical images to calculate transport parameters in hypoxic and normoxic regions of interests (ROIs). Details of this analysis are described in Chapter 4. Following MRI, the tumor was excised and carefully sliced, keeping the orientation as it was in the MRI scanner. Optical images were co-registered to the MR images using affine transformation [69]. The registration error was calculated by statistical dice similarity index [70]. The co-registered fluorescence images were masked to calculate the DCE-MRI parameters in hypoxic and normoxic regions. The Coll fiber distribution images were in turn co-registered by affine transformation to the optical images that were already co-registered to the MR images. This co-registration and co-localization analysis was performed in MATLAB 7.4.0 (The MathWorks, Natick, MA). A two tailed t-test was performed using Microsoft Office Excel 2010 and  $p$ -values of  $< 0.05$  were considered to be significant (see Chapter 4).

*Magnetic Resonance imaging to characterize water diffusion.* Diffusion tensor imaging (DTI) is an MRI technique where microscopic tissue structures are revealed by mapping the water diffusion [71]. Water movement is detected using MR, by adding two diffusion sensitizing gradients (also called the diffusion gradients) to the classical spin echo MRI sequence. The first

diffusion gradient dephases water molecules and the second diffusion gradient is applied to rephase these water molecules. Ideally, if there is no water movement within the time laps of these two gradient pulses, a perfect rephasing of the MR signal would be achieved, but due to thermal water motion (or Brownian motion) there is a loss in the rephased MR signal [71]. This loss in the MR signal is a measure of water diffusion, and the diffusion coefficient (D) is described by Equation 4.

$$s_1 = s_0 e^{-b_1 D} \quad \text{[Equation 4]}$$

In Equation 4,  $S_1$  represents the acquired MR signal, and  $S_0$  is the MR signal with  $b = 0$ . The diffusion coefficient D mainly depends on the b-value. The b-value depends on the strength and time duration of the gradient pulse applied [71].

Water diffusion is measured in the direction of the diffusion gradient. By applying gradients in the X, Y and Z direction, it is possible to measure water movement in any direction [71]. Apparent diffusion coefficient (ADC) maps are typically generated by deriving the diffusion coefficient with more than one b-value in every pixel as described in Equation 5.

$$D = -\ln\left(\frac{s_2}{s_1}\right)/(b_2 - b_1) \quad \text{[Equation 5]}$$

In Equation 5, D represents the diffusion coefficient, b represents the b-value, and S is the MR signal acquired at a given b-value. Water molecules predominantly diffuse along neuronal fibers

as diffusion across fibers is restricted by axonal membrane and, in the case of myelinated axons, myelin sheath [71]. By observing the water's diffusion direction, it is possible to map underlying tissue macrostructures that affect water diffusion [71]. If water moved freely in all directions it would be detected as an isotropic diffusion, but if water had a preferred direction of movement, anisotropy would be detected in the water diffusion [71]. To acquire water diffusion in all directions, a model developed by Basser *et al* has been used, where the measurements from all directions are fitted to a 3D ellipsoid [72]. A minimum of six directions are typically required to fit the 6 parameters of a 3D ellipsoid, i.e. the three lengths in the longest, middle and shortest axes, referred to as eigenvalues  $\lambda_1, \lambda_2, \lambda_3$  and their orientations referred to as eigenvectors  $v_1, v_2, v_3$  [71]. We can then calculate the fractional anisotropy (FA) map from the eigenvalues  $\lambda$  as described in Equation 6.

$$FA = \sqrt{\frac{1}{2} \frac{\sqrt{((\lambda_1 - \lambda_2)^2 + (\lambda_2 - \lambda_3)^2 + (\lambda_3 - \lambda_1)^2)}}{\sqrt{\lambda_1^2 + \lambda_2^2 + \lambda_3^2}}} \quad [\text{Equation 6}]$$

The resulting ADC from different directions is assigned red, green or blue color for the X, Y or Z direction, respectively, and each pixel is assigned the color in which direction it has the highest ADC value [71]. Thus, a color-coded map is calculated to display the directionality of the water diffusion [71].

DTI has mainly been used for the investigation and detection of neurological diseases and for brain white matter tracking [71]. Water diffusion in breast tumors is restricted by underlying structures such as cells and the components of the ECM [71]. In this thesis, we have applied

DTI to breast cancer xenograft models and clinical breast cancer specimens to correlate water diffusion to the corresponding Col1 fiber distribution (Chapter 5, [48]). The influence of hypoxia on water diffusion was also studied, as described in Chapter 5. In our work here, DTI was performed on an 11.7 Tesla spectrometer (Bruker Biospin, Billerica, MA, USA) with six diffusion directions ( $b \sim 1500 \text{ s/mm}^2$ ) and a 11.7 Tesla Bruker system (Bruker Corp., Billerica, MA, USA) with up to 30 diffusion direction ( $b \sim 1500 \text{ s/mm}^2$ ) for our *ex vivo* and *in vivo* DTI experiments, respectively (Chapter 5, [48]). The average diffusion-weighted (aDW) images and maps of ADC and FA were calculated using DTI Studio image processing software [73].

## **Thesis outline**

The following section features the abstracts of the four papers that comprise this thesis.

### ***Chapter 2 (Paper 1) – Hypoxic Tumor Microenvironments Reduce Collagen I Fiber Density.***

Although the mechanisms through which hypoxia influences several phenotypic characteristics such as angiogenesis, selection for resistance to apoptosis, resistance to radiation and chemotherapy, and increased invasion and metastasis are well characterized, the relationship between tumor hypoxia and components of the extracellular matrix (ECM) is relatively unexplored. The collagen I (Col1) fiber matrix of solid tumors is the major structural part of the ECM. Col1 fiber density can increase tumor initiation, progression, and metastasis, with cancer cell invasion occurring along radially aligned Col1 fibers. Here we have investigated the influence of hypoxia on Col1 fiber density in solid breast and prostate tumor models. Second harmonic generation (SHG) microscopy was used to detect differences in Col1 fiber density and

volume between hypoxic and normoxic tumor regions. Hypoxic regions were detected by fluorescence microscopy, using tumors derived from human breast and prostate cancer cell lines stably expressing enhanced green fluorescent protein (EGFP) under transcriptional control of the hypoxia response element. In-house fiber analysis software was used to quantitatively analyze Col1 fiber density and volume from the SHG microscopy images. Normoxic tumor regions exhibited a dense mesh of Col1 fibers. In contrast, fewer and structurally altered Col1 fibers were detected in hypoxic EGFP-expressing tumor regions. Microarray gene expression analyses identified increased expression of lysyl oxidase and reduced expression of some matrix metalloproteases in hypoxic compared with normoxic cancer cells. These results suggest that hypoxia mediates Col1 fiber restructuring in tumors, which may impact delivery of macromolecular agents as well as dissemination of cells.

***Chapter 3 (Paper 2) – Collagen I fiber density increases in lymph node positive breast cancers in a pilot study.*** Collagen I (Col1) fibers are a major structural component in the extracellular matrix of human breast cancers. Second harmonic generation (SHG) microscopic detection of Col1 fiber alignment was recently proposed as a novel paradigm for the prediction of human breast cancer survival. In a preliminary pilot study, we have explored the link between Col1 fiber density in primary human breast cancers and the occurrence of lymph node metastasis. Col1 fibers were detected by SHG microscopy in primary human breast cancers from patients presenting with lymph node metastasis (LN+) versus without lymph node metastasis (LN-). Col1 fiber density, which was quantified using our in-house SHG image analysis software, was significantly higher in the primary human breast cancers of LN+ versus LN- patients. Breast cancers from LN+ patients had a Col1 fiber volume of  $29.22 \pm 1.67\%$  and an inter-fiber distance

of  $2.25 \pm 0.17 \mu\text{m}$  versus a fiber volume of  $20.33 \pm 2.27\%$  with an inter-fiber distance of  $2.88 \pm 0.44 \mu\text{m}$  in breast cancers from LN- patients. We also demonstrated that tissue fixation and paraffin-embedding had no effect on SHG Col1 fiber detection and quantification. High Col1 fiber density in primary breast tumors is associated with breast cancer metastasis and may serve as an imaging biomarker of metastasis.

***Chapter 4 (Paper 3) – Hypoxic tumor environments exhibit disrupted collagen I fibers and low macromolecular transport.*** Hypoxic tumor microenvironments result in an aggressive phenotype and resistance to therapy that leads to tumor progression, recurrence, and metastasis. While poor vascularization and the resultant inadequate drug delivery are known to contribute to drug resistance, the effect of hypoxia on molecular transport through the interstitium and the role of the extracellular matrix (ECM) in mediating this transport are unexplored. The dense mesh of fibers present in the ECM can especially influence the movement of macromolecules. Collagen 1 (Col1) fibers form a key component of the ECM in breast cancers. Here we characterized the influence of hypoxia on macromolecular transport in tumors, and the role of Col1 fibers in mediating this transport using an MDA-MB-231 breast cancer xenograft model engineered to express red fluorescent protein under hypoxia. Magnetic resonance imaging of macromolecular transport was combined with second harmonic generation microscopy of Col1 fibers. Hypoxic tumor regions displayed significantly decreased Col1 fiber density and volume, as well as significantly lower macromolecular draining and pooling rates, than normoxic regions. Regions adjacent to severely hypoxic areas revealed higher deposition of Col1 fibers and increased macromolecular transport. These data suggest that Col1 fibers may facilitate macromolecular transport in tumors and their reduction in hypoxic regions may reduce this transport. Decreased

macromolecular transport in hypoxic regions may also contribute to poor drug delivery and tumor recurrence in hypoxic regions. High Col1 fiber density observed around hypoxic regions may facilitate the escape of aggressive cancer cells from hypoxic regions.

**Chapter 5 (Paper 4) – Manuscript (DTI-SHG)** Collagen 1 (Col1) fibers play an important role in macromolecular transport and cancer cell dissemination. Our goal in this study was to understand the influence of Col1 fibers on water diffusion, and to examine the potential of using noninvasive diffusion tensor imaging (DTI) to detect Col1 fibers in breast lesions. We have previously observed in genetically engineered human MDA-MB-231 breast cancer xenograft tumors that fluoresce under hypoxia, relatively low amounts of collagen 1 fibers in fluorescent hypoxic regions. The same tumor model was used to further investigate the relationship between Col1 fibers, water diffusion and anisotropy, and hypoxia. We observed for the first time that water diffusion and anisotropy followed Col1 fiber distribution in human breast cancer specimens. In regions with low Col1 fiber content, apparent diffusion coefficient (ADC) and fractional anisotropy (FA) values decreased significantly as compared to regions containing dense Col1 fibers (p-value < 0.05). In the breast cancer xenograft model, we observed that hypoxic regions with significantly lower Col1 fiber volume had significantly lower ADC and FA values as compared to normoxic tumor regions with higher Col1 fiber volume. Lastly, we performed *in vivo* DTI measurements to confirm that DTI patterns in tumors observed *in vivo* spatially co-localized with DTI patterns observed *ex vivo* in the same tumors. These studies have identified the potential use of noninvasive DTI as a biomarker to detect Col1 fiber density and further confirm the importance of Col1 fibers in molecular transport through the ECM.



## References

1. Meijer, G.A. (2000). GLOBOCAN 1: Cancer incidence and mortality worldwide. *Journal of Clinical Pathology*. 53(2): 164-164.
2. Keshtgar, M.R.S. and P.J. Ell (1999). Sentinel lymph node detection and imaging. *European Journal of Nuclear Medicine*. 26(1): 57-67.
3. Institute, N.C. *Stages of Breast Cancer*. 2013; Available from: <http://www.cancer.gov/cancertopics/pdq/treatment/breast/Patient/page2#Keypoint11>.
4. Rastelli, F. and S. Crispino (2008). Factors predictive of response to hormone therapy in breast cancer. *Tumori*. 94(3): 370-83.
5. Ross, J.S., E.A. Slodkowska, W.F. Symmans, L. Pusztai, P.M. Ravdin, and G.N. Hortobagyi (2009). The HER-2 receptor and breast cancer: ten years of targeted anti-HER-2 therapy and personalized medicine. *Oncologist*. 14(4): 320-68.
6. Engebraaten, O., H.K. Moen Vollan, and A.L. Borresen-Dale (2013). Triple-Negative Breast Cancer and the Need for New Therapeutic Targets. *Am J Pathol*.
7. Goel, S., D.G. Duda, L. Xu, L.L. Munn, Y. Boucher, D. Fukumura, and R.K. Jain (2011). Normalization of the Vasculature for Treatment of Cancer and Other Diseases. *Physiological Reviews*. 91(3): 1071-1121.
8. Jain, R.K. (2003). Molecular regulation of vessel maturation. *Nature Medicine*. 9(6): 685-693.
9. Warburg, O. (1956). On respiratory impairment in cancer cells. *Science*. 124(3215): 269-70.

10. DeBerardinis, R.J., A. Mancuso, E. Daikhin, I. Nissim, M. Yudkoff, S. Wehrli, and C.B. Thompson (2007). Beyond aerobic glycolysis: transformed cells can engage in glutamine metabolism that exceeds the requirement for protein and nucleotide synthesis. *Proc Natl Acad Sci U S A*. 104(49): 19345-50.
11. Glunde, K., Z.M. Bhujwala, and S.M. Ronen (2011). Choline metabolism in malignant transformation. *Nature Reviews Cancer*. 11(12): 835-848.
12. Borgan, E., B. Sitter, O.C. Lingjaerde, H. Johnsen, S. Lundgren, T.F. Bathen, T. Sorlie, A.L. Borresen-Dale, and I.S. Gribbestad (2010). Merging transcriptomics and metabolomics - advances in breast cancer profiling. *Bmc Cancer*. 10.
13. Thomlinson, R.H. and L.H. Gray (1955). The histological structure of some human lung cancers and the possible implications for radiotherapy. *Br J Cancer*. 9(4): 539-49.
14. Semenza, G.L. (2010). Defining the role of hypoxia-inducible factor 1 in cancer biology and therapeutics. *Oncogene*. 29(5): 625-34.
15. Ljungkvist, A.S.E., J. Bussink, J.H.A.M. Kaanders, P.F.J.W. Rijken, A.C. Begg, J.A. Raleigh, and A.J. van der Kogel (2005). Hypoxic cell turnover in different solid tumor lines. *International Journal of Radiation Oncology Biology Physics*. 62(4): 1157-1168.
16. Dewhirst, M.W., H. Kimura, S.W.E. Rehmus, R.D. Braun, D. Papahadjopoulos, K. Hong, and T.W. Secomb (1996). Microvascular studies on the origins of perfusion-limited hypoxia. *British Journal of Cancer*. 74: S247-S251.
17. Bussink, J., J.H. Kaanders, P.F. Rijken, J.A. Raleigh, and A.J. Van der Kogel (2000). Changes in blood perfusion and hypoxia after irradiation of a human squamous cell carcinoma xenograft tumor line. *Radiat Res*. 153(4): 398-404.

18. Milas, L., N.R. Hunter, K.A. Mason, C.G. Milross, Y. Saito, and L.J. Peters (1995). Role of reoxygenation in induction of enhancement of tumor radioresponse by paclitaxel. *Cancer Research*. 55(16): 3564-8.
19. Huang, L.E., J. Gu, M. Schau, and H.F. Bunn (1998). Regulation of hypoxia-inducible factor 1 alpha is mediated by an O-2-dependent degradation domain via the ubiquitin-proteasome pathway. *Proc Natl Acad Sci U S A*. 95(14): 7987-7992.
20. Jiang, B.H., E. Rue, G.L. Wang, R. Roe, and G.L. Semenza (1996). Dimerization, DNA binding, and transactivation properties of hypoxia-inducible factor 1. *Journal of Biological Chemistry*. 271(30): 17771-17778.
21. Michieli, P. (2009). Hypoxia, angiogenesis and cancer therapy: to breathe or not to breathe? *Cell Cycle*. 8(20): 3291-6.
22. Lorusso, G. and C. Rugg (2008). The tumor microenvironment and its contribution to tumor evolution toward metastasis. *Histochemistry and Cell Biology*. 130(6): 1091-1103.
23. Hanahan, D. and R.A. Weinberg (2000). The hallmarks of cancer. *Cell*. 100(1): 57-70.
24. Stasinopoulos, I., M.F. Penet, Z.H. Chen, S. Kakkad, K. Glunde, and Z.M. Bhujwala (2011). Exploiting the tumor microenvironment for theranostic imaging. *Nmr in Biomedicine*. 24(6): 636-647.
25. Egeblad, M., E.S. Nakasone, and Z. Werb (2010). Tumors as Organs: Complex Tissues that Interface with the Entire Organism. *Developmental Cell*. 18(6): 884-901.
26. De Wever, O., P. Demetter, M. Mareel, and M. Bracke (2008). Stromal myofibroblasts are drivers of invasive cancer growth. *International Journal of Cancer*. 123(10): 2229-2238.

27. Weber, C.E. and P.C. Kuo (2012). The tumor microenvironment. *Surgical Oncology-Oxford*. 21(3): 172-177.
28. Tan, J.X., E. Buache, M.P. Chenard, N. Dali-Youcef, and M.C. Rio (2011). Adipocyte is a non-trivial, dynamic partner of breast cancer cells. *International Journal of Developmental Biology*. 55(7-9): 851-859.
29. Friedl, P., Y. Hegerfeldt, and M. Tusch (2004). Collective cell migration in morphogenesis and cancer. *International Journal of Developmental Biology*. 48(5-6): 441-449.
30. Lochter, A. and M.J. Bissell (1995). Involvement of extracellular matrix constituents in breast cancer. *Semin Cancer Biol*. 6(3): 165-73.
31. Skrzydlewska, E., M. Sulkowska, M. Koda, and S. Sulkowski (2005). Proteolytic-antiproteolytic balance and its regulation in carcinogenesis. *World J Gastroenterol*. 11(9): 1251-66.
32. Song, F., K. Wisithphrom, J. Zhou, and L.J. Windsor (2006). Matrix metalloproteinase dependent and independent collagen degradation. *Front Biosci*. 11: 3100-20.
33. Zheng, W.Q., L.M. Looi, and P.L. Cheah (2002). Correlation between laminin and cathepsin D expressions in breast carcinoma. *Tumori*. 88(4): 296-9.
34. Guinec, N., V. Dalet-Fumeron, and M. Pagano (1993). "In vitro" study of basement membrane degradation by the cysteine proteinases, cathepsins B, B-like and L. Digestion of collagen IV, laminin, fibronectin, and release of gelatinase activities from basement membrane fibronectin. *Biol Chem Hoppe Seyler*. 374(12): 1135-46.
35. Parks, W.C. and R. Mecham, *Extracellular Matrix Degradation*. William C. Parks, Robert P. Mecham ed. Extracellular Matrix Degradation. Vol. Chapter 2. 2011. 23-51.

36. Brown, E., T. McKee, E. diTomaso, A. Pluen, B. Seed, Y. Boucher, and R.K. Jain (2003). Dynamic imaging of collagen and its modulation in tumors in vivo using second-harmonic generation. *Nat Med.* 9(6): 796-800.
37. McKee, T.D., P. Grandi, W. Mok, G. Alexandrakis, N. Insin, J.P. Zimmer, M.G. Bawendi, Y. Boucher, X.O. Breakefield, and R.K. Jain (2006). Degradation of fibrillar collagen in a human melanoma xenograft improves the efficacy of an oncolytic herpes simplex virus vector. *Cancer Research.* 66(5): 2509-13.
38. Myllyharju, J. and K.I. Kivirikko (2001). Collagens and collagen-related diseases. *Annals of Medicine.* 33(1): 7-21.
39. Bruce Alberts, D.B., Julian Lewis, Martin Raff, Keith Roberts, James D. Watson, *Molecular Biology of the Cell . 3rd edition.* 3 ed1994: Garland Science.
40. Shoulders, M.D. and R.T. Raines (2009). Collagen structure and stability. *Annu Rev Biochem.* 78: 929-58.
41. Provenzano, P.P., D.R. Inman, K.W. Eliceiri, J.G. Knittel, L. Yan, C.T. Rueden, J.G. White, and P.J. Keely (2008). Collagen density promotes mammary tumor initiation and progression. *BMC Med.* 6.
42. Maemura, M., S.K. Akiyama, V.L. Woods, and R.B. Dickson (1995). Expression and Ligand-Binding of Alpha-2-Beta-1 Integrin on Breast-Carcinoma Cells. *Clinical & Experimental Metastasis.* 13(4): 223-235.
43. Raman, V., D. Artemov, A.P. Pathak, P.T. Winnard, Jr., S. McNutt, A. Yudina, A. Bogdanov, Jr., and Z.M. Bhujwala (2006). Characterizing vascular parameters in hypoxic regions: a combined magnetic resonance and optical imaging study of a human prostate cancer model. *Cancer Research.* 66(20): 9929-36.

44. Kakkad, S., M. Solaiyappan, B. O'Rourke, I. Stasinopoulos, E. Ackerstaff, V. Raman, Z. Bhujwalla, and K. Glunde (2010). Hypoxic tumor microenvironments reduce collagen I fiber density. *Neoplasia*. 12(8): 608-17.
45. Pathak, A.P., D. Artemov, B.D. Ward, D.G. Jackson, M. Neeman, and Z.M. Bhujwalla (2005). Characterizing extravascular fluid transport of macromolecules in the tumor interstitium by magnetic resonance imaging. *Cancer Research*. 65(4): 1425-32.
46. Pathak, A.P., D. Artemov, M. Neeman, and Z.M. Bhujwalla (2006). Lymph node metastasis in breast cancer xenografts is associated with increased regions of extravascular drain, lymphatic vessel area, and invasive phenotype. *Cancer Research*. 66(10): 5151-8.
47. Kakkad, S.M., M.-F. Penet, A. Akhbardeh, A.P. Pathak, M. Solaiyappan, V. Raman, D. Leibfritz, K. Glunde, and Z.M. Bhujwalla (2013). Hypoxic tumor environments exhibit disrupted collagen I fibers and low macromolecular transport. *PLoS One*. 12;8(12).
48. Kakkad, S.M., J. Zhang, A. Akhbardeh, D. Jacob, M. Solaiyappan, M. Jacobs, V. Raman, D. Leibfritz, K. Glunde, and Z.M. Bhujwalla (Manuscript in preparation). Collagen fibers influence water diffusion and anisotropy. *Journal of the National Cancer Institute*.
49. Zipfel, W.R., R.M. Williams, and W.W. Webb (2003). Nonlinear magic: multiphoton microscopy in the biosciences. *Nat Biotechnol*. 21(11): 1369-77.
50. Mohler, W., A.C. Millard, and P.J. Campagnola (2003). Second harmonic generation imaging of endogenous structural proteins. *Methods*. 29(1): 97-109.
51. Franken, P.A., G. Weinreich, C.W. Peters, and A.E. Hill (1961). Generation of Optical Harmonics. *Physical Review Letters*. 7(4): 118-&.

52. Campagnola, P.J., M.D. Wei, A. Lewis, and L.M. Loew (1999). High-resolution nonlinear optical imaging of live cells by second harmonic generation. *Biophysical Journal*. 77(6): 3341-3349.
53. Zoumi, A., A. Yeh, and B.J. Tromberg (2002). Imaging cells and extracellular matrix in vivo by using second-harmonic generation and two-photon excited fluorescence. *Proc Natl Acad Sci U S A*. 99(17): 11014-9.
54. Deza, E.D.M.M., (2009). Encyclopedia of Distances, Springer.
55. Castellano, G., L. Bonilha, L.M. Li, and F. Cendes (2004). Texture analysis of medical images. *Clinical Radiology*. 59(12): 1061-1069.
56. Haralick, R.M., and L.G. Shapiro. , *Computer and Robot Vision*, 1992, Addison-Wesley.
57. Haralick, R.M., Shanmuga.K, and I. Dinstein (1973). Textural Features for Image Classification. *Ieee Transactions on Systems Man and Cybernetics*. Smc3(6): 610-621.
58. Bezdek, J.C., *Pattern recognition with fuzzy objective function algorithms*. Advanced applications in pattern recognition 1981, New York: Plenum Press. xv, 256 p.
59. Glunde, K., T. Shah, P.T. Winnard, V. Raman, T. Takagi, F. Vesuna, D. Artemov, and Z.M. Bhujwalla (2008). Hypoxia regulates choline kinase expression through hypoxia-inducible factor-1 $\alpha$  signaling in a human prostate cancer model. *Cancer Research*. 68(1): 172-180.
60. Krishnamachary, B., M.F. Penet, S. Nimmagadda, Y. Mironchik, V. Raman, M. Solaiyappan, G.L. Semenza, M.G. Pomper, and Z.M. Bhujwalla (2012). Hypoxia Regulates CD44 and Its Variant Isoforms through HIF-1 $\alpha$  in Triple Negative Breast Cancer. *PLoS One*. 7(8).

61. Contag, C.H., D. Jenkins, P.R. Contag, and R.S. Negrin (2000). Use of reporter genes for optical measurements of neoplastic disease in vivo. *Neoplasia*. 2(1-2): 41-52.
62. Weissleder, R. (2001). A clearer vision for in vivo imaging. *Nat Biotechnol*. 19(4): 316-7.
63. Wigal, S.B., C.M. Polzonetti, A. Stehli, and E. Gratton (2012). Phase synchronization of oxygenation waves in the frontal areas of children with attention-deficit hyperactivity disorder detected by optical diffusion spectroscopy correlates with medication. *J Biomed Opt*. 17(12).
64. Castano, A.P., T.N. Demidova, and M.R. Hamblin (2004). Mechanisms in photodynamic therapy: part one-photosensitizers, photochemistry and cellular localization. *Photodiagnosis and Photodynamic Therapy*. 1(4): 279-293.
65. Shaner, N.C., P.A. Steinbach, and R.Y. Tsien (2005). A guide to choosing fluorescent proteins. *Nature Methods*. 2(12): 905-909.
66. Kriege, M., C.T.M. Brekelmans, C. Boetes, P.E. Besnard, H.M. Zonderland, I.M. Obdeijn, R.A. Manoliu, T. Kok, H. Peterse, M.M.A. Tilanus-Linthorst, S.H. Muller, S. Meijer, J.C. Oosterwijk, L.V.A.M. Beex, R.A.E.M. Tollenaar, H.J. de Koning, E.J.T. Rutgers, J.G.M. Klijn, and M.R.I. Screeni (2004). Efficacy of MRI and mammography for breast-cancer screening in women with a familial or genetic predisposition. *New England Journal of Medicine*. 351(5): 427-437.
67. Jacobs, M.A. (2009). Multiparametric magnetic resonance imaging of breast cancer. *J Am Coll Radiol*. 6(7): 523-6.
68. Glunde, K., A.P. Pathak, and Z.M. Bhujwalla (2007). Molecular-functional imaging of cancer: to image and imagine. *Trends in Molecular Medicine*. 13(7): 287-97.



69. Collignon, A., F. Maes, D. Delaere, D. Vandermeulen, P. Suetens, and G. Marchal (1995). Automated multi-modality image registration based on information theory. *Information Processing in Medical Imaging*. 3: 263-274.
70. Dice, L.R. (1945). Measures of the Amount of Ecologic Association between Species. *Ecology*. 26(3): 297-302.
71. Mori, S. and J.Y. Zhang (2006). Principles of diffusion tensor imaging and its applications to basic neuroscience research. *Neuron*. 51(5): 527-539.
72. Basser, P.J., J. Mattiello, and D. LeBihan (1994). MR diffusion tensor spectroscopy and imaging. *Biophysical Journal*. 66(1): 259-67.
73. Jiang, H.Y., P.C.M. van Zijl, J. Kim, G.D. Pearlson, and S. Mori (2006). DtiStudio: Resource program for diffusion tensor computation and fiber bundle tracking. *Computer Methods and Programs in Biomedicine*. 81(2): 106-116.



## Chapter 2

---

### Hypoxic tumor microenvironments reduce collagen I fiber density

Published in: **Neoplasia**, 2010 Aug;12(8):608-17

Hypoxic tumor microenvironments reduce collagen I fiber density.

**Samata M. Kakkad**, Meiyappan Solaiyappan, Brian O'Rourke, Ioannis Stasinopoulos, Ellen Ackerstaff, Venu Raman, Zaver M. Bhujwala, and Kristine Glunde

**Abbreviations footnote**

Coll, Collagen 1

ECM, extracellular matrix

EGFP, enhanced green fluorescent protein

FOV, field of view

HIF, hypoxia inducible factor

HRE, hypoxia response element

K-S, Kolmogorov-Smirnov

LOX, lysyl oxidase

MMP, matrix metalloproteinase

P3H, prolyl-3-hydroxylases

P4H, prolyl-4-hydroxylases

PIN, prostatic intraepithelial neoplasia

PLOD, procollagen lysyl-hydroxylases

Pro-Coll, procollagen type I

ROI, region of interest

SCID, severe combined immunodeficient

SDS-PAGE, sodium dodecyl sulfate-polyacrylamide gel electrophoresis

SHG, second harmonic generation

TGF, transforming growth factor

uPA, urokinase plasminogen activator

uPAR, urokinase plasminogen activator receptor

## **Abstract**

Although the mechanisms through which hypoxia influences several phenotypic characteristics such as angiogenesis, selection for resistance to apoptosis, resistance to radiation and chemotherapy, and increased invasion and metastasis are well characterized, the relationship between tumor hypoxia and components of the extracellular matrix (ECM) is relatively unexplored. The collagen I (Col1) fiber matrix of solid tumors is the major structural part of the ECM. Col1 fiber density can increase tumor initiation, progression, and metastasis, with cancer cell invasion occurring along radially aligned Col1 fibers. Here we have investigated the influence of hypoxia on Col1 fiber density in solid breast and prostate tumor models. Second harmonic generation (SHG) microscopy was used to detect differences in Col1 fiber density and volume between hypoxic and normoxic tumor regions. Hypoxic regions were detected by fluorescence microscopy, using tumors derived from human breast and prostate cancer cell lines stably expressing enhanced green fluorescent protein (EGFP) under transcriptional control of the hypoxia response element. In-house fiber analysis software was used to quantitatively analyze Col1 fiber density and volume from the SHG microscopy images. Normoxic tumor regions exhibited a dense mesh of Col1 fibers. In contrast, fewer and structurally altered Col1 fibers were detected in hypoxic EGFP-expressing tumor regions. Microarray gene expression analyses identified increased expression of lysyl oxidase and reduced expression of some matrix metalloproteases in hypoxic compared with normoxic cancer cells. These results suggest that hypoxia mediates Col1 fiber restructuring in tumors, which may impact delivery of macromolecular agents as well as dissemination of cells.

## Introduction

Tumors display hypoxic environments that primarily arise from their abnormal and chaotic vasculature [1]. Hypoxia triggers multiple signaling cascades that significantly affect biologic outcomes including angiogenesis, selection for resistance to apoptosis, resistance to radiation and chemotherapy, and increased invasion and metastasis [2, 3]. The extracellular matrix (ECM) plays an important role in drug delivery as well as invasion and metastasis, but the relationship between tumor hypoxia and ECM components is relatively unexplored.

The ECM in breast and prostate tumors is composed of a complex meshwork of fibrillar collagens, glycoproteins, and proteoglycans [4, 5], which profoundly affect metastasis, as well as proliferation, angiogenesis, adhesion, migration, invasion, and drug delivery [4–9]. Collagen I (Col1) fibers are the major structural ECM component in breast [4, 10–12] and prostate tumors [8, 13, 14]. A recent study demonstrated a causal relationship between Col1 fibers and metastasis in a bitransgenic mouse model with increased stromal Col1, in which high Col1 fiber density was able to significantly increase mammary tumor initiation, progression, and lung metastasis [11]. Cancer cell invasion in this mouse model started at the tumor-stromal interface in the primary tumor along radially aligned Col1 fibers [10]. The presence of a fibrotic focus in central tumor regions of breast cancer patients has been suggested as a prognostic factor and surrogate marker for hypoxia in breast tumors [15, 16]. A recent study in a carcinogen-induced rat mammary carcinoma model indicated that, overall, more fibrotic tumors were also more hypoxic [17]. Cells of myofibroblast phenotype in the reactive stroma of Gleason 3–scored prostate cancers

exhibited an elevated Col1 synthesis, which was first observed in activated peri-acinar fibroblasts adjacent to prostatic intraepithelial neoplasia [8].

Col1 fiber biosynthesis, maturation, and deposition is a multistep process, initiated by the Col1A1 and Col1A2 genes that produce the pro- $\alpha$ 1(I) and pro- $\alpha$ 2(I) chains, respectively, of procollagen type I (pro-Col1). Intracellular prolyl-3/4-hydroxylases, lysyl hydroxylases, and protein disulfide isomerases further modify these pro- $\alpha$ 1(I) and pro- $\alpha$ 2(I) chains to form pro-Col1 triple helices [18, 19]. Fibroblasts are primarily responsible for synthesizing and secreting pro-Col1, whereas hepatic stellate cells [20], osteoblasts [21], odontoblasts [21], and hypoxic smooth muscle cells [22] also have the ability to produce pro-Col1. Extracellular procollagen N- and C-proteinases cleave the pro-Col1 propeptide ends of secreted pro-Col1, thereby initiating the self-assembly of collagen microfibrils [19]. Extracellular lysyl oxidase (LOX) covalently cross-links Col1 microfibrils with each other to form strong and stable mature Col1 fibers that surround cells within the ECM [19]. Fibrillar Col1 profoundly affects the mechanical properties of tissues, with high Col1 fiber content corresponding to more rigid and less compressible tissue properties [19]. Breast [23, 24] and prostate cancer cells [8] can stimulate Col1 synthesis in tumor-associated fibroblasts and reorganize a previously random Col1 fiber matrix [10]. In addition, Col1 fibers in breast and prostate tumors can be degraded and remodeled by matrix metalloproteinase (MMP)-1 and MMP-14 (also referred to as MT1-MMP), which are secreted by or located on the cancer cells [25]. Whereas MMP-1 and MMP-14 initiate Col1 fiber degradation in the tumor microenvironment, further breakdown is mediated by MMP-2, MMP-9, MMP-12, and MMP-13 [26, 27], as well as cathepsins and the urokinase plasminogen activator (uPA) and uPA receptor (uPAR) system [28].

In normal tissues, hypoxic environments promote the formation of collagen deposits [18, 29, 30]. The influence of hypoxia on Col1 remodeling in solid tumors *in vivo* is relatively unexplored. The purpose of our study was to determine the effect of hypoxia on Col1 fibers in solid breast and prostate tumor models.

We used second harmonic generation (SHG) microscopy to detect Col1 fibers in these tumor models. SHG microscopy detects the intrinsic signal of the noncentrosymmetric physical properties of Col1 fibers without an exogenous optical imaging agent [31, 32]. SHG microscopy has been previously used in tumor xenografts to assess ECM integrity [31]. With SHG microscopy of human specimens, Col1 fibers in breast tumors were found to be straighter and denser than the fibers in benign lesions or normal breast tissue [32]. Here, for the first time, we have applied SHG microscopy to detect differences in Col1 fibers between hypoxic and normoxic tumor regions. The studies were performed using tumors derived from human breast and prostate cancer cell lines stably expressing enhanced green fluorescent protein (EGFP) under transcriptional control of five copies of a hypoxia response element (HRE), which have already been used in several studies in our laboratory [33, 34]. To analyze Col1 fiber density and volume from the SHG microscopy images, we developed an in-house fiber analysis software. Normoxic tumor regions without fluorescence exhibited a dense mesh of Col1 fibers, whereas fewer and structurally altered Col1 fibers were detected in hypoxic EGFP-expressing tumor regions. Microarray gene expression analyses indicated increased LOX expression and reduced expression of MMPs in hypoxic cancer cells. These results suggest that tumor hypoxia can result in Col1 fiber restructuring, which may influence several ECM-related characteristics such as macromolecular transport and cancer cell dissemination.



## Materials and Methods

### *Cell Lines and Tumor Models*

The triple-negative metastatic human breast cancer cell line MDAMB-231 [35] and the androgen-independent human prostate cancer cell line PC-3 [36] were obtained from the American Type Culture Collection (ATCC, Rockville, MD). Wild-type MDA-MB-231 [37] and PC-3 [38] cells were maintained as previously described. To generate MDA-MB-231 and PC-3 cells that express EGFP under hypoxic conditions as a hypoxia-inducible factor 1 (HIF-1)–driven hypoxia sensor, MDA-MB-231 and PC-3 cells were stably transfected with a construct containing five copies of the HRE of the human VEGF-A gene ligated to the complementary DNA of EGFP, which produced MDA-MB-231–5HRE-EGFP and PC-3–5HRE-EGFP as previously described [33, 34]. EGFP expression was verified in hypoxic cell cultures by fluorescence microscopy and in corresponding protein lysates by sodium dodecyl sulfate–polyacrylamide gel electrophoresis and immunoblot analysis with anti-EGFP antibody (BD Biosciences, San Jose, CA) as previously described [33, 34]. In our previous studies, we observed detectable EGFP expression within 6 hours of exposure to less than 1% O<sub>2</sub> and robust EGFP expression by 20 hours in HREEGFP–expressing cells in culture [33]. Cells were routinely characterized for hypoxia–driven EGFP expression before inoculation in mice.

Two million MDA-MB-231–5HRE-EGFP cells were orthotopically inoculated in the mammary fat pad of anesthetized female severe combined immunodeficient mice as previously described [39] to grow solid MDA-MB-231–5HRE-EGFP xenografts. Solid PC-3–5HREEGFP

prostate tumor xenografts were obtained by inoculating  $2 \times 10^6$  PC-3-5HRE-EGFP cells in 0.1 ml of Hank's balanced salt solution (Sigma-Aldrich, St Louis, MO) subcutaneously in the right flank of male severe combined immunodeficient mice [33, 34]. Tumor xenografts reached their final experimental size within 8 weeks. In our previous studies, low oxygen tension was detected in several EGFP fluorescing regions ( $pO_2 < 0.6$  mm Hg), and higher oxygen tensions ( $5.0$  mm Hg  $< PO_2 < 40.0$  mm Hg) comparable to normal muscle tissue ( $23.0$  mm Hg  $< pO_2 < 50.0$  mm Hg) were detected in several non-fluorescing peripheral tumor regions measured with a fiber-optic oxygen probe inserted *in vivo* [33].

#### *SHG and Confocal Microscopy*

Animals were sacrificed, tumor xenografts were excised for *ex vivo* fluorescence microscopy, and three to five serial 2-mm-thick fresh tissue slices were cut using an acrylic adjustable tissue slicer (12 mm depth up to 25mmwidth; Braintree Scientific, Inc., Braintree, MA) and tissue slicer blades (Braintree Scientific, Inc.). These serial fresh xenograft tissue slices were each placed on individual microscope slides (Fisher brand catalog number 12-550-34; Fisher Scientific, Pittsburgh, PA), which were stored in a box containing ice on the bottom, in which the slides were located on a perforated plate at approximately 1 cm above the ice to ensure a tissue temperature of approximately 4°C to avoid tissue degradation. For microscopic measurements, a given slide holding a tumor slice was taken out of the icebox and placed under the microscope for the time of microscopic imaging. In between microscopic measurements, the fresh tumor slices were returned to the icebox to keep the tissue at 4°C, and they were periodically moistened with saline to avoid dehydration of the tissue. EGFP expression in these

tumor slices was detected by fluorescence microscopy using a 1× objective attached to a Nikon inverted microscope, equipped with a filter set for 450 to 490 nm excitation and 500 to 550 nm emission, and a Nikon Coolpix digital camera (Nikon Instruments, Inc., Melville, NY). These 1× images were used to coarsely locate hypoxic and normoxic tumor regions in subsequent SHG microscopic acquisitions.

For SHG microscopy, a microscope slide holding a fresh 2-mm-thick tissue slice was removed from the icebox and placed under the objective of a multiphoton system. After SHG microscopy, the slide was moistened and returned to the icebox. The SHG microscopy of tumor slices was performed on a Nikon/Bio-Rad or a Zeiss LSM 710 NLO Meta multiphoton microscopy system (Carl Zeiss Micro Imaging, Inc., Thornwood, NY). The Nikon E600FN upright research fluorescence microscope was equipped with a Bio-RadMRC-1024/2-P multiphoton attachment (Bio-Rad, Hercules, CA) and a Tsunami 3941 M1S femtosecond mode-locked Ti:Sa pulsed laser (Spectra Physics, Mountain View, CA) pumped by a 10-W Millennia X solid-state laser (Spectra Physics). Laser light of 880 nm was used as an incident light for generation of the SHG Coll1 signal and for two-photon excitation of EGFP fluorescence. The SHG signal from Coll1 fibers was detected at 410 to 470 nm, and the EGFP fluorescence was detected at 500 to 560 nm. The Zeiss 710 NLO Meta confocal microscope (Carl Zeiss Micro-Imaging, Inc.) was equipped with a 680- to 1080-nm tunable Coherent Chameleon Vision II laser (Coherent, Inc., Santa Clara, CA). For SHG Coll1 microscopy, incident laser light at 880 nm was used, and the SHG signal was detected at 410 to 470 nm. Simultaneously, EGFP was excited with the 488-nm laser line and detected at 500 to 560 nm. On both microscope systems, a 25× lens was used to acquire confocal z-stacks of approximately 100 μm thickness with a z-interval

of approximately 5  $\mu\text{m}$ . Neither the SHG nor the EGFP signal of a given field of view (FOV) on a given tumor tissue slice changed over time when imaging the same FOV multiple times within one imaging session, for example, once in the beginning and once at the end of an imaging session.

After microscopy, fresh tumor slices were frozen in Tissue Tek OCT freezing compound (Sakura Finetek USA, Inc., Torrance, CA). Frozen slices were cryo-sectioned with a microcryotome (Microm International, Walldorf, Germany) at 100  $\mu\text{m}$  thickness, fixed with 3% paraformaldehyde (Sigma-Aldrich) solution, stained for nuclei with Hoechst 33342 (Invitrogen Corp, Carlsbad, CA), and mounted with Faramount aqueous mounting medium (DakoCytomation, Carpinteria, CA). Two-photon excitation of Hoechst 33342 at 880 nm together with excitation of the SHG signal was performed on these whole-mount sections. Hoechst was detected at 450 to 500 nm, and the SHG Col1 signal was detected at 400 to 450 nm. EGFP was single-photon excited at 488 nm and detected at 500 to 560 nm.

### *Image and Statistical Analysis*

Image analysis to quantify (1) the Col1 fiber distance distribution and (2) the Col1 fiber volume was performed using in-house software. This software was written in Matlab using MATLAB 7.4.0 (The MathWorks, Natick, MA) and described in detail in the Results section. Regions of interest (ROIs) containing defined percentages of hypoxic EGFP fluorescing cells were drawn and analyzed with this software. A one-sided t test ( $\alpha = 0.05$ ) was used to detect

significant differences between hypoxic and normoxic ROIs using Microsoft Office Excel 2007 (Microsoft, Redmond, WA). P values < .05 were considered to be significant.

#### *Gene Expression Analysis with Affymetrix Microarrays of Hypoxic versus Normoxic Cells*

Wild-type MDA-MB-231 and PC-3 cells were exposed to hypoxic conditions in a commercially available culture chamber (BioSpherix Ltd, Redfield, NY) for 24 and 48 hours. This humidified culture chamber was maintained at 37°C and equilibrated with a mixture of 0.3% to 0.7% O<sub>2</sub> and 5% CO<sub>2</sub> for the required time intervals, using controlled N<sub>2</sub> and CO<sub>2</sub> gas infusions (BioSpherix). Controls were placed in a standard cell culture incubator at 37°C in a humidified atmosphere containing 21% O<sub>2</sub> and 5% CO<sub>2</sub>. Total cellular RNA was isolated from approximately 10<sup>7</sup> cells, using the RNeasy Mini Kit (Qiagen, Inc., Valencia, CA) and QIAshredder homogenizer spin columns (Qiagen) as previously described [37]. The microarray hybridization was performed at the Johns Hopkins Medical Institution's Microarray Core Facility using the Human Genome U133 Plus 2.0 GeneChip array (Affymetrix, Inc, Santa Clara, CA) and the Affymetrix GeneChip platform, Agilent GeneArray Scanner, and Micro Array Suite 5.0 software by Affymetrix as previously described [37]. To estimate the gene expression signals, data analysis was conducted on the chips' cell intensity file probe signal values at the Affymetrix probe pair (perfect match probe and mismatch probe) level, using statistical techniques and the robust multiarray analysis package as previously described [37, 40, 41]. The posterior probabilities of the differential expression of genes were estimated for hypoxic versus normoxic MDAMB-231 cells and hypoxic versus normoxic PC-3 cells. The criterion of the

posterior probability  $> 0.5$ , which means the posterior probability is larger than by chance, was used to produce the differentially expressed gene lists. All computations were performed under the R environment as previously described [37].

## **Results**

To achieve quantitative analysis of Col1 fibers from SHG images, we developed in-house image analysis software. A major challenge in the quantitative analysis of Col1 fiber distribution and volume occurs because of the complex intersecting patterns of the fibers in three spatial dimensions, which is apparent in the raw data set of z-sections in Figure 1. We therefore developed a practical and intuitive approach to characterize these distribution patterns by analyzing the interstices in the fibrillar mesh outlined in Figure 2.

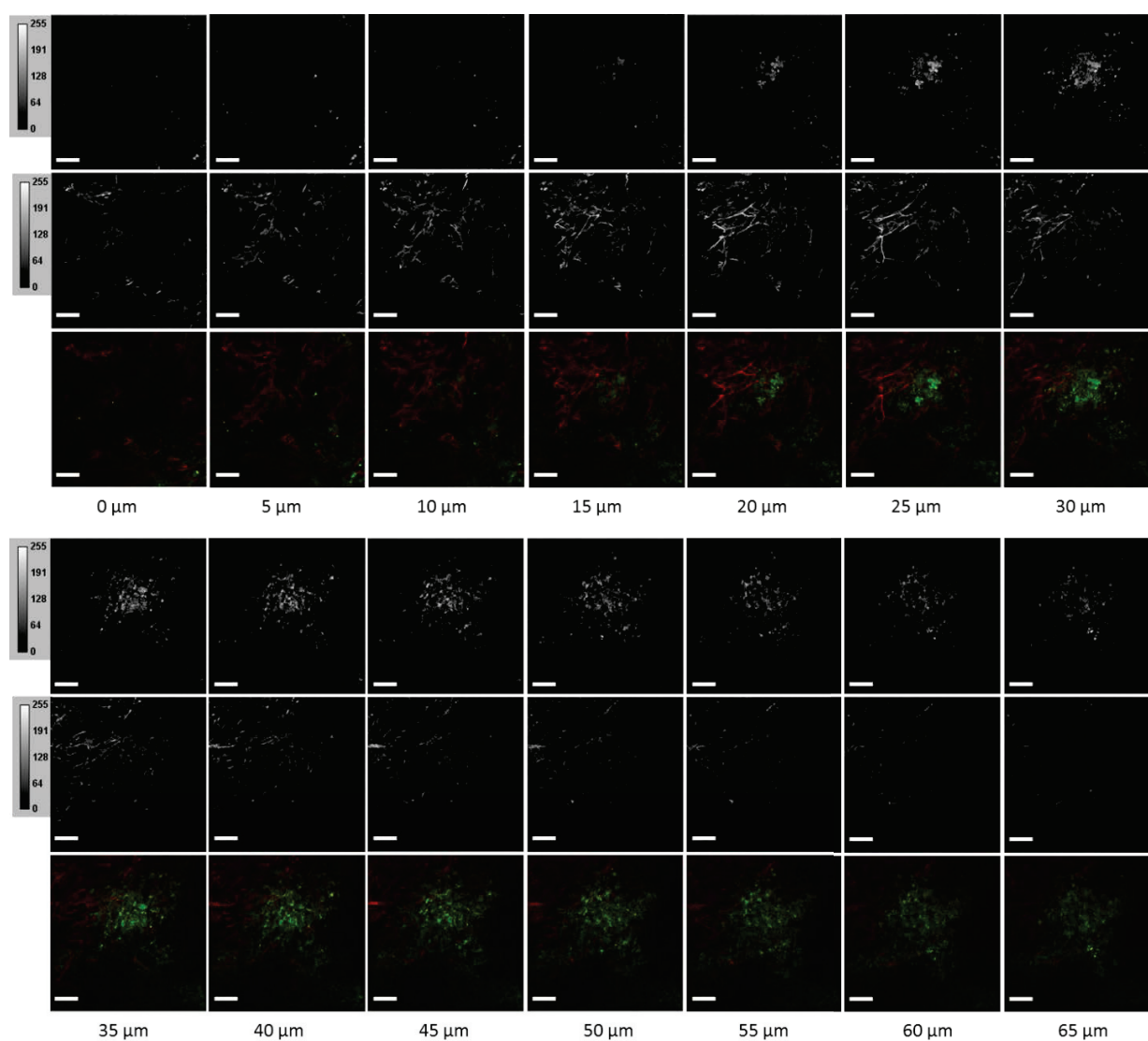


**Figure 1:** Complete representative raw data set showing the z-series of EGFP images (top panel) and SHG images (middle panel) in gray scale, as well as the merged images displaying the EGFP channel in green and the SHG channel in red. Scale bars, 100  $\mu\text{m}$ .

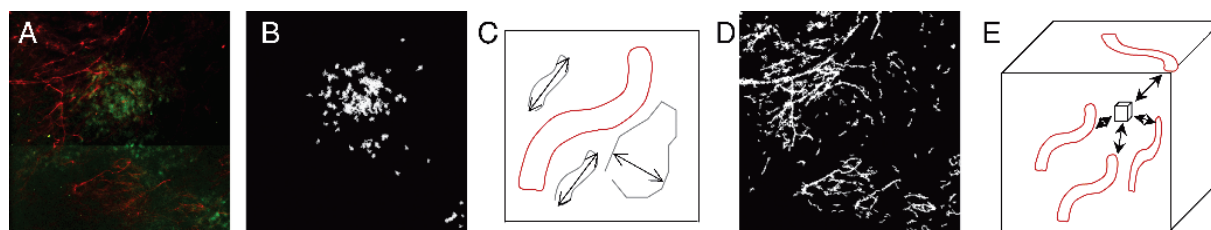


**Figure 2:** Quantification of fiber distance distribution with in-house software: (A) representative raw image data shown as z-projection of the Col1 fibers (red) in a hypoxic (green) region; (B) representative example of software detection of hypoxic cells (green in raw image (A)) independent of fluorescence intensity and threshold of raw images; preprocessing using the filter (C) to identify fiber-like objects (red) among various non-fiber-like objects in the image to produce (D) the corresponding Col1 fiber image; (E) computing the distances three-dimensionally to the surrounding fibers from each voxel to determine the nearest distance to a fiber. The fiber volume is computed as an additional parameter.

The analytical approach presented in Figure 2 was applied to quantify the Col1 fiber distances and volumes from tumor xenograft models. Figure 2A shows the representative raw image displayed as a z-projection of the three-dimensional data set, which was generated from the z-sections in Figure 1. Figure 2B shows that the software was able to detect hypoxic cells independent of variability in the dynamic range of the green fluorescence signal in the images. The hypoxic ROIs in our analysis were defined as containing more than 80% green fluorescing hypoxic cells; normoxic regions contained less than 1% of green fluorescing hypoxic cells in the ROI. Images were preprocessed to exclude noise and non fibrillar shapes as shown in Figure 2C. Figure 2D shows that the software detected Col1 fiber structures from the raw image. A three-dimensional volume of the Col1 fiber mesh within a given ROI was selected, and Euclidean distances from each empty voxel to the nearest Col1 fiber voxel were computed to quantify the fiber distances within the mesh (Figure 2E). This provided a cumulative histogram of the distance distribution as a measure of porosity of the mesh as shown in the subsequent figures. In addition, a second parameter, the Col1 fiber volume, was quantified using our in-house three-dimensional image quantification software. Figure 3 shows the performance of this software on



an artificial training data set. We manually generated a sparser fiber image A as shown in Figure 3A, which was modified in Figure 3B with a few additional lines representing fibers to give image B. Our software was able to correctly detect a shift toward a denser fiber distribution (Figure 3C) and an increased fiber volume (Figure 3D) for image B compared with image A. Compared with analysis methods based on Fourier analysis [32], our method derived parameters that are visually evident in the images. Because of its robustness, the method requires minimal preprocessing steps that can be adopted to varying image quality.

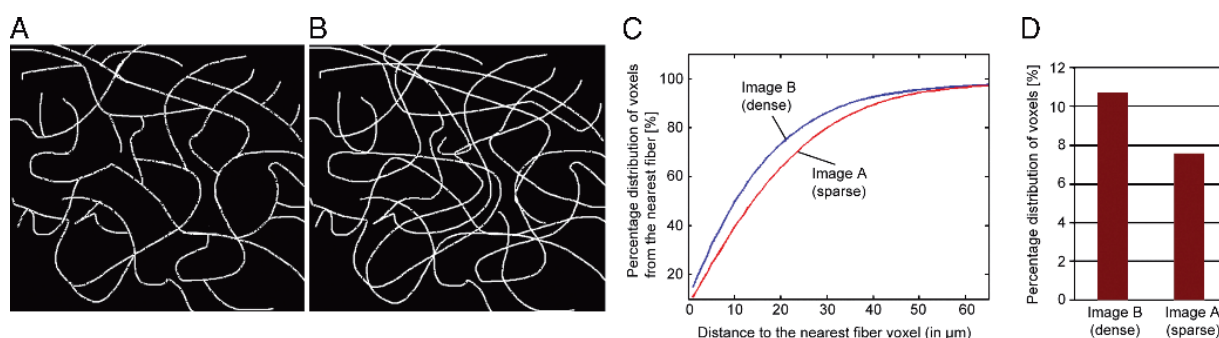


**Figure 3:** Performance of our software on a training data set of two artificial manually drawn fiber images of (A) sparser fibers and (B) denser fibers, in which just a few more lines representing fibers were added to image A. The software correctly detected (C) the shift toward a denser fiber distribution as well as (D) the increase in fiber volume in image B compared with that in image A.

A representative example from an MDA-MB-231 breast tumor is shown in Figure 4 and that from a PC-3 prostate tumor is shown in Figure 5. Low-power microscopic images covering 2-mm-thick tumor slices from representative MDA-MB-231-5HRE-EGFP (Figure 4A) and PC-3-5HRE-EGFP (Figure 5A) tumors demonstrated that the hypoxic green fluorescing regions were heterogeneously distributed throughout the tumors.

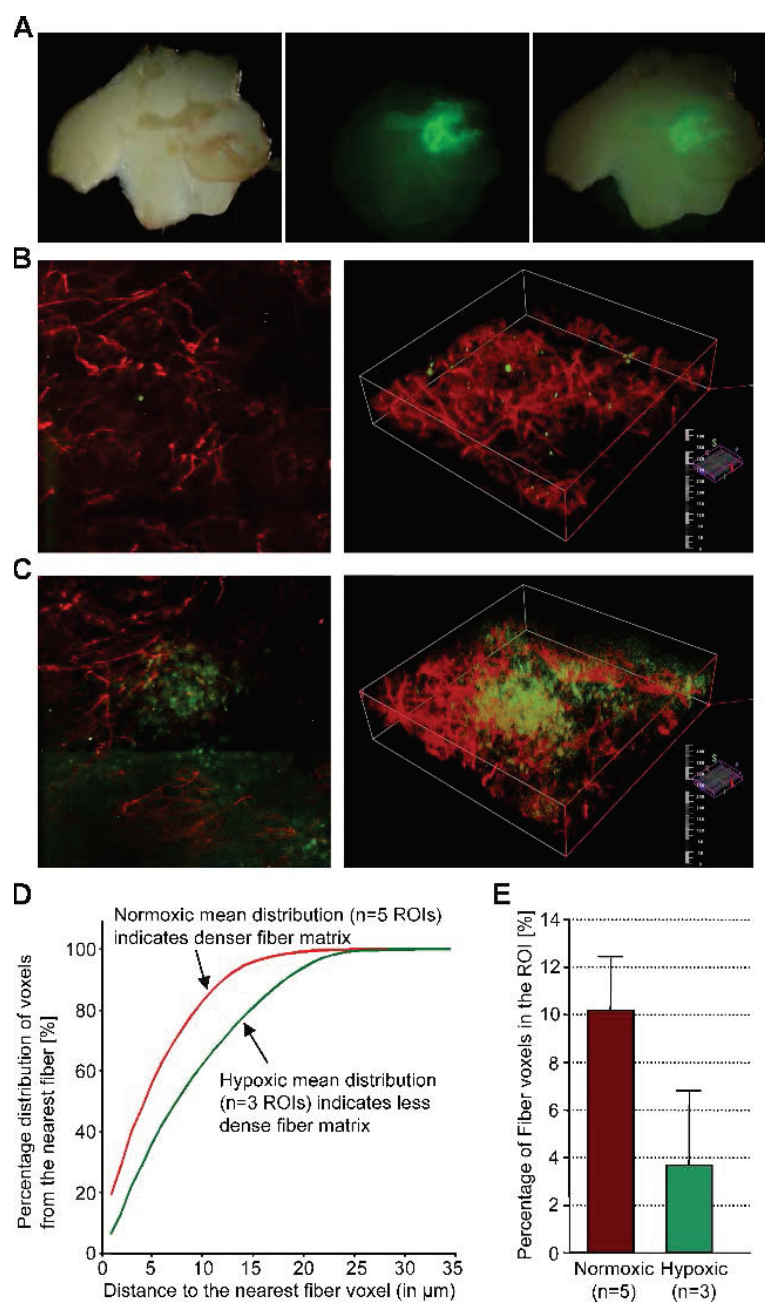


**Figure 4:** Hypoxic regions are heterogeneously distributed throughout MDA-MB-231 tumors as evident in a representative set of (A) bright-field, green fluorescence, and overlay microscopic images (left to right) of a fresh 2-mm-thick section from a solid MDA-MB-231-5HRE-EGFP breast tumor. Representative SHG Col1 fiber (red) and hypoxia (green) images are from (B) a normoxic and (C) a hypoxic FOV, displayed as z-projection (left) and as three-dimensionally reconstructed image (right). We computed (D) the mean distance distribution to the nearest fiber voxel as a measure of fiber density and (E) the percentage of fiber voxels within the ROI (mean $\pm$ SD). Data are from three tumors. Hypoxic regions had more than 80%, and normoxic regions had less than 1% of hypoxic EGFP-expressing cells in the ROI. Hypoxic tumor regions contained less dense and fewer Col1 fibers than normoxic regions in MDA-MB-231 breast tumor xenografts stably expressing HRE-EGFP.

Hypoxic regions of MDA-MB-231 breast as well as PC-3 prostate tumor xenografts displayed significantly sparser, more porous Col1 fibers than normoxic regions as evident from representative microscopic images of normoxic (Figures 4B and 5B) and hypoxic regions (Figures 4C and 5C). Figures 4, B and C, and 5, B and C, show z-projections of the z-stack on the left and the corresponding three-dimensional display of the image on the right. The median hypoxic Col1 inter fiber distances were significantly ( $P = 0.050$  for MDA-MB-231,  $n = 3-5$ ;  $P = 0.002$  for PC-3,  $n = 9$ ) higher compared with the median normoxic Col1 inter fiber distances for both breast (Figure 4D,  $n = 3-5$  ROIs) and prostate tumor xenografts (Figure 5D,  $n = 9$  ROIs). Cumulative histograms of the Col1 fiber distance distributions of breast (Figure 4D) and prostate (Figure 5D) tumor xenografts demonstrated that the mean Col1 fiber distance distribution shifted toward longer inter fiber distances in hypoxic compared with normoxic regions. This increased Col1 fiber distance in hypoxic tumor areas implied a more porous distribution of Col1 fibers in hypoxic versus normoxic tumor regions. The Col1 fiber volume was significantly lower (breast tumor model:  $P = 0.0428$ ,  $n = 3-5$  ROIs in Figure 4E; prostate tumor model:  $P = 0.0004$ ,  $n = 9$  ROIs in Figure 5E) in hypoxic than in normoxic regions in both tumor models, consistent with the fewer, more porous distribution of Col1 fibers in hypoxic tumor regions. Using Hoechst 33342 staining and fluorescence microscopic detection of cell nuclei, we confirmed that an equal number of cells and comparable cell density were present in hypoxic and normoxic regions of MDA-MB-231 and PC-3 tumor xenografts, as shown in representative images from MDA-MB-231 tumors in Figure 6.

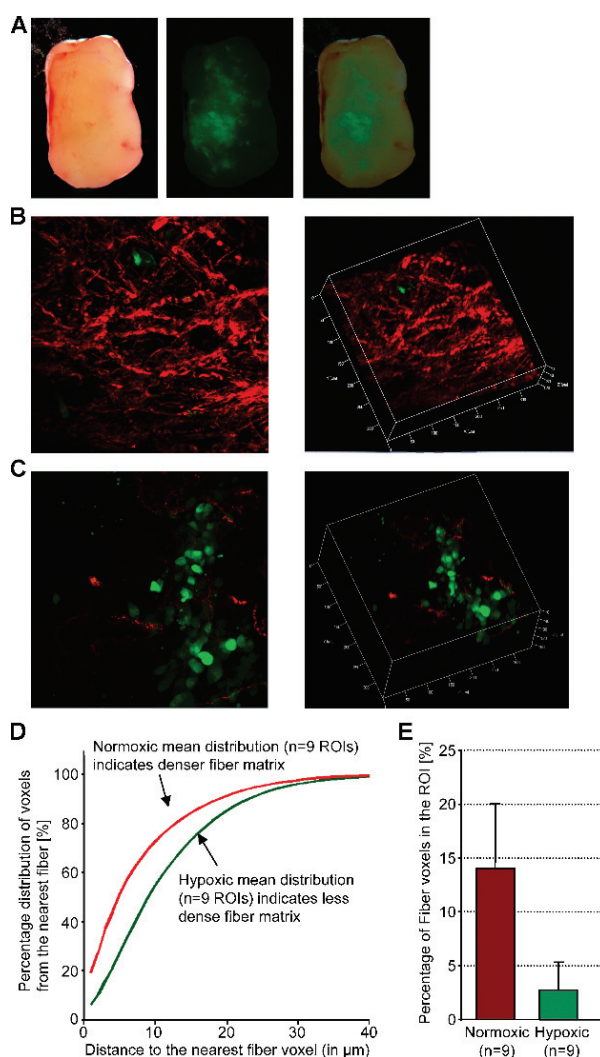


**Figure 5:** Consistent with Figure 2, hypoxic regions are heterogeneously distributed throughout solid PC-3 tumors as evident in a representative set of (A) bright-field, green fluorescence, and overlay microscopic images (left to right) of a fresh 2-mm-thick section from a solid PC-3-5HRE-EGFP prostate tumor. Representative SHG Col1 fiber (red) and hypoxia (green) images are from (B) a normoxic and (C) a hypoxic FOV, displayed as z-projection (left) and as three-dimensionally reconstructed image (right). We computed (D) the mean distance distribution to the nearest fiber voxel as a measure of fiber density and (E) the percentage of fiber voxels within the ROI (mean  $\pm$  SD). Data are from three tumors. Hypoxic regions had more than 80%, and normoxic regions had less than 1% of hypoxic EGFP-expressing cells in the ROI. Hypoxic tumor regions contained less dense and fewer Col1 fibers than normoxic regions in PC-3 prostate tumor xenografts stably expressing HRE-EGFP.

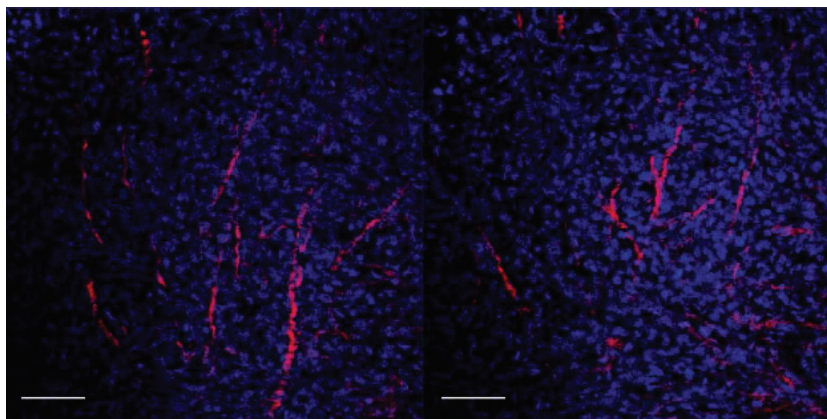


**Figure 6:** Representative z-sections of Hoechst 33342-stained whole-mount sections demonstrate that cells are evenly distributed throughout the tumors, independent of local fiber density. Col1 fibers are displayed in red, and nuclei are displayed in blue. Scale bars, 100  $\mu\text{m}$ .

We investigated differences in gene expression of factors secreted by hypoxic versus normoxic cancer cells that can influence Col1 synthesis, cross-linking, and degradation. A comparison of gene expression analyzed using Affymetrix Human Genome U133 Plus 2.0 GeneChip arrays of hypoxic versus normoxic cells for MDA-MB-231 breast cancer cells is shown in Table 1 and that for PC-3 prostate cancer cells is shown in Table 2. Both cancer cell types showed increased expression of LOX under hypoxic conditions in cell culture. In addition, some MMPs were under expressed under hypoxic conditions, such as MMP-3 in MDA-MB-231 breast cancer cells and MMP-1 and MMP-16 in prostate cancer cells. The uPAR was overexpressed in hypoxic PC-3 cells compared with normoxic controls. Other than the reported genes, no differences were detected in any other MMPs, cathepsins, tissue inhibitors of metalloproteases, or genes involved in Col1 synthesis and degradation. Additional studies are currently underway to elucidate the molecular differences leading to the changes on Col1 fiber patterns in hypoxic compared with normoxic tumor regions.

**Table 1:** Genes of secreted factors that are involved in Col1 synthesis and breakdown and contained on the affymetrix human genome U133 Plus 2.0 Array, which are differentially expressed in hypoxic versus normoxic human MDA-MB-231 breast cancer cells.

Gene Group	Gene Title	Gene Symbol	Representative Public ID	Fold Change	Probability
Col1 synthesis/crosslinking	Lysyl oxidase	LOX	NM_002317	5.2446	0.9435
Matrix metallo-proteases	matrix metalloproteinase 3 (stromelysin 1, progelatinase)	MMP3	NM_002422	-3.9105	0.7526

**Table 2:** Genes of secreted factors that are involved in Col1 synthesis and breakdown and contained on the affymetrix human genome U133 Plus 2.0 Array, which are differentially expressed in hypoxic versus normoxic human PC-3 prostate cancer cells.

Gene Group	Gene Title	Gene Symbol	Representative Public ID	Fold Change	Probability
Col1 synthesis/crosslinking	Lysyl oxidase	LOX	NM_002317	3.2023	1.000
Matrix metallo-proteases	matrix metalloproteinase 1 (interstitial collagenase)	MMP1	NM_002421	-1.9742	0.9966
	matrix metalloproteinase 16 (membrane-inserted)	MMP16	U79292	-2.1110	0.9995
uPA System Proteases	plasminogen activator, urokinase receptor	PLAUR	U08839	2.1025	0.9974

## Discussion

Since the discovery of HIF-1 and HREs as transcriptional controls in multiple genes [42], it has become evident that tumor hypoxia is associated with a more aggressive cancer phenotype [43]. In this study, we demonstrated for the first time that hypoxic regions in solid tumors contain significantly fewer and less dense Col1 fibers. We also developed a practical, intuitive,

and robust image analysis approach to quantitatively characterize differences in Col1 fiber matrices and provide parameters that are visually evident, such as the Col1 fiber distance distribution and the Col1 fiber volume. Col1 fibers are the major structural ECM component in breast [4, 10–12] and prostate tumors [8, 13, 14], and high Col1 fiber density and elevated Col1 synthesis have been associated with mammary tumor initiation, progression, and metastasis [10, 11] and prostate carcinogenesis [8]. Our data show that hypoxia significantly reduced the Col1 fiber matrix density in invasive, metastatic solid breast and prostate tumor models, whereas normoxic tumor regions contained a dense meshwork of Col1 fibers. Patient and animal model data associating increased fibrosis with elevated hypoxia do not contradict our current study because these studies did not compare hypoxic and normoxic regions within a given tumor but rather evaluated overall tumor hypoxia within a given tumor, based on staining Figure 5. Consistent with Figure 2, hypoxic regions are heterogeneously distributed throughout solid PC-3 tumors as evident in a representative set of (A) bright-field, green fluorescence, and overlay microscopic images (left to right) of a fresh 2-mm-thick section from a solid PC- hypoxia markers, with respect to overall fibrosis staining in the same tumor [15–17]. Taken together, these findings indicate that although a dense Col1 matrix may be required for tumor initiation, its presence may not be necessary at later stages of tumor growth when hypoxia occurs. Our data suggest that once solid tumors are large enough for hypoxia to occur because of insufficient and chaotic vascularization, these hypoxic regions can acquire a loose and porous Col1 fiber matrix. Our previous validation of HRE-controlled expression of EGFP in cells in culture as well as in hypoxic tumor regions *in vivo* suggests that EGFP expression detected hypoxia of 1% or less that had existed for at least 6 hours and was within an oxygen tension of  $pO_2$  less than 0.6 mmHg [33]. Changes in the Col1 fiber matrix were therefore characterized in these chronically hypoxic

regions. Future studies of the effects of acute hypoxia, reoxygenation, and transient hypoxia on the Col1 fiber matrix as well as the causative changes in gene expression will provide further insight into the regulation of Col1 fibers in tumors.

Col1 fiber degradation through proteolytic enzymes and reduced Col1 fiber synthesis are possible explanations for the less dense Col1 fiber matrix in hypoxic tumor regions. In terms of degradative processes, hypoxic conditions can increase the expression and activity of MMP-1 [44–46] and MMP-14 [47, 48], especially in cancer cells. However, our microarray-based gene expression analysis in cell cultures revealed a reduction in MMP-3 or MMP-1 and MMP-16 expression on exposure to hypoxia in MDA-MB-231 breast or PC-3 prostate cancer cells, respectively. These cancer cell lines may behave differently under cell culture conditions compared with the *in vivo* situation in solid tumors. Further studies are necessary to compare the expression and activity levels of MMPs from cells within the tumor microenvironment, such as stromal fibroblasts, endothelial cells, and macrophages, among others. Other degradative pathways, such as the uPA-initiated cascade, may be involved in degrading Col1 fibers in hypoxic tumor regions. In this cascade, secreted uPA binds to cellular uPARs to catalyze the conversion of plasminogen to plasmin, which is a broad-spectrum enzyme that results in immediate ECM degradation or activation of multiple MMPs [28]. Hypoxic PC-3 cells in tissue culture showed higher uPA activity levels than oxygenated PC-3 cells [38]. Exposure of MDA-MB-231 cells to hypoxia was shown to increase uPAR expression along with increasing the invasiveness of these cells [49, 50], which would support the possibility of uPAR-mediated Col1 degradation in hypoxic tumor regions.



In terms of Col1 synthesis, hypoxia has been found to stimulate Col1 fiber synthesis and cross-linking as outlined here. Hypoxia has been observed to activate the Col1A1 promoter through transforming growth factor  $\beta$  that is activated by HIF-1 [21, 22] or by posttranscriptional processes [30]. Hypoxia was also shown to stimulate the expression of a cluster of hydroxylases required in the posttranslational processing of Col1 fibers [18]. Expression of these hydroxylases, such as prolyl-4-hydroxylases and procollagen lysyl-hydroxylase, may be coordinated by HIF-1 [18]. LOX, which cross-links Col1 microfibrils, has recently been implicated in hypoxia-induced metastasis [51, 52]. LOX is regulated by HIF-1, and secreted LOX is responsible for the invasive/metastatic properties of hypoxic human cancer cells through focal adhesion kinase activity and cell-matrix adhesion [51, 52]. The gene expression analysis in our study revealed a significant increase in LOX expression under hypoxia in invasive/metastatic breast and prostate cancer cells alike, which is in good agreement with these studies [51, 52]. Col1 fiber density and volume will ultimately depend on the net balance between synthesis and degradation. The less dense, porous Col1 fiber matrix observed in hypoxic tumor regions suggests that degradation may have dominated over synthesis in chronically hypoxic tumor regions.

In summary, using combined SHG and fluorescence microscopy and a newly developed image analysis approach to quantify fiber structures, we have demonstrated that hypoxia resulted in a more porous and reduced Col1 fiber matrix in hypoxic regions of solid tumors *in vivo*. The use of SHG microscopic detection of Col1 fibers to assess ECM integrity, which is an intrinsic contrast mechanism, may prove clinically useful in the future in minimally invasive procedures, such as biopsies or ablations, in which a fiber-optic micro-endoscope can be implemented as part

of the biopsy or ablation needle. In normal tissue, Col1 fibers and the ECM, in general, are structured to guide interstitial fluid to the lymphatics [53]. Whereas hypoxia undoubtedly alters Col1 fibers in these human tumor xenograft models, the role of this Col1 restructuring in macromolecular transport and mediating cancer cell dissemination requires further investigation.

## **Acknowledgments**

The authors thank Scot Kuo for expert technical support with the microscopy studies on the Zeiss 710 NLO Meta confocal microscope equipped for multiphoton microscopy, Gary Cromwell for laboratory support, and David Bonekamp for his help in developing the Col1 fiber analysis software.

This work was supported by the National Institutes of Health grants P50 CA103175 and P30 CA006973

## **References**

1. Jain, R.K. (1988). Determinants of tumor blood flow: a review. *Cancer Res.* 48(10): 2641-58.
2. Tatum, J.L., G.J. Kelloff, R.J. Gillies, J.M. Arbeit, J.M. Brown, K.S. Chao, J.D. Chapman, W.C. Eckelman, A.W. Fyles, A.J. Giaccia, R.P. Hill, C.J. Koch, M.C. Krishna,

- K.A. Krohn, J.S. Lewis, R.P. Mason, G. Melillo, A.R. Padhani, G. Powis, J.G. Rajendran, R. Reba, S.P. Robinson, G.L. Semenza, H.M. Swartz, P. Vaupel, D. Yang, B. Croft, J. Hoffman, G. Liu, H. Stone, and D. Sullivan (2006). Hypoxia: importance in tumor biology, noninvasive measurement by imaging, and value of its measurement in the management of cancer therapy. *Int J Radiat Biol.* 82(10): 699-757.
3. Hockel, M. and P. Vaupel (2001). Tumor hypoxia: definitions and current clinical, biologic, and molecular aspects. *J Natl Cancer Inst.* 93(4): 266-76.
  4. Lochter, A. and M.J. Bissell (1995). Involvement of extracellular matrix constituents in breast cancer. *Semin Cancer Biol.* 6(3): 165-73.
  5. Chung, L.W., A. Baseman, V. Assikis, and H.E. Zhou (2005). Molecular insights into prostate cancer progression: the missing link of tumor microenvironment. *J Urol.* 173(1): 10-20.
  6. Pathak, A.P., D. Artemov, M. Neeman, and Z.M. Bhujwala (2006). Lymph node metastasis in breast cancer xenografts is associated with increased regions of extravascular drain, lymphatic vessel area, and invasive phenotype. *Cancer Res.* 66(10): 5151-8.
  7. Alexandrakis, G., E.B. Brown, R.T. Tong, T.D. McKee, R.B. Campbell, Y. Boucher, and R.K. Jain (2004). Two-photon fluorescence correlation microscopy reveals the two-phase nature of transport in tumors. *Nat Med.* 10(2): 203-7.
  8. Tuxhorn, J.A., G.E. Ayala, M.J. Smith, V.C. Smith, T.D. Dang, and D.R. Rowley (2002). Reactive stroma in human prostate cancer: induction of myofibroblast phenotype and extracellular matrix remodeling. *Clin Cancer Res.* 8(9): 2912-23.

9. Cooper, C.R., C.H. Chay, J.D. Gendernalik, H.L. Lee, J. Bhatia, R.S. Taichman, L.K. McCauley, E.T. Keller, and K.J. Pienta (2003). Stromal factors involved in prostate carcinoma metastasis to bone. *Cancer*. 97(3 Suppl): 739-47.
10. Provenzano, P.P., K.W. Eliceiri, J.M. Campbell, D.R. Inman, J.G. White, and P.J. Keely (2006). Collagen reorganization at the tumor-stromal interface facilitates local invasion. *BMC Med*. 4(1): 38.
11. Provenzano, P.P., D.R. Inman, K.W. Eliceiri, J.G. Knittel, L. Yan, C.T. Rueden, J.G. White, and P.J. Keely (2008). Collagen density promotes mammary tumor initiation and progression. *BMC Med*. 6: 11.
12. Li, T., L. Sun, N. Miller, T. Nicklee, J. Woo, L. Hulse-Smith, M.S. Tsao, R. Khokha, L. Martin, and N. Boyd (2005). The association of measured breast tissue characteristics with mammographic density and other risk factors for breast cancer. *Cancer Epidemiol Biomarkers Prev*. 14(2): 343-9.
13. Taboga, S.R. and C. Vidal Bde (2003). Collagen fibers in human prostatic lesions: histochemistry and anisotropies. *J Submicrosc Cytol Pathol*. 35(1): 11-6.
14. Zhang, Y., S. Nojima, H. Nakayama, Y. Jin, and H. Enza (2003). Characteristics of normal stromal components and their correlation with cancer occurrence in human prostate. *Oncol Rep*. 10(1): 207-11.
15. Colpaert CG, Vermeulen PB, Fox SB, Harris AL, Dirix LY, and Van Marck EA (2003). The presence of a fibrotic focus in invasive breast carcinoma correlates with the expression of carbonic anhydrase IX and is a marker of hypoxia and poor prognosis. *Breast Cancer Res Treat* 81, 137–147.

16. Van den Eynden GG, Colpaert CG, Couvelard A, Pezzella F, Dirix LY, Vermeulen PB, Van Marck EA, and Hasebe T (2007). A fibrotic focus is a prognostic factor and a surrogate marker for hypoxia and (lymph)angiogenesis in breast cancer: review of the literature and proposal on the criteria of evaluation. *Histopathology* 51, 440–451.
17. McPhail LD and Robinson SP (2010). Intrinsic susceptibility MR imaging of chemically induced rat mammary tumors: relationship to histologic assessment of hypoxia and fibrosis. *Radiology* 254, 110–118.
18. Hofbauer, K.H., B. Gess, C. Lohaus, H.E. Meyer, D. Katschinski, and A. Kurtz (2003). Oxygen tension regulates the expression of a group of procollagen hydroxylases. *Eur J Biochem.* 270(22): 4515-22.
19. Shoulders, M.D. and R.T. Raines (2009). Collagen structure and stability. *Annu Rev Biochem.* 78: 929-58.
20. Corpechot, C., V. Barbu, D. Wendum, N. Kinnman, C. Rey, R. Poupon, C. Housset, and O. Rosmorduc (2002). Hypoxia-induced VEGF and collagen I expressions are associated with angiogenesis and fibrogenesis in experimental cirrhosis. *Hepatology.* 35(5): 1010-21.
21. Rossert, J., C. Terraz, and S. Dupont (2000). Regulation of type I collagen genes expression. *Nephrol Dial Transplant.* 15 Suppl 6: 66-8.
22. Gong, L.M., J.B. Du, L. Shi, Y. Shi, and C.S. Tang (2004). Effects of endogenous carbon monoxide on collagen synthesis in pulmonary artery in rats under hypoxia. *Life Sci.* 74(10): 1225-41.

23. Kauppila, S., F. Stenback, J. Risteli, A. Jukkola, and L. Risteli (1998). Aberrant type I and type III collagen gene expression in human breast cancer in vivo. *J Pathol.* 186(3): 262-8.
24. Kao, R.T., J. Hall, and R. Stern (1986). Collagen and elastin synthesis in human stroma and breast carcinoma cell lines: modulation by the extracellular matrix. *Connect Tissue Res.* 14(4): 245-55.
25. Sabeh, F., I. Ota, K. Holmbeck, H. Birkedal-Hansen, P. Soloway, M. Balbin, C. Lopez-Otin, S. Shapiro, M. Inada, S. Krane, E. Allen, D. Chung, and S.J. Weiss (2004). Tumor cell traffic through the extracellular matrix is controlled by the membrane-anchored collagenase MT1-MMP. *J Cell Biol.* 167(4): 769-81.
26. Coussens, L.M., B. Fingleton, and L.M. Matrisian (2002). Matrix metalloproteinase inhibitors and cancer: trials and tribulations. *Science.* 295(5564): 2387-92.
27. Egeblad, M. and Z. Werb (2002). New functions for the matrix metalloproteinases in cancer progression. *Nat Rev Cancer.* 2(3): 161-74.
28. Andreasen, P.A., L. Kjoller, L. Christensen, and M.J. Duffy (1997). The urokinase-type plasminogen activator system in cancer metastasis: a review. *Int J Cancer.* 72(1): 1-22.
29. Falanga, V., L. Zhou, and T. Yufit (2002). Low oxygen tension stimulates collagen synthesis and COL1A1 transcription through the action of TGF-beta1. *J Cell Physiol.* 191(1): 42-50.
30. Horino, Y., S. Takahashi, T. Miura, and Y. Takahashi (2002). Prolonged hypoxia accelerates the posttranscriptional process of collagen synthesis in cultured fibroblasts. *Life Sci.* 71(26): 3031-45.

31. Brown, E., T. McKee, E. diTomaso, A. Pluen, B. Seed, Y. Boucher, and R.K. Jain (2003). Dynamic imaging of collagen and its modulation in tumors in vivo using second-harmonic generation. *Nat Med.* 9(6): 796-800.
32. Falzon, G., S. Pearson, and R. Murison (2008). Analysis of collagen fibre shape changes in breast cancer. *Phys Med Biol.* 53(23): 6641-52.
33. Raman, V., D. Artemov, A.P. Pathak, P.T. Winnard, Jr., S. McNutt, A. Yudina, A. Bogdanov, Jr., and Z.M. Bhujwala (2006). Characterizing vascular parameters in hypoxic regions: a combined magnetic resonance and optical imaging study of a human prostate cancer model. *Cancer Res.* 66(20): 9929-36.
34. Glunde, K., T. Shah, P.T. Winnard, Jr., V. Raman, T. Takagi, F. Vesuna, D. Artemov, and Z.M. Bhujwala (2008). Hypoxia regulates choline kinase expression through hypoxia-inducible factor-1 alpha signaling in a human prostate cancer model. *Cancer Res.* 68(1): 172-80.
35. Cailleau, R., R. Young, M. Olive, and W.J. Reeves, Jr. (1974). Breast tumor cell lines from pleural effusions. *J Natl Cancer Inst.* 53(3): 661-74.
36. Kaighn, M.E., K.S. Narayan, Y. Ohnuki, J.F. Lechner, and L.W. Jones (1979). Establishment and characterization of a human prostatic carcinoma cell line (PC-3). *Invest Urol.* 17(1): 16-23.
37. Glunde, K., C. Jie, and Z.M. Bhujwala (2004). Molecular causes of the aberrant choline phospholipid metabolism in breast cancer. *Cancer Res.* 64(12): 4270-6.
38. Ackerstaff, E., D. Artemov, R.J. Gillies, and Z.M. Bhujwala (2007). Hypoxia and the presence of human vascular endothelial cells affect prostate cancer cell invasion and metabolism. *Neoplasia.* 9(12): 1138-51.

39. Glunde, K., C.A. Foss, T. Takagi, F. Wildes, and Z.M. Bhujwala (2005). Synthesis of 6'-O-lissamine-rhodamine B-glucosamine as a novel probe for fluorescence imaging of lysosomes in breast tumors. *Bioconjug Chem.* 16(4): 843-51.
40. Irizarry, R.A., B. Hobbs, F. Collin, Y.D. Beazer-Barclay, K.J. Antonellis, U. Scherf, and T.P. Speed (2003). Exploration, normalization, and summaries of high density oligonucleotide array probe level data. *Biostatistics.* 4(2): 249-64.
41. Bolstad, B.M., R.A. Irizarry, M. Astrand, and T.P. Speed (2003). A comparison of normalization methods for high density oligonucleotide array data based on variance and bias. *Bioinformatics.* 19(2): 185-93.
42. Semenza, G.L. (2000). Expression of hypoxia-inducible factor 1: mechanisms and consequences. *Biochem Pharmacol.* 59(1): 47-53.
43. Semenza, G.L. (2002). HIF-1 and tumor progression: pathophysiology and therapeutics. *Trends Mol Med.* 8(4 Suppl): S62-7.
44. Cha, H.S., K.S. Ahn, C.H. Jeon, J. Kim, Y.W. Song, and E.M. Koh (2003). Influence of hypoxia on the expression of matrix metalloproteinase-1, -3 and tissue inhibitor of metalloproteinase-1 in rheumatoid synovial fibroblasts. *Clin Exp Rheumatol.* 21(5): 593-8.
45. Guo, W.J., J. Li, Z. Chen, J.Y. Zhuang, W.H. Gu, L. Zhang, J. Pang, C.H. Lu, W.Z. Zhang, and Y.F. Cheng (2004). Transient increased expression of VEGF and MMP-1 in a rat liver tumor model after hepatic arterial occlusion. *Hepatogastroenterology.* 51(56): 381-6.



46. Kan, C., M. Abe, M. Yamanaka, and O. Ishikawa (2003). Hypoxia-induced increase of matrix metalloproteinase-1 synthesis is not restored by reoxygenation in a three-dimensional culture of human dermal fibroblasts. *J Dermatol Sci.* 32(1): 75-82.
47. Kondo, S., S. Kubota, T. Shimo, T. Nishida, G. Yosimichi, T. Eguchi, T. Sugahara, and M. Takigawa (2002). Connective tissue growth factor increased by hypoxia may initiate angiogenesis in collaboration with matrix metalloproteinases. *Carcinogenesis.* 23(5): 769-76.
48. Ottino, P., J. Finley, E. Rojo, A. Otlecz, G.N. Lambrou, H.E. Bazan, and N.G. Bazan (2004). Hypoxia activates matrix metalloproteinase expression and the VEGF system in monkey choroid-retinal endothelial cells: Involvement of cytosolic phospholipase A2 activity. *Mol Vis.* 10: 341-50.
49. Graham, C.H., J. Forsdike, C.J. Fitzgerald, and S. Macdonald-Goodfellow (1999). Hypoxia-mediated stimulation of carcinoma cell invasiveness via upregulation of urokinase receptor expression. *Int J Cancer.* 80(4): 617-23.
50. Lash, G.E., T.E. Fitzpatrick, and C.H. Graham (2001). Effect of hypoxia on cellular adhesion to vitronectin and fibronectin. *Biochem Biophys Res Commun.* 287(3): 622-9.
51. Erler, J.T., K.L. Bennewith, M. Nicolau, N. Dornhofer, C. Kong, Q.T. Le, J.T. Chi, S.S. Jeffrey, and A.J. Giaccia (2006). Lysyl oxidase is essential for hypoxia-induced metastasis. *Nature.* 440(7088): 1222-6.
52. Erler, J.T. and A.J. Giaccia (2006). Lysyl oxidase mediates hypoxic control of metastasis. *Cancer Res.* 66(21): 10238-41.
53. Pepper, M.S., J.C. Tille, R. Nisato, and M. Skobe (2003). Lymphangiogenesis and tumor metastasis. *Cell Tissue Res.* 314(1): 167-77. Epub 2003 Jul 18.



## Chapter 3

---

### Collagen I fiber density increases in lymph node positive breast cancers in a pilot study

Published in: **Journal of Biomedical Optics**, 2012 Nov;17(11)  
Collagen I fiber density increases in lymph node positive breast cancers in a pilot study.  
**Samata M. Kakkad**, Meiyappan Solaiyappan, Pedram Argani, Saraswati Sukumar,  
Lisa K. Jacobs, Dieter Leibfritz, Zaver M. Bhujwala, and Kristine Glunde

## **Abstract**

Collagen I (Col1) fibers are a major structural component in the extracellular matrix of human breast cancers. In a preliminary pilot study, we have explored the link between Col1 fiber density in primary human breast cancers and the occurrence of lymph node metastasis. Col1 fibers were detected by second harmonic generation (SHG) microscopy in primary human breast cancers from patients presenting with lymph node metastasis (LN+) versus without lymph node metastasis (LN-). Col1 fiber density, which was quantified using our in-house SHG image analysis software, was significantly higher in the primary human breast cancers of LN+ (fiber volume =  $29.22 \pm 1.67\%$ , inter-fiber distance =  $2.25 \pm 0.17 \mu\text{m}$ ) versus LN- (fiber volume =  $20.33 \pm 2.27\%$ , inter-fiber distance =  $2.88 \pm 0.44 \mu\text{m}$ ) patients. Texture analysis by evaluating the co-occurrence matrix and the Fourier transform of the Col1 fibers proved to be significantly different for the parameters of co-relation and energy, as well as aspect ratio and eccentricity for LN+ versus LN- cases. We also demonstrated that tissue fixation and paraffin-embedding had negligible effect on SHG Col1 fiber detection and quantification. High Col1 fiber density in primary breast tumors is associated with breast cancer metastasis and may serve as an imaging biomarker of metastasis.

## **Introduction**

The extracellular matrix (ECM) in primary breast cancers is significantly altered compared to normal breast tissue and may provide new biomarkers for cancer diagnosis [1-4], metastasis prediction [5, 6], and prognosis of survival [7]. Cancer metastasis is a multistep process in which the tumor microenvironment (TME) facilitates cancer cell-ECM interactions

that are necessary for metastasis to occur [8]. The ECM in breast tumors is composed of a complex meshwork of fibrillar collagens, glycoproteins, and proteoglycans [9], which profoundly affect metastasis, as well as proliferation, angiogenesis, adhesion, migration, invasion, macromolecular transport, and drug delivery [9-13]. Multiple molecular mechanisms such as ECM degradation by proteases secreted by cancer cells, and dysregulated ECM synthesis by tumor-associated stromal cells have been implicated in the formation of the significantly altered ECM of breast tumors [8] that include structural changes in the fiber patterns of fiber-forming ECM components. Col1 fibers are the major structural ECM component in breast tumors [5, 6, 9, 14, 15], and increased stromal Col1 has been found to facilitate breast tumor formation, invasion, and metastasis [5, 6].

X-ray mammography, which detects radiodense fibroglandular tissue in the breast, demonstrated that women with high (50% to 74% versus <5%) breast density have a 4.64-fold increased risk of developing breast carcinoma [16, 17]. Histologic evaluation of biopsy and mastectomy specimens from X-ray mammographically dense breast regions revealed a significantly higher collagen density and extent of fibrosis in these regions [14, 15]. High Col1 fiber density significantly increased mammary tumor initiation, progression, and lung metastasis [6]. Cancer cell invasion in this mouse model started at the tumor-stromal interface in the primary tumor along radially aligned Col1 fibers, which can form avenues for metastasis [5]. In a recent study, Col1 fibers that were oriented perpendicular to the cancer cell boundaries were found to serve as a prognostic signature for survival of breast carcinoma patients [7].

Here we have, for the first time, performed a pilot study to test the relationship between lymph node metastasis and Col1 fiber texture and density in primary human breast cancers using second harmonic generation (SHG) microscopy. SHG microscopy detects an intrinsic signal generated by the noncentrosymmetric physical properties of Col1 fibers, and does not require the use of an exogenous optical imaging agent [3, 4, 18]. We have performed a small retrospective SHG microscopy study to determine if the Col1 fiber signature in primary breast tumors is altered in patients presenting with lymph node metastasis compared to patients with uninvolved lymph nodes. We used our in-house automated fiber analysis software as previously described [19], which is free of user variability and observed that primary breast cancers in LN+ patients have significantly denser Col1 fiber signatures than primary breast cancer in LN- patients. To validate our in-house software results, we additionally used two commonly used texture analysis techniques to analyze Col1 images [20-22]: the gray level co-occurrence matrix (GLCM) and the Fourier transform (FT). We observed that the GLCM parameters co-relation and energy and the FT parameters aspect ratio and eccentricity were significantly different for the Col1 fiber distribution in LN+ cases as compared to the LN- cases. We also demonstrated that tissue fixation and paraffin-embedding had no effect on SHG Col1 fiber detection and quantification, indicating that Col1 fiber assessment by nondestructive SHG microscopy may be implemented in routine clinical pathology settings.

## **Materials and Methods**

### *Ethics Statement*

An exemption for retrospective analysis of de-identified human breast tumor specimens was approved by the Institutional Review Board of the Johns Hopkins University School of Medicine as these specimens were not collected specifically for this particular research project, and the identity of the individuals to whom the specimens pertain was unknown to everyone involved in this research project. Research that involves only coded human biological specimens is not human subjects research under the human subjects regulations of the US Department of Health and Human Services.

All experimental animal protocols were approved by the Institutional Animal Care and Use Committee of the Johns Hopkins University School of Medicine under the animal protocol number MO08M166 and under the Animal Welfare Assurance Number A3272-01.

#### *Tumor Xenograft Specimens*

To test if different types of tissue processing affect the SHG Col1 fiber signals, we used a xenograft model system of human breast tumors instead of valuable patient material. MCF-7, a nonmetastatic, estrogen-sensitive (estrogen-dependent) line, was orthotopically inoculated in the upper left thoracic mammary fat pad of female athymic nude mice to grow breast tumor xenografts. MCF-7 breast cancer cells were purchased from the American Type Culture Collection (ATCC) and used within 6 months of obtaining them from ATCC. The MCF-7 cell line was tested and authenticated by ATCC by two independent methods: the ATCC cytochrome

C oxidase I PCR assay and short tandem repeat profiling using multiplex PCR. For MCF-7 cell inoculations, 0.18 mg of a 60-day release 17 $\beta$ -estradiol pellet (Innovative Research of America) was subcutaneously implanted near the left shoulder of athymic nude mice 1 week before inoculation. Two million MCF-7 cells were inoculated in a volume of 0.05 mL HBSS (Sigma; no Matrigel was used). Tumor size was about 500 mm<sup>3</sup> when animals were sacrificed and tumors were removed. To assess if tissue processing affects SHG-detected Col1 fiber patterns, each tumor was cut into three equal-sized parallel-cut pieces. One piece was formalin-fixed paraffin-embedded (FFPE), a second piece of the same tumor was put on a microscope slide and kept in an ice-box for immediate fresh-tissue SHG imaging, and a third piece of the tumor was placed in Tissue Tek OCT freezing compound (Sakura Finetek USA, Inc, Torrance, CA), cryosectioned with a microcryotome (Microm International, Walldorf, Germany) at 100  $\mu$ m thickness, fixed with 4% paraformaldehyde (Sigma-Aldrich) solution, and mounted with Faramount aqueous mounting medium (DakoCytomation, Carpinteria, CA).

### *Breast Cancer Specimens*

We retrospectively analyzed 14 breast cancer tissues, all of which were invasive ductal carcinomas (IDC). Eight of these breast cancers were LN+ and 6 were LN-. All cancers were tumor grade 2-3, estrogen receptor positive (ER+), and progesterone receptor positive (PR+). All of our samples were obtained from hospitals in Maryland and were graded by board-certified breast pathologists including Dr. Pedram Argani. Snap-frozen primary breast tumor specimens were placed in Tissue Tek OCT freezing compound (Sakura Finetek USA, Inc, Torrance, CA), cryosectioned with a microcryotome (Microm International, Walldorf, Germany) at 100  $\mu$ m



thickness for whole mount sections and 5  $\mu\text{m}$  thickness for adjacent sections, fixed with 4% paraformaldehyde (Sigma-Aldrich) solution, stained for nuclei with Hoechst 33342 (Invitrogen Corp, Carlsbad, CA), and mounted with Faramount aqueous mounting medium (DakoCytomation, Carpinteria, CA) as previously described [19]. For testing the within-tumor consistency of SHG-detected Col1 inter-fiber distances and Col1 fiber volume, we obtained FFPE samples from four different biopsy passes of the same breast cancer for four human specimens, which were grade 3, LN+, ER+, and PR+; grade 2, LN+, ER+, PR+; grade 2, LN-, ER+, PR+; and grade 3, LN+, ER+, PR-. These FFPE samples were embedded in paraffin blocks, within which they were marked with the pink dye phloxine, which visualizes the shape of the biopsy specimen within the white paraffin block. We also obtained the adjacent H&E slide. In our pathology lab, the H&E section is always cut as the last slide in the series that is cut from a given FFPE block. Therefore it was possible to spatially correlate the shape of the hematoxylin and eosin (H&E) section with the specimen in the FFPE block.

### *SHG Imaging*

SHG microscopy was performed on a Zeiss LSM 710 NLO Meta confocal microscope (Carl Zeiss MicroImaging, Inc, Thornwood, NY) equipped with a 680–1080 nm tunable Coherent Chameleon Vision II laser with automated pre-compensation (Coherent, Inc, Santa Clara, CA) located in the Johns Hopkins University School of Medicine (JHU SOM) Microscope Core Facility (directed by Dr. Scot Kuo). Incident laser light of 880 nm was used for generating the SHG Col1 signal and laser light of 760 nm for two-photon excitation of Hoechst 33342. The laser power used was about 10 mW for the 880 nm channel and about 19 mW for the 760 nm

channel. The SHG signal was detected within 410–450 nm, and the Hoechst fluorescence was detected within 400–475 nm. Six to ten random fields of view (FOVs) per sample that were equidistantly spread throughout the breast tumor specimen were imaged to provide a realistic representation of each breast cancer sample. At each FOV, we acquired a z-stack of 100  $\mu\text{m}$  total thickness with a z-interval of 5  $\mu\text{m}$  using a 25x/0.8 LD LCI PlanApo multi-immersion lens. The corresponding images of adjacently cut H&E stained 5-mm thick sections were used to verify that all samples contained cancer. Brightfield microscopy of the H&E-stained adjacent sections was performed using a Nikon inverted microscope equipped with a Nikon Coolpix digital camera (Nikon Instruments, Inc, Melville, NY). For testing the within-tumor consistency using FFPE blocks of different biopsy passes, we additionally performed tile-function imaging covering the entire biopsy sample for two biopsy passes, again acquiring z-stacks of 100  $\mu\text{m}$  total thickness with a z-interval of 5  $\mu\text{m}$  using the 25x lens.

### *Coll Fiber Quantification*

To quantify our data independent of SHG signal intensity and free of errors introduced by user variability, we used automated geometric analysis and texture analysis techniques. We used a geometric analysis technique, where the parameters of fiber volume and inter-fiber distance were calculated. Image analysis to quantify the Coll inter-fiber distance and the Coll fiber volume was performed using in-house software as previously described [19]. This software was written in Matlab using MATLAB 7.4.0 (TheMathWorks, Natick, MA) and was previously described in detail [19]. Briefly, our software quantifies the median of all Coll inter-fiber distances and the total Coll fiber volume as outlined in Figure 1. A representative z-plane of a

raw image is shown in Figure 1A, which is preprocessed to exclude noise and nonfibrillar shapes as demonstrated in the schematic in Figure 1B, resulting in the extraction of Col1 fiber structures from the raw images as shown in Figure 1C. As indicated in Figure 1D, Euclidean distances from each empty voxel to the nearest Col1 fiber voxel were computed within each three-dimensional FOV to quantify the inter-fiber distances and the total fiber volume from the Col1 fiber mesh. Based on a previous report, we expected more tightly packed Col1 fibers and a higher fiber volume for LN+ cases as compared to LN- cases [6]. Therefore, a one-sided t-test ( $\alpha = 0.05$ ) was used to detect significant differences in the Col1 inter-fiber distance and the Col1 fiber volume between primary tumors from LN- versus LN+ cases using Microsoft Office Excel 2007 (Microsoft, Redmond, WA). P values of  $< 0.05$  were considered to be significant. P values of  $0.10 > P > 0.05$  were considered to be a trend towards significance [23].

To validate our analysis results, we also used well-established texture analysis methods for Col1 fiber quantification [20-22], to see if the Col1 fiber distributions were significantly different for the LN- and LN+ cases as observed in our geometric analysis. We used the gray level co-occurrence matrix (GLCM) and Fourier transform (FT) texture analysis to analyze Col1 fiber distributions. Several textural features were extracted by GLCM, which is a statistical texture analysis method based on the second order statistics of an image's gray scale histogram [24]. This analysis was done in Matlab using MATLAB 7.4.0 (TheMathWorks, Natick, MA). The extracted features include: 1) Contrast, which is a measure of intensity variation, with a contrast = 0 for a constant image, and a range = [0 1]; 2) Co-relation, which is a measure of how a pixel is co-related to its neighboring pixel, with 1 for positively and -1 for negatively co-related pixels, and a range = [-1 1]); 3) Energy, which is also known as uniformity or angular second

moment, with an energy = 1 for a constant image, and a range = [0 1]; and 4) Homogeneity, which is a property measure of how homogeneous an image is, with a value = 1 for a constant image, and a range = [0 1] [25]. We also calculated the two-dimensional FT for all images. For randomly distributed Col1 fibers the resulting FT approximates a circle, while for a more organized fiber pattern, the FT looks elliptical. FT features were obtained by fitting an ellipse to the FT of each image and include: 1) Aspect ratio (AR), which is the ratio of the major axis to the minor axis of the ellipse; 2) Orientation, which is the angle between the x-axis and the major axis of the ellipse; and 3) Eccentricity, which is the ratio of the distance between the foci of the ellipse and the length of the major axis. For a circle, the eccentricity is 0, and its range = [0 1]. A one-sided t-test ( $\alpha = 0.05$ ) was used to detect significant differences in the Col1 texture for all above parameters between primary tumors from LN- versus LN+ cases using Microsoft Office Excel 2007 (Microsoft, Redmond, WA). P values of  $< 0.05$  were considered to be significant.

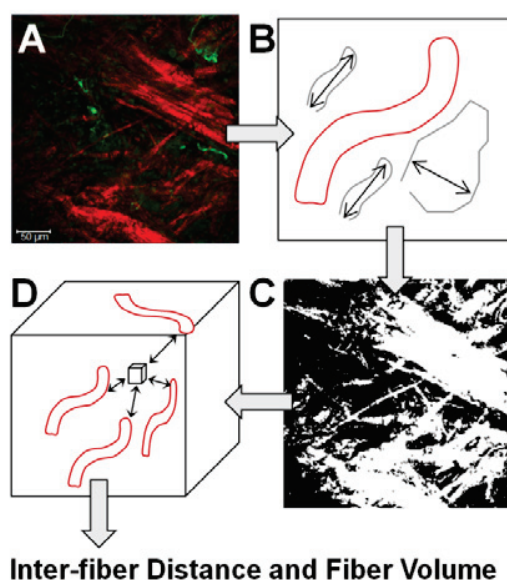


**Figure 1:** Construction of inter-fiber distance and fiber volume: (A) composite image of the Col1 fibers (red) and cell nuclei (green); preprocessing using the optional filter (B) to identify fiber-like objects (red) among various non-fiber-like objects in the image to produce (C) the corresponding Col1 fiber image; (D) computing the distances from each 3D voxel to the surrounding fibers in 3D to determine the nearest distance to a fiber in [ $\mu\text{m}$ ] and the total fiber volume [%]. One z-plane from a 3D image stack is displayed in A and C. Each image size is  $339 \mu\text{m} \times 339 \mu\text{m}$ . The scale bars represent  $50 \mu\text{m}$ .

## Results

To test if the SHG microscopic detection of Col1 fiber signatures depends on tissue processing, we compared fresh tissue samples with formaldehyde-fixed, Hoechst-stained whole-mount sections and with FFPE samples from the same MCF-7 breast tumor xenograft. The data presented in Figure 2 demonstrate that SHG microscopy effectively revealed Col1 fiber signatures in this breast tumor xenograft model. We found that the Col1 fiber distribution in tissues under these different preparations were fairly consistent. Figure 2A-C shows that the Col1 fiber structures were stable and remained unaltered in the same MCF-7 breast tumor xenograft that was first imaged fresh, and from which adjacent sections were re-imaged after 4%-paraformaldehyde-fixation and Hoechst 33342-staining, or after formalin-fixation and paraffin-embedding within FFPE blocks. The Col1 fiber volume (Figure 2D) and inter-fiber distance (Figure 2E) from 5 randomly selected fields of views (FOVs) detected from each sample preparation revealed no changes between the same tissue that was fresh, fixed, or paraffin-embedded. These results suggest that tissues with different preparations (fresh, fixed, or FFPE) can be used for SHG-Col1 imaging studies without introducing artifacts, although in practice, tissue processing within each experimental set-up should be kept consistent to avoid any potential variations across different types of tissue preparations.

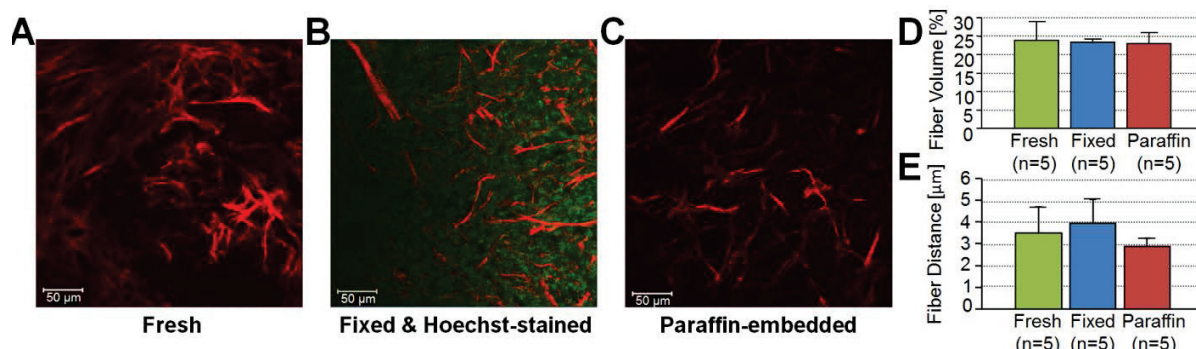


**Figure 2:** The SHG signal is robust and independent of tissue processing. We obtained comparable images from (A) fresh, (B) fixed and Hoechst-stained, and (C) paraffin-embedded MCF-7 breast tumor xenograft tissue, consistent with (D) almost identical results obtained by fiber volume and (E) inter-fiber distance quantification of 5 randomly selected fields of views (FOVs) from each differently processed tissue. Each image size is 339 μm x 339 μm. The scale bars represent 50 μm.

We compared the Col1 fiber signatures in the primary tumors of LN- and LN+ patients in an initial proof-of-principle pilot study. As evident in Figure 3, denser SHG Col1 fiber signatures were detected in primary tumor specimens from 8 LN+ patients compared to those from 6 LN- patients. We quantified 10 randomly selected, equidistant FOVs from each primary tumor to assess global Col1 changes. This approach accounts for the possibility that Col1 fiber architecture can be spatially heterogeneous within a given tumor. The image quantification software described above was used to quantify the Col1 fiber volume (Figure 3C) and distance (Figure 3D) in this geometric analysis. The Col1 fiber volume significantly ( $p=0.0036$ ,  $n=6-8$ , values are mean±standard deviation) increased from  $20.33 \pm 5.56\%$  in LN- to  $29.22 \pm 4.72\%$  in LN+ patients. The Col1 inter-fiber distance showed a trend towards significance ( $p=0.0807$ ,  $n=6-8$ , values are mean±standard deviation) and decreased from  $2.88 \pm 1.07 \mu\text{m}$  in LN- to  $2.25 \pm 0.45 \mu\text{m}$  in LN+ patients (Figure 3). The primary tumors of all patients were positive for estrogen receptor (ER) and progesterone receptor (PR). Hence ER and PR status were the same in all patients and were not confounding factors in this comparison.

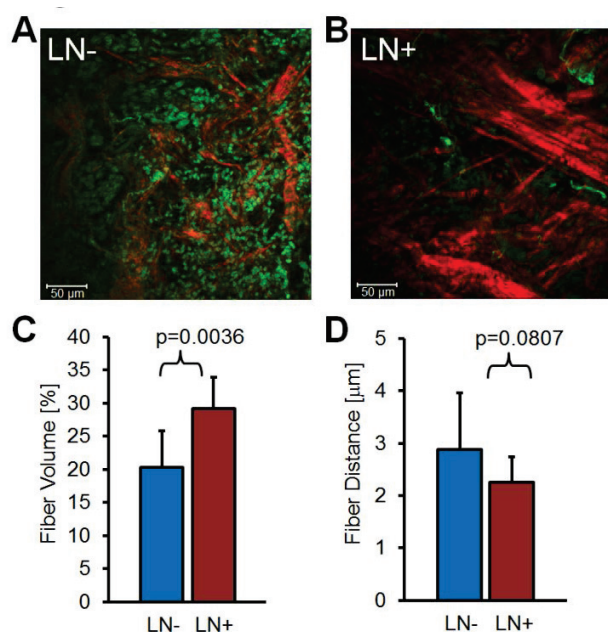


**Figure 3:** Primary breast tumors from LN+ patients contained denser Col1 fibers than primary tumors from LN- patients. Shown are representative SHG Col1 fiber (red) images from a (A) LN- patient and a (B) LN+ patient. Nuclei were counterstained with Hoechst (green). Each image size is 339 μm x 339 μm, one z-plane is displayed. The scale bars represent 50 μm. LN- patients (n=6) displayed (C) significantly (p=0.0036) decreased fiber volume and (D) and a trend (p=0.0807) toward increased inter-fiber distance compared to LN+ patients (n=8). Values are mean ± standard deviation.

To validate our geometric analysis of the differences observed in Col1 fiber distribution of LN- versus LN+ patients, we used different texture analysis methods to quantify the fiber patterns in a manner that is independent of the SHG signal intensity. We analyzed the same FOVs as used for the geometric analysis using GLCM and FT methods. We observed that the GLCM parameters co-relation and energy (Figure 4A) significantly separated the LN- and LN+ patients (p=0.0007 and p= 0.01788, respectively). The Col1 fibers in LN- samples had a significantly lower co-relation (LN- mean=0.44, LN+ mean=0.67, p=0.0007) and a significantly higher energy value (LN- mean=0.47, LN+ mean=0.28, p=0.01788) as compared to the fibers in LN+ samples. These parameters of higher co-relation and lower energy in LN+ versus LN- cases indicate that LN+ samples had more and denser Col1 fibers than LN- samples, which is

consistent with our geometric analysis results. In Figure 4B, we show that the FT parameters aspect ratio (AR) and eccentricity were significantly different for the LN- and LN+ patient samples ( $p=0.0557$  and  $p=0.0462$ , respectively). The LN- samples had a significantly higher AR (LN- mean=1.9, LN+ mean=1.45,  $p=0.057$ ) and a significantly higher eccentricity (LN- mean=0.74, LN+ mean=0.66,  $p=0.0462$ ) as compared to the LN+ samples. The FT analysis parameters AR and eccentricity were able to distinguish between LN+ and LN- samples. However, because the spatial information is lost in FT analysis, it was not possible in our case to interpret the decrease in AR and eccentricity in LN+ versus LN- patients in terms of geometric fiber parameters.

To assess if local Col1 fiber differences in a given tumor affect global Col1 fiber measurements obtained by analyzing and quantifying 10 randomly selected, equidistant FOVs from each primary tumor (N=14), we determined the spatial heterogeneity of the Col1 fiber architecture in breast tumor specimens. This assessment is necessary because with microscopic techniques, such as SHG Col1 fiber imaging, the FOV is in the range of hundreds of microns, while clinical breast tumors typically span larger diameters. Therefore, it is necessary to test if the differences in Col1 fiber density globally span the tumor, or are local phenomena. Our data presented in Figure 5 show that the Col1 inter-fiber distance distribution and fiber volume are almost identical in four biopsy passes that were obtained from the same human breast tumor specimen. In addition, the overall averages of a Col1 fiber volume of  $25 \pm 3\%$  and distance of  $3.0 \pm 0.4 \mu\text{m}$  for the tile-imaged biopsy pass B1 are comparable to the averages from 6 FOVs per biopsy pass (Figure 5). Comparable results were obtained for a total of four primary breast tumor cases, where the Col1 fiber volumes and inter-fiber distances for six equidistant FOVs



from four separate biopsy passes from each one of the four tumors gave comparable results (null hypothesis of the T-test was true, i.e.  $p$ -value  $>0.05$  for all breast tumor cases;  $N=4$ ). While there is some heterogeneity in the Col1 fiber architecture in breast tumor specimens, our approach of measuring and averaging over several randomly selected, equidistant FOVs that cover the entire tumor/biopsy averages out local fiber heterogeneity and detects overall global changes in Col1 fiber signature. Our data indicate that global Col1 fiber alterations in breast tumors dominate local Col1 fiber differences.

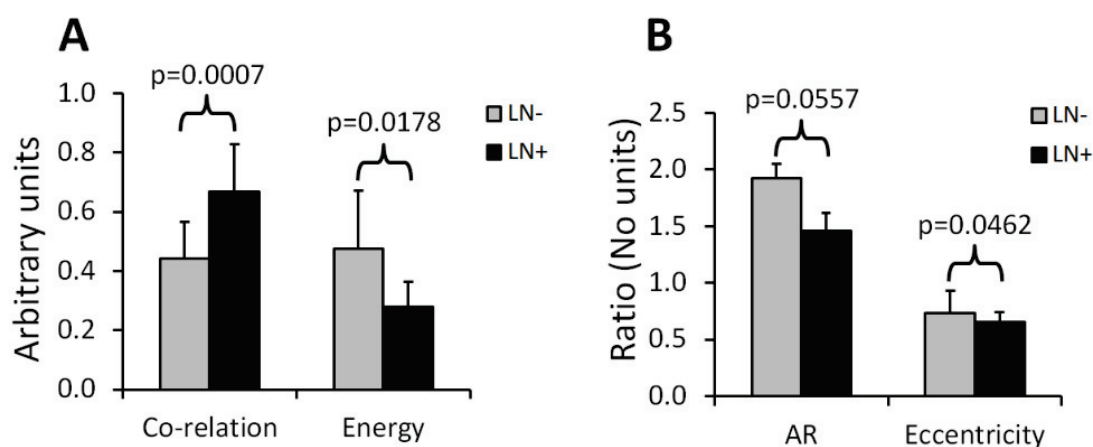


**Figure 4:** GLCM and FT texture analyses of Col1 fibers in primary breast tumors were able to distinguish between LN+ and LN- patients. **(A)** GLCM parameters showed that LN- patients ( $n=6$ ) displayed a significantly decreased inter-fiber co-relation ( $p=0.0007$ ) and significantly higher energy uniformity ( $p=0.0178$ ) as compared to LN+ patients ( $n=8$ ). Texture analysis using FT demonstrated that **(B)** the Col1 fiber distribution of LN- patients ( $n=6$ ) had a significantly higher aspect ratio (AR,  $p=0.0572$ ) and significantly higher eccentricity value ( $p=0.0462$ ) as compared to LN+ patients ( $n=8$ ). Values are mean  $\pm$  standard deviation.

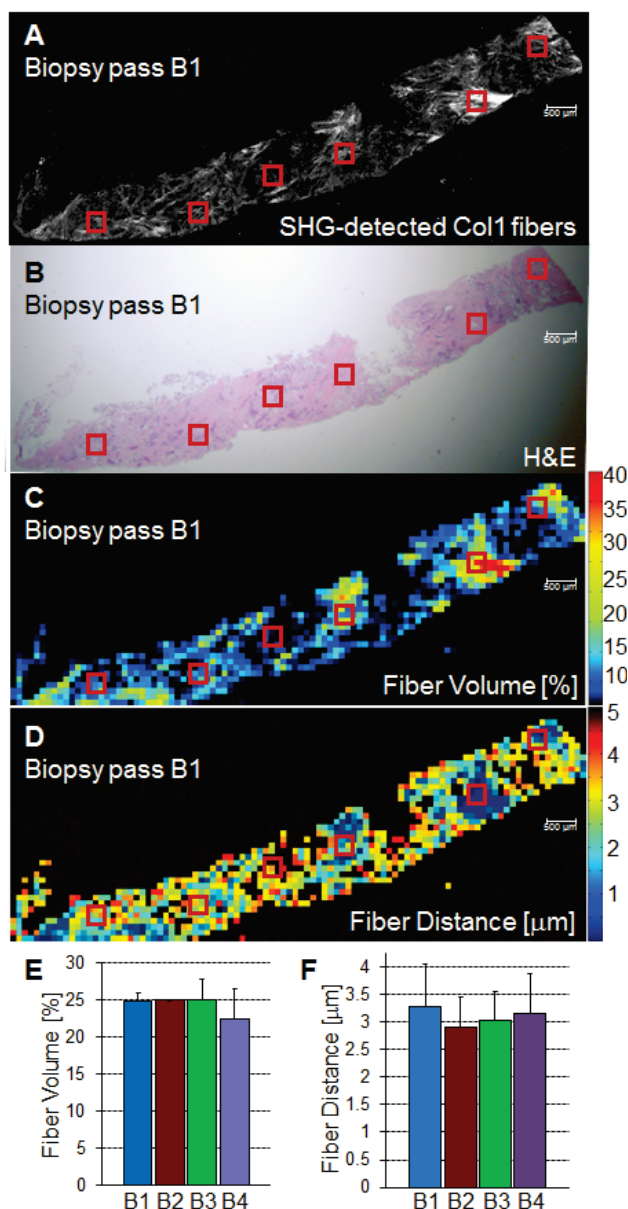


**Figure 5:** (A) SHG tile imaging covering breast tumor biopsy B1 and (B) the adjacent hematoxylin and eosin stained section. (C) Fiber Volume and (D) Fiber Distance were quantified with our software on a FOV by FOV basis covering the entire biopsy pass B1 to visualize the spatial heterogeneity by heat maps. Representative, average fiber volume and inter-fiber distance of the 3D data stack is displayed in 2D (C and D). Six randomly selected FOVs (marked in red/black) in this biopsy were analyzed for their Col1 fiber distribution. Four biopsy passes B1 (shown), B2, B3, and B4 taken from the same LN+ breast tumor were analyzed for their Col1 fiber (E) volume and (F) distance and displayed close to identical values for both parameters. Values are mean  $\pm$  standard deviation. These findings demonstrate that robust global changes in Col1 fiber architecture occur in malignant breast tumors, which can be reliably quantified by randomly selecting six FOVs. Each image size is 9862  $\mu\text{m}$  x 4080  $\mu\text{m}$ . The scale bars represent 500  $\mu\text{m}$ .

## Discussion

The presence or absence of metastases in axillary lymph nodes is currently the most important predictor of prognosis in breast carcinoma, and an integral component of the breast cancer staging system [26, 27]. Using ex vivo primary tumor specimens from patients, we observed increased Col1 fiber density in LN+ compared to LN- patients ( $p=0.0036$ ,  $N=14$ ) and significantly varied fiber distributions as obtained by our texture analysis (correlation,  $p=0.0007$ ; energy,  $p=0.0179$ ; AR,  $p=0.0557$ ; eccentricity,  $p=0.0462$ ;  $N=14$ ). Our data are in good agreement with a recent study that identified a tumor-associated Col1 signature (TACS) of bundles of straightened and aligned Col1 fibers that are oriented perpendicular to the tumor boundary as an independent prognostic marker for poor survival in patients with this TACS in their primary tumors [7]. While this larger clinical study scored for disease-free survival in 196 patient samples on human breast carcinoma tissue microarrays, our study more specifically compared primary tumors from LN+ and LN- patients in an initial proof-of-principle study. Unlike the study by Conklin et al. [7] that relied on a qualitative yes-no judgment performed by trained persons without software involvement or quantification, data analysis in our study was done by an in-house automated software that quantifies inter-fiber distance and fiber volume from raw Col1-SHG images. A major advantage of this automated analysis approach is that it is free of errors from subjective judgement, and that it can give quantitative results in real-time. By averaging over [6-10] FOVs that were equidistantly spread throughout each breast tumor specimen, we were able to obtain robust quantitative results ( $N=14$ , total number of tissue samples). Our data are also in good agreement with preclinical findings in a bi-transgenic mouse model, in which high Col1 fiber density promoted mammary tumor initiation, progression, and metastasis [6], and provide the first patient data linking lymph node metastasis with Col1 fiber

density. In addition, recent studies demonstrated that high Col1 fiber density in primary tumors can facilitate metastasis by providing dense Col1 fiber avenues along which cancer cells migrate to ultimately establish distant colonies [5, 6]. In these studies the initial invasion of breast cancer cells at the tumor-stromal interface was shown to occur along radially aligned Col1 fibers in the primary tumor [5, 6]. Breast cancer cells invade into Col1 matrices by overexpressing integrins on their cell surface, which enable these cells to adhere to the Col1-containing ECM [28, 29]. Cancer cells migrate through lymphatic vessels to the connected sentinel lymph node to establish metastatic growth [30-33]. Since lymphatic vessels are attached to collagen through anchoring filaments [34-36], future studies should focus on identifying if Col1 fibers guide migrating cancer cells into tumor-associated lymphatic vessels within the primary tumor.

In the clinic, the lymph node status is typically assessed by a sentinel lymph node biopsy, where the ‘sentinel nodes’ draining the lymphatic basin containing the tumor are identified and excised. This biopsy is typically performed at about 3 weeks after the initial breast biopsy [27] to identify and histologically examine axillary lymph nodes that are at high risk of containing cancer cells [27]. There is a 25% adverse event rate after sentinel lymph node biopsy, with 9% of patients having axillary paresthesia, 6% having lymphedema, 6% having axillary seromas, and 3% having wound infections [27]. Avoiding the sentinel lymph node biopsy procedure would eliminate these risks for those patients that are LN-. If the sentinel lymph nodes cannot be identified, additional axillary lymph node dissection is performed, which causes even more adverse surgical effects than the sentinel lymph node biopsy alone [27]. Therefore, novel biomarkers that alone, or when integrated with other standard markers, accurately predict for lymph node metastasis are critically needed. Our data suggest that SHG imaging of Col1 fibers

may serve as a surrogate marker to predict the presence of lymph node metastasis, which is in good agreement with the study by Conklin et al. [7] that showed that a specific TACS was able to predict survival. Col1 fibers were detected by optical second harmonic generation (SHG) microscopy, a highly sensitive and non-destructive technique that images intrinsic signal from Col1 fibers [4, 18, 37, 38]. Several other breast cancer markers have been associated with axillary lymph node metastasis such as CCND1, CD44, COX-2, EGFR, HER2/NEU, HPA, and LYVE-1 (reviewed in [39]). In addition, increased expression of vascular endothelial growth factor-C (VEGF-C) or VEGF-A, both of which are able to promote lymphangiogenesis in primary tumors, correlated with an increased incidence of regional lymph node as well as distant metastases in humans and animals [30-32]. Different techniques assessing protein expression, mRNA expression, chromosome alterations, and DNA copy number changes are being used to evaluate these markers of lymph node metastasis in primary breast tumors [39]. The advantage of SHG-detection of Col1 fibers as a biomarker of lymph node metastasis is that the technique is non-destructive and can be used to interrogate live tissues.

Our data show that the global Col1 fiber architecture in a given breast cancer is an important parameter, which dominates local Col1 fiber differences within the tissue. Our approach of probing several randomly selected, equidistant FOVs covering the entire tumor/biopsy to average out local fiber heterogeneity ensures that we are measuring global Col1 fiber architecture, which is quantified by the parameters Col1 fiber volume and inter-fiber distance. We previously observed in an orthotopic human breast tumor xenograft model that hypoxic tumor microenvironments reduce Col1 fiber density and increase Col1 inter-fiber distance [19]. Some of the occurring local heterogeneity in the Col1 fiber architecture of human

breast cancers may be due to hypoxic regions in these tumors. To implement SHG microscopy of Col1 fibers in the breast pathology work-flow, it would be feasible to image the SHG Col1 fiber signatures using paraffin blocks generated from excised tumors of patients as was done in Figure 3 or from biopsies as shown in Figure 5. As SHG microscopy is non-destructive, the unaltered paraffin blocks can be returned to the pathology archive following SHG microscopic investigation. Another major advantage of SHG microscopy is that it can be performed through an ultra-compact fiber-optic endomicroscope [40-45], which can be integrated with a 14-gauge breast biopsy needle. Such “through-needle” SHG endomicroscopy may in the future allow for SHG Col1 imaging to be performed during the initial diagnostic mammography-guided breast biopsy in the clinic. We have also demonstrated the feasibility of using automated software to analyze Col1 fibers, and obtain robust quantitative results that avoid human subjectivity and error. Our software has the potential to provide real-time results during fiber-optic endomicroscopy scanning.

Col1 fibers are the target of recently developed stromal depletion therapies to treat desmoplastic tumors [46]. Stromal depletion therapies are currently going into clinical trials in pancreatic cancer [46]. Imaging biomarkers that are able to assess the response to such therapies in patients will be important. The SHG-detected Col1 fiber signature may provide such a monitoring tool for stromal depletion therapies in the future, and this may be realized either by non-destructive SHG microscopy during the pathology work-flow using FFPE blocks, or by using SHG endomicroscopic imaging of Col1 fibers in patients. Col1 fibers also play an important role in drug delivery across the ECM of tumors, for which SHG imaging can serve as an assessment tool [18]. Tumor delivery of nanotherapeutics may in fact be improved by

strategies aimed at reducing the Col1 fiber matrix, as recently demonstrated with a Col1 synthesis inhibitor in desmoplastic models of human breast, pancreatic, and skin tumors using SHG microscopy [47].

## **Conclusions**

In summary, the results obtained here have identified a potential biomarker that may be useful in the assessment and staging of breast cancer, and confirmed the importance of Col1 fibers in the metastatic process. Larger scale studies using breast and other cancer tissues are necessary to validate the sensitivity and specificity of Col1 fibers detected with SHG microscopy to predict the presence of cancer cells in lymph nodes. Such studies can lead to the development of an imaging biomarker to evaluate lymph node metastasis at the time of presentation, and may result in the formulation of novel Col1 fiber-depletion strategies to reduce metastatic spread. Detection and quantification of Col1 fibers can easily be implemented in clinical pathological laboratory routines to provide additional valuable information for potentially predicting lymph node involvement in breast cancer. Automated software can be used to quantify the Col1 fiber distribution to give objective results, with the potential to perform real-time quantification during endomicroscopy.

## **Declaration of Competing Interests**

The author(s) declare that they have no competing interests.

**Authors' contributions**

SMK carried out all SHG imaging experiments, wrote the code of our in-house fiber analysis software, and performed all analyses with this in-house software. MS conceived of the in-house fiber analysis software, and supervised its testing. SS, LKJ, PA, and DL participated in the conception, design, and coordination of the study. ZMB and KG conceived of, designed, and coordinated the study. KG drafted the manuscript. All authors read, edited, and approved the final manuscript.

**Acknowledgements and Funding**

The authors thank Dr. Scot Kuo for expert technical support with the microscopy studies on the Zeiss 710 NLO Meta confocal microscope equipped for multiphoton microscopy, Dr. Xingde Li and Dr. Antonio Wolff for helpful discussions throughout this project, and Tiffany R. Greenwood for laboratory support.

This work was supported by the National Institutes of Health grants P50 CA103175 and P30 CA006973.



## References

1. Bergamaschi, A., E. Tagliabue, T. Sorlie, B. Naume, T. Triulzi, R. Orlandi, H.G. Russnes, J.M. Nesland, R. Tammi, P. Auvinen, V.M. Kosma, S. Menard, and A.L. Borresen-Dale (2008). Extracellular matrix signature identifies breast cancer subgroups with different clinical outcome. *J Pathol.* 214(3): 357-67.
2. Sund, M. and R. Kalluri (2009). Tumor stroma derived biomarkers in cancer. *Cancer Metastasis Rev.* 28(1-2): 177-83.
3. Falzon, G., S. Pearson, and R. Murison (2008). Analysis of collagen fibre shape changes in breast cancer. *Phys Med Biol.* 53(23): 6641-52.
4. Hompland, T., A. Erikson, M. Lindgren, T. Lindmo, and C. de Lange Davies (2008). Second-harmonic generation in collagen as a potential cancer diagnostic parameter. *J Biomed Opt.* 13(5): 054050.
5. Provenzano, P.P., K.W. Eliceiri, J.M. Campbell, D.R. Inman, J.G. White, and P.J. Keely (2006). Collagen reorganization at the tumor-stromal interface facilitates local invasion. *BMC Med.* 4(1): 38.
6. Provenzano, P.P., D.R. Inman, K.W. Eliceiri, J.G. Knittel, L. Yan, C.T. Rueden, J.G. White, and P.J. Keely (2008). Collagen density promotes mammary tumor initiation and progression. *BMC Med.* 6: 11.
7. Conklin, M.W., J.C. Eickhoff, K.M. Riching, C.A. Pehlke, K.W. Eliceiri, P.P. Provenzano, A. Friedl, and P.J. Keely (2011). Aligned collagen is a prognostic signature for survival in human breast carcinoma. *Am J Pathol.* 178(3): 1221-32.
8. Gupta, G.P. and J. Massague (2006). Cancer metastasis: building a framework. *Cell.* 127(4): 679-95.

9. Lochter, A. and M.J. Bissell (1995). Involvement of extracellular matrix constituents in breast cancer. *Semin Cancer Biol.* 6(3): 165-73.
10. Pathak, A.P., D. Artemov, M. Neeman, and Z.M. Bhujwalla (2006). Lymph node metastasis in breast cancer xenografts is associated with increased regions of extravascular drain, lymphatic vessel area, and invasive phenotype. *Cancer Res.* 66(10): 5151-8.
11. Pathak, A.P., D. Artemov, B.D. Ward, D.G. Jackson, M. Neeman, and Z.M. Bhujwalla (2005). Characterizing extravascular fluid transport of macromolecules in the tumor interstitium by magnetic resonance imaging. *Cancer Res.* 65(4): 1425-32.
12. Alexandrakis, G., E.B. Brown, R.T. Tong, T.D. McKee, R.B. Campbell, Y. Boucher, and R.K. Jain (2004). Two-photon fluorescence correlation microscopy reveals the two-phase nature of transport in tumors. *Nat Med.* 10(2): 203-7.
13. Ingber, D.E. (2008). Can cancer be reversed by engineering the tumor microenvironment? *Semin Cancer Biol.* 18(5): 356-64.
14. Alowami, S., S. Troup, S. Al-Haddad, I. Kirkpatrick, and P.H. Watson (2003). Mammographic density is related to stroma and stromal proteoglycan expression. *Breast Cancer Res.* 5(5): R129-35.
15. Li, T., L. Sun, N. Miller, T. Nicklee, J. Woo, L. Hulse-Smith, M.S. Tsao, R. Khokha, L. Martin, and N. Boyd (2005). The association of measured breast tissue characteristics with mammographic density and other risk factors for breast cancer. *Cancer Epidemiol Biomarkers Prev.* 14(2): 343-9.

16. Boyd, N.F., G.S. Dite, J. Stone, A. Gunasekara, D.R. English, M.R. McCredie, G.G. Giles, D. Tritchler, A. Chiarelli, M.J. Yaffe, and J.L. Hopper (2002). Heritability of mammographic density, a risk factor for breast cancer. *N Engl J Med.* 347(12): 886-94.
17. McCormack, V.A. and I. dos Santos Silva (2006). Breast density and parenchymal patterns as markers of breast cancer risk: a meta-analysis. *Cancer Epidemiol Biomarkers Prev.* 15(6): 1159-69.
18. Brown, E., T. McKee, E. diTomaso, A. Pluen, B. Seed, Y. Boucher, and R.K. Jain (2003). Dynamic imaging of collagen and its modulation in tumors in vivo using second-harmonic generation. *Nat Med.* 9(6): 796-800.
19. Kakkad, S.M., M. Solaiyappan, B. O'Rourke, I. Stasinopoulos, E. Ackerstaff, V. Raman, Z.M. Bhujwalla, and K. Glunde (2010). Hypoxic Tumor Microenvironments Reduce Collagen I Fiber Density. *Neoplasia.* 12(8): 608-617.
20. Bayan, C., J.M. Levitt, E. Miller, D. Kaplan, and I. Georgakoudi (2009). Fully automated, quantitative, noninvasive assessment of collagen fiber content and organization in thick collagen gels. *Journal of Applied Physics.* 105(10): 102042-11.
21. Cicchi, R., D. Kapsokalyvas, V. De Giorgi, V. Maio, A. Van Wiechen, D. Massi, T. Lotti, and F.S. Pavone (2010). Scoring of collagen organization in healthy and diseased human dermis by multiphoton microscopy. *Journal of biophotonics.* 3(1-2): 34-43.
22. Hu, W., H. Li, C. Wang, S. Gou, and L. Fu (2012). Characterization of collagen fibers by means of texture analysis of second harmonic generation images using orientation-dependent gray level co-occurrence matrix method. *Journal of biomedical optics.* 17(2): 026007.

23. Desbiens, N.A. (2003). A novel use for the word "trend" in the clinical trial literature. *The American journal of the medical sciences*. 326(2): 61-5.
24. Haralick, R.M., K. Shanmugam, and I.H. Dinstein (1973). Textural Features for Image Classification. *Systems, Man and Cybernetics, IEEE Transactions on*. SMC-3(6): 610-621.
25. Haralick, R.M. and L.G. Shapiro, *Computer and robot vision* 1992: Addison-Wesley.
26. Singletary, S.E., C. Allred, P. Ashley, L.W. Bassett, D. Berry, K.I. Bland, P.I. Borgen, G. Clark, S.B. Edge, D.F. Hayes, L.L. Hughes, R.V. Hutter, M. Morrow, D.L. Page, A. Recht, R.L. Theriault, A. Thor, D.L. Weaver, H.S. Wieand, and F.L. Greene (2002). Revision of the American Joint Committee on Cancer staging system for breast cancer. *J Clin Oncol*. 20(17): 3628-36.
27. Lucci, A., L.M. McCall, P.D. Beitsch, P.W. Whitworth, D.S. Reintgen, P.W. Blumencranz, A.M. Leitch, S. Saha, K.K. Hunt, and A.E. Giuliano (2007). Surgical complications associated with sentinel lymph node dissection (SLND) plus axillary lymph node dissection compared with SLND alone in the American College of Surgeons Oncology Group Trial Z0011. *J Clin Oncol*. 25(24): 3657-63.
28. Wolf, K. and P. Friedl (2009). Mapping proteolytic cancer cell-extracellular matrix interfaces. *Clin Exp Metastasis*. 26(4): 289-98.
29. Mierke, C.T., B. Frey, M. Fellner, M. Herrmann, and B. Fabry (2011). Integrin alpha5beta1 facilitates cancer cell invasion through enhanced contractile forces. *J Cell Sci*. 124(Pt 3): 369-83.
30. Bando, H., H.A. Weich, S. Horiguchi, N. Funata, T. Ogawa, and M. Toi (2006). The association between vascular endothelial growth factor-C, its corresponding receptor,

- VEGFR-3, and prognosis in primary breast cancer: a study with 193 cases. *Oncol Rep.* 15(3): 653-9.
31. Hirakawa, S., S. Kodama, R. Kunstfeld, K. Kajiya, L.F. Brown, and M. Detmar (2005). VEGF-A induces tumor and sentinel lymph node lymphangiogenesis and promotes lymphatic metastasis. *J Exp Med.* 201(7): 1089-99.
  32. Jennbacken, K., C. Vallbo, W. Wang, and J.E. Damber (2005). Expression of vascular endothelial growth factor C (VEGF-C) and VEGF receptor-3 in human prostate cancer is associated with regional lymph node metastasis. *Prostate.* 65(2): 110-6.
  33. Alitalo, K., T. Tammela, and T.V. Petrova (2005). Lymphangiogenesis in development and human disease. *Nature.* 438(7070): 946-53.
  34. Grimaldi, A., A. Moriondo, L. Sciacca, M.L. Guidali, G. Tettamanti, and D. Negrini (2006). Functional arrangement of rat diaphragmatic initial lymphatic network. *Am J Physiol Heart Circ Physiol.* 291(2): H876-85.
  35. Ryan, T.J. (1989). Structure and function of lymphatics. *J Invest Dermatol.* 93(2 Suppl): 18S-24S.
  36. Swartz, M.A. (2001). The physiology of the lymphatic system. *Adv Drug Deliv Rev.* 50(1-2): 3-20.
  37. Campagnola, P.J. and L.M. Loew (2003). Second-harmonic imaging microscopy for visualizing biomolecular arrays in cells, tissues and organisms. *Nat Biotechnol.* 21(11): 1356-60.
  38. Zipfel, W.R., R.M. Williams, R. Christie, A.Y. Nikitin, B.T. Hyman, and W.W. Webb (2003). Live tissue intrinsic emission microscopy using multiphoton-excited native

- fluorescence and second harmonic generation. *Proc Natl Acad Sci U S A*. 100(12): 7075-80.
39. Cavalli, L.R. (2009). Molecular markers of breast axillary lymph node metastasis. *Expert Rev Mol Diagn*. 9(5): 441-54.
  40. Bao, H., A. Boussioutas, R. Jeremy, S. Russell, and M. Gu (2010). Second harmonic generation imaging via nonlinear endomicroscopy. *Opt Express*. 18(2): 1255-60.
  41. Liu, G., T. Xie, I.V. Tomov, J. Su, L. Yu, J. Zhang, B.J. Tromberg, and Z. Chen (2009). Rotational multiphoton endoscopy with a 1 microm fiber laser system. *Opt Lett*. 34(15): 2249-51.
  42. Myaing, M.T., D.J. MacDonald, and X.D. Li (2006). Fiber-optic scanning two-photon fluorescence endoscope. *Optics Letters*. 31(8): 1076-1078.
  43. Wu, Y.C. and X.D. Li, *Two-photon Fluorescence Endomicroscopy*, in *Advances in Lasers and Electro Optics*, Nelson Costa and Adolfo Cartaxo, Editors. 2010, InTech Publishing.
  44. Wu, Y.C., Y.X. Leng, J.F. Xi, and X.D. Li (2009). Scanning all-fiber-optic endomicroscopy system for 3D nonlinear optical imaging of biological tissues. *Optics Express*. 17(10): 7907-7915.
  45. Wu, Y., J. Xi, M.J. Cobb, and X. Li (2009). Scanning fiber-optic nonlinear endomicroscopy with miniature aspherical compound lens and multimode fiber collector. *Optics Letters*. 34(7): 953-5.
  46. Garber, K. (2010). Stromal depletion goes on trial in pancreatic cancer. *J Natl Cancer Inst*. 102(7): 448-50.

47. Diop-Frimpong, B., V.P. Chauhan, S. Krane, Y. Boucher, and R.K. Jain (2010). Losartan inhibits collagen I synthesis and improves the distribution and efficacy of nanotherapeutics in tumors. *Proc Natl Acad Sci U S A*. 108(7): 2909-14.





## Chapter 4

---

### Hypoxic tumor environments exhibit disrupted collagen I fibers and low macromolecular transport

Published in: **PLoS One. 2013 Dec 12;8(12)**

Hypoxic tumor environments exhibit disrupted collagen I fibers and low macromolecular transport.

**Samata M. Kakkad**, Marie-France Penet, Alireza Akhbardeh, Arvind P. Pathak, Meiyappan Solaiyappan, Venu Raman, Dieter Leibfritz, Kristine Glunde, and Zaver M. Bhujwalla

**Abbreviations footnote**

Albumin-GdDTPA, albumin-Gd-diethylenetriaminepentaacetate

Coll, collagen 1

ECM, extracellular matrix

FOV, field of view

FCM, fuzzy c-means

HIF, hypoxia inducible factor

HRE, hypoxia response element

K-S, Kolmogorov-Smirnov

MMCA, macromolecular contrast agent

MRI, magnetic resonance imaging

PS, permeability surface area product

RFP, red fluorescent protein

ROI, region of interest

SCID, severe combined immunodeficient

SHG, second harmonic generation

SD, standard deviation

VV, vascular volume

**Abstract**

Hypoxic tumor microenvironments result in an aggressive phenotype and resistance to therapy that leads to tumor progression, recurrence, and metastasis. While poor vascularization and the resultant inadequate drug delivery are known to contribute to drug resistance, the effect of hypoxia on molecular transport through the interstitium and the role of the extracellular matrix (ECM) in mediating this transport are unexplored. The dense mesh of fibers present in the ECM can especially influence the movement of macromolecules. Collagen 1 (Col1) fibers form a key component of the ECM in breast cancers. Here we characterized the influence of hypoxia on macromolecular transport in tumors, and the role of Col1 fibers in mediating this transport using an MDA-MB-231 breast cancer xenograft model engineered to express red fluorescent protein under hypoxia. Magnetic resonance imaging of macromolecular transport was combined with second harmonic generation microscopy of Col1 fibers. Hypoxic tumor regions displayed significantly decreased Col1 fiber density and volume, as well as significantly lower macromolecular draining and pooling rates, than normoxic regions. Regions adjacent to severely hypoxic areas revealed higher deposition of Col1 fibers and increased macromolecular transport. These data suggest that Col1 fibers may facilitate macromolecular transport in tumors and their reduction in hypoxic regions may reduce this transport. Decreased macromolecular transport in hypoxic regions may also contribute to poor drug delivery and tumor recurrence in hypoxic regions. High Col1 fiber density observed around hypoxic regions may facilitate the escape of aggressive cancer cells from hypoxic regions.

## Introduction

Tumors display abnormal physiological environments such as hypoxia, which primarily arise from their abnormal and chaotic vasculature [1]. Hypoxia is associated with increased resistance to radiation and chemotherapy, and with a more aggressive phenotype [1]. The discovery of the hypoxia inducible factor (HIF), and the identification of hypoxia response elements (HREs) as transcriptional controls in multiple genes [2], is continuing to unravel the critical role of hypoxia in influencing cancer progression and metastasis. The molecular mechanisms underlying the cascade of changes induced by hypoxia and the HIF-axis have attracted significant attention [2], but the functional impact of hypoxia on the tumor extracellular matrix (ECM) and on the transport of macromolecules in the tumor interstitium is relatively unexplored. Our purpose here was to investigate the role of hypoxia in altering the ECM, particularly the Col1 fiber distribution, and its effect on macromolecular transport. To study the relationship between hypoxia, macromolecular transport, and Col1 fiber distribution, we combined dynamic magnetic resonance imaging (MRI) of the macromolecular contrast agent (MMCA) albumin-GdDTPA, to detect interstitial macromolecular transport, with second harmonic generation (SHG) microscopy to measure Col1 fibers morphology and distribution. SHG is a nonlinear optical process that requires a molecular environment without a center of symmetry, such as an interfacial region, to produce a signal that can be used to image endogenous structural proteins such as Col1 [3]. These studies were performed in MDA-MB-231 human breast cancer xenografts genetically engineered to express tdTomato red fluorescent protein (RFP) under control of HRE [4].

As an abundant stromal component, Col1 fibers form a major part of the breast tumor ECM [5-8]. Malignant breast cancers are characterized by significantly higher Col1 fiber density and altered Col1 fiber architecture [8]. High mammary Col1 density was shown to cause mammary tumor initiation, progression, and metastasis [8]. We have previously shown that hypoxic regions in breast and prostate tumor xenografts contain significantly lower Col1 fiber density and volume compared to normoxic tumor regions [9]. Hypoxia stimulates the gene expression of a cluster of hydroxylases necessary for Col1 fiber formation [10]. Hypoxic environments in tumors may lead to abnormal collagen deposition either by cancer cells or fibroblasts within the tumor stroma [8,11]. In normal tissue, Col1 fibers direct interstitial fluid into lymphatic channels [12]. In tumors, these fibers may not be structured for efficient flow of fluid, especially in hypoxic areas [9]. Here, by careful co-registration of *in vivo* MRI to *ex vivo* optical images, we related macromolecular transport to Col1 fibers morphology and hypoxia. Macromolecules that extravasate from the vasculature into the tumor interstitium, are transported through the ECM either by diffusion or convection [13-15]. To understand drug delivery through the tumor ECM, it is important to understand the role of both, Col1 fibers and hypoxia in this transport.

The movement of macromolecules through the ECM can also provide insight into the movement of metastatic cells through the ECM. Our data suggest that collagen fibers mediate macromolecular transport that is reduced in hypoxic low Col1 fiber containing regions. Around these severely hypoxic regions, a dense Col1 fiber mesh is observed that aligns with increased macromolecular transport. These results have significant implications for the delivery of macromolecular therapeutic agents as they uncover a new aspect of hypoxic environments in limiting macromolecular transport. The sparser fibers within severely hypoxic regions and the

previously observed close correlation between dense collagen fibers and metastasis [16] suggest that the stimulus for invasion may occur from hypoxic environments with the denser collagen fibers around these regions providing avenues of escape and dissemination in the metastatic cascade.

## **Materials and Methods**

### *Ethics statement*

All experimental animal protocols were approved by the Institutional Animal Care and Use Committee of the Johns Hopkins University School of Medicine under the animal protocol number MO11M122 and under the Animal Welfare Assurance Number A3272-01.

### *Tumor model and inoculation*

The triple-negative metastatic human breast cancer cell line MDA-MB-231 [17] was obtained from the American Type Culture Collection (ATCC, Rockville, MD). To generate MDA-MB-231 cells that express red fluorescent protein (RFP) under hypoxic conditions, MDA-MB-231 cells were stably transfected with a construct containing five copies of the HRE of the human VEGF-A gene ligated to the cDNA of the tdTomato RFP, which produced MDA-MB-231-5HRE-TdTomato cells as previously described and validated [4,18]. Two million MDA-MB-231-5HRE-TdTomato cells were orthotopically inoculated in the right upper thoracic mammary fat pad of anesthetized female severe combined immunodeficient (SCID) mice.

MDA-MB-231-5HRE-TdTomato tumor xenografts reached their final experimental size of approximately 400-500 mm<sup>3</sup> within 8 weeks and the studies were performed with 10 mice.

### *MRI acquisition*

Mice were imaged 8 weeks post inoculation, once tumor volumes were approximately 400-500 mm<sup>3</sup>. The mouse was anesthetized for MRI, and a home-built catheter was inserted in the tail vein to deliver the MMCA albumin-GdDTPA. MRI was performed on a 4.7T Bruker spectrometer using a home built solenoid coil placed around the tumor. The respiration rate was monitored and an isoflurane mask used to maintain stable anesthesia during the 123 min of MRI scan time. The MRI acquisition was performed as previously described [19]. Briefly, multi-slice relaxation rates (T1-1) were acquired using a saturation recovery technique with fast-T1 SNAPSHOT FLASH imaging (flip angle = 10 degrees, echo time = 2 ms). Images of the central 4 slices (slice thickness of 1 mm) of the tumor were acquired (128 x 128 matrix, 16 mm field of view, number of average = 8) for three relaxation delays (100, 500 and 1000 ms). A multislice map of completely relaxed magnetization (M0 map) was also acquired with a recovery time of seven seconds. The in-plane resolution of the MR images was 125  $\mu\text{m}$  x 125  $\mu\text{m}$ . Interstitial transport parameters were measured from quantitative T1 maps obtained before and following intravenous administration of the MMCA albumin-GdDTPA (500 mg/kg dose). Images were acquired in two “phases” corresponding to the biphasic kinetics of the MMCA [19]. The “early phase” acquisition images included a pre-contrast image, and a 3 minute post-contrast image that was repeated every 5 minutes over the initial 30 minutes to characterize the tumor vascular volume (VV) and permeability surface area product (PS). Since drainage of macromolecules in

and around tumors either by convection or by the lymphatics is a slow event, the second block of MR data was acquired up to 123 minutes post-contrast and was used to characterize the interstitial transport parameters through the ECM. Transport parameters calculated included number of draining and pooling voxels, draining and pooling rates, and exudate volumes derived as previously described [19] and briefly described in the Quantification section). At the end of the MRI acquisition, blood T1 was determined from 20 microliters drawn from the tail vein. The experimental workflow is outlined in Figure 1.

#### *Fluorescence and multiphoton microscopy*

Following the MRI acquisition, mice were euthanized and the tumors were excised. The orientation of the tumor in the MRI scanner bore was registered using spatial markers, and the tumor sliced into 1 mm thick sections. Optical imaging of the fresh tissue slices corresponding to the MR-imaged slices was performed to detect hypoxic and normoxic regions. First an overview of the entire tumor slice was acquired at 1× magnification using a Nikon inverted microscope equipped with a Nikon Coolpix digital camera (Nikon Instruments, Inc., Melville, NY, Figure 1, Image acquisition block – Ex-vivo imaging). Images of all four slices were acquired in the bright field for tissue architecture and in the red fluorescence field for detection of hypoxic regions. Optical images acquired with the 1× objective, were used to map the MRI data to hypoxic and normoxic regions within the corresponding slices, and identify fields of view (FOV) to image Col1 fibers at higher magnification. We used multiphoton microscopy to detect the SHG signal from the Col1 fibers in these fresh tissue slices. SHG imaging was performed as previously described [9, 16]. Briefly, we used a 25×/0.8 LD LCI PlanApo multi-immersion lens



on a Zeiss 710 LSM NLO Meta multiphoton microscopy system (Carl Zeiss MicroImaging, Inc, Thornwood, NY) equipped with a 680-1080 nm tunable Coherent Chameleon Vision II laser (Coherent, Inc, Santa Clara, CA) with automated pre-compensation and fast scanning at 40 nm/s. 3-dimensional (3D) image stacks were acquired from various fields of view (FOVs) in the hypoxic and normoxic regions. Hypoxic FOVs were selected to contain more than 80% of red fluorescing cells and were therefore severely hypoxic. Normoxic FOVs contained less than 1% of red fluorescing cells. Coll fibers were illuminated with incident laser light of 880 nm and detected at 410-470 nm. The fluorescence from TdTomato red was excited at a wavelength of 543 nm, and detected at 570-620 nm [9].

#### *Quantitative image analysis*

Macromolecular transport in tumors was quantified from the dynamic MRI images based on biphasic kinetics of the MMCA as previously described [19]. Vascular VV and PS were calculated from the first 30 minutes during the 'early phase'. 'Late phase' images acquired up to 123 minutes post contrast injection gave macromolecular transport parameters that included draining rate, draining volume, pooling rate, and pooling volume. During the 'late phase' a draining voxel was defined as a voxel from which the contrast agent at a rate lower than the PS, and a pooling voxel was one in which the contrast agent concentration increased at a rate higher than the PS. After identifying the draining and pooling voxels, the rates and exudate volumes were calculated. All quantification analysis was done in a home-built program written in IDL (ITT Exelis Visual Information Solutions, VA USA) and AFNI (NIH software).

The structural information of the tumor microenvironment was obtained by quantifying the Col1 fiber distribution acquired with SHG microscopy. Col1 fiber distribution analysis was performed as previously described [9]. Briefly, the inter-fiber distance and percent fiber volume present in hypoxic and normoxic FOVs were quantified. The quantification of the Col1 fiber distance distribution and fiber volume was performed using a customized program written in Matlab (MATLAB 7.4.0, The MathWorks, Natick, MA). Regions of interest (ROIs) containing more than 80 % of red fluorescing cells, considered severely hypoxic, and regions with less than 1 % of red fluorescing cells, considered normoxic, were analyzed [9]. A two-sided paired t-test ( $\alpha = 0.05$ ) was used to detect significant differences in inter-fiber distances and percent fiber volumes between these severely hypoxic and normoxic ROIs using Microsoft Office Excel 2010 (Microsoft, Redmond, WA). P-values of  $< 0.05$  were considered to be significant.

To combine functional and structural information, MRI and  $1\times$  optical images were co-registered (Figure 1, Image processing and quantification block) to calculate transport parameters in hypoxic and normoxic ROIs. To account for tissue deformation and differences in spatial information we used a mutual information – based registration approach and calculated Dice similarity statistics to quantify the quality of the co-registration.

To preserve the orientation of the tumor during the *in vivo* MRI acquisition, we used 5% agarose gel to cover the entire tumor, and made asymmetrical cuts in the surrounding agarose gel before acquiring the MRI images. Since agarose gel contains water, it results in a uniform signal around the tumor in the M0 map (Figure 1, Image Acquisition block). The asymmetrical markings were visible in the MRI images and helped mark the orientation of the tumor.

Following MRI, the tumor was excised and sliced with the tumor orientation maintained as it was in the MRI scanner. For each modality we combined the various images acquired, extracted features, and used the mutual information approach for co-registration between modalities (Figure 1, Image Processing block). For the MRI images we used the R1 maps acquired over 26 time points to identify cluster features using the fuzzy c-means (FCM) [20,21] clustering technique (Figure 1, Image Processing block). For the optical images, we fused the bright field and fluorescent images by wavelet based image fusion [22], and extracted features for the optical images using FCM. Extracted features from the optical images were then registered to the extracted features from the MR image using affine transformation [23]. Rigid-body registration was used to avoid any feature distortion. Since the bright field image and fluorescence field image are intrinsically registered to the fused image, the same transformation matrix was applied to register them to the MR images. Dice similarity index [24] was calculated to assess the registration error. Dice similarity indices ranged from 0 to 1, where 0 indicates no overlap and 1 indicates complete overlap [24]. For multimodality co-registration of *in vivo* MRI and *ex vivo* optical data, a Dice similarity index  $> 0.85$  was considered as good overlap. Once the images were co-registered, the hypoxic regions were drawn out on the co-registered fluorescent images to calculate the vascular parameters of VV and PS in the hypoxic and normoxic regions. Similarly, the macromolecular transport parameters of draining rate and volume, and pooling rate and volume were calculated for hypoxic and normoxic regions (Figure 1, Image processing and quantification block – Quantification). The co-registration and co-localization analysis was performed in MATLAB 7.4.0 (The MathWorks, Natick, MA). A two tailed t-test was performed using Microsoft Office Excel 2010. P-values of  $< 0.05$  were considered to be significant (N = 10).

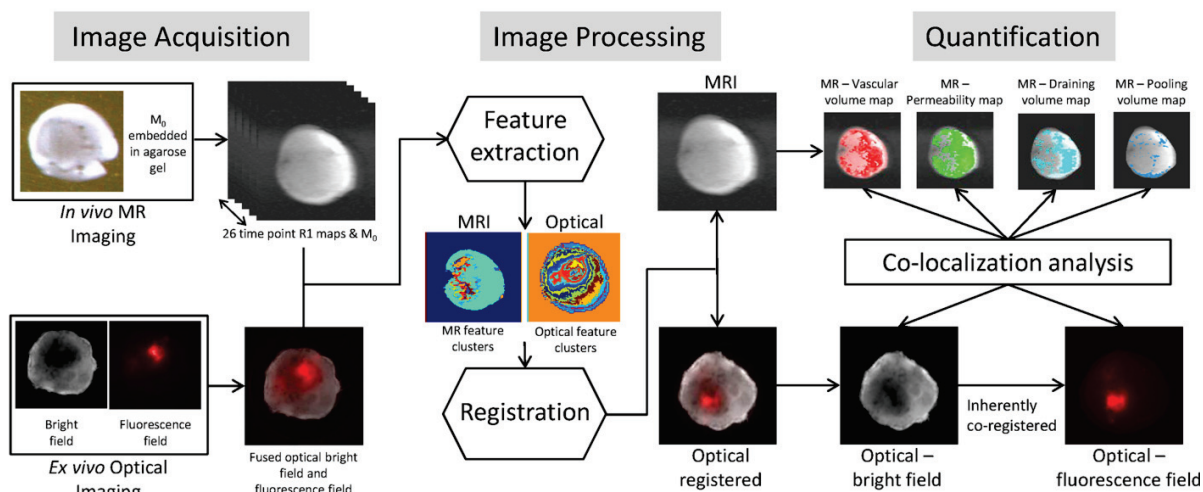


**Figure 1:** Workflow of the experimental design. The workflow consisted of three distinct parts: image acquisition, image processing and image quantification. For the image acquisition part, we performed *in vivo* MRI to extract functional information of vasculature and macromolecular transport within the tumor ECM. Following MRI, the tumor was excised and *ex vivo* optical imaging performed to extract the distribution of hypoxic regions and Col1 fibers. In image processing, MRI and optical images were co-registered following which vascular and transport parameters in hypoxic and normoxic regions were computed. Col1 fiber distributions in these regions were quantified to give fiber volume and inter-fiber distances. For image quantification, the quantitative data were analyzed and comparisons performed between hypoxic and normoxic regions.

## Results

Hypoxic regions were identified by tdTomato red fluorescence in the optical images ( $N = 10$ , Figure 2a). Using SHG microscopy, we observed significantly fewer and sparsely distributed Col1 fibers in severely hypoxic regions as compared to normoxic regions. A 3D visualization of the Col1 fiber in these hypoxic regions (Figure 2b) and normoxic regions (Figure 2c) revealed that the regions in the sparsely distributed Col1 fibers were filled with hypoxic cells. Quantitative analysis of the Col1 fibers showed that the percentage of Col1 fiber volume in severely hypoxic regions was significantly lower than that in the normoxic regions ( $p\text{-value} = 0.000106$ ,  $N = 10$ , Figure 2d). Similarly, the inter fiber distance in these hypoxic regions was

significantly greater than that in normoxic regions ( $p$ -value = 0.000121,  $N = 10$ , Figure 2e), indicating more sparsely distributed Col1 fibers in the hypoxic regions as compared to the normoxic regions.

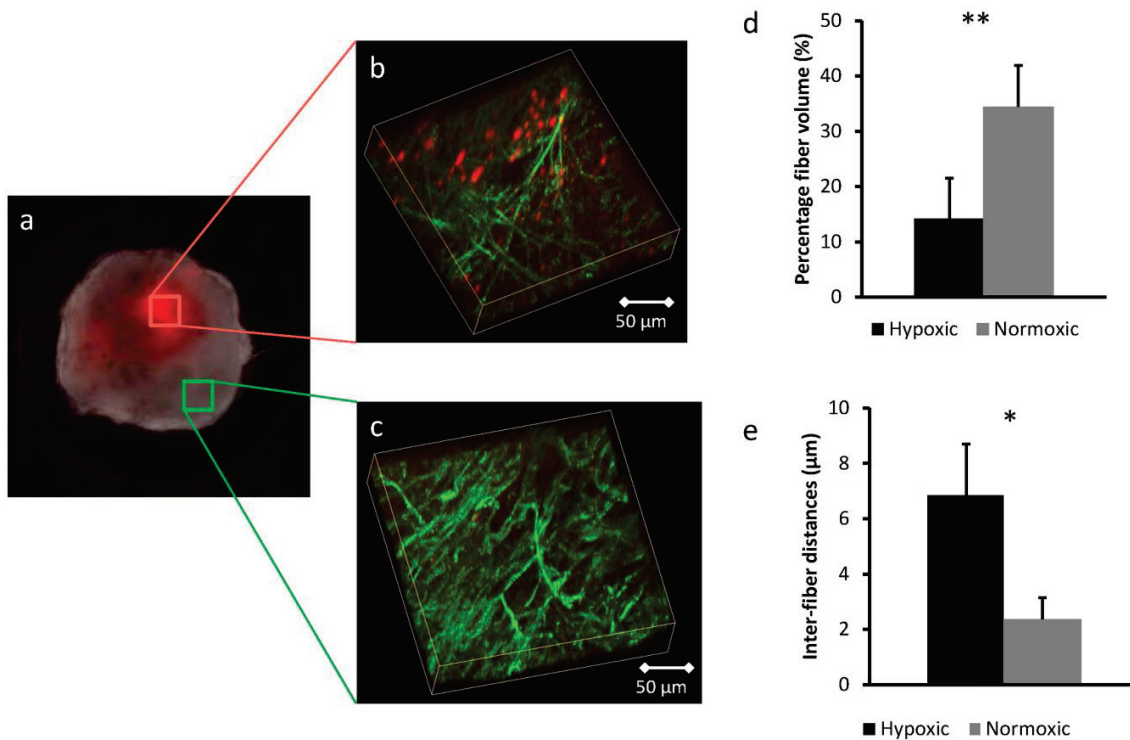


**Figure 2:** Optical imaging and quantification of fiber volume and fiber distribution. (a) *Ex vivo* 1× bright field and fluorescence image overlaid showing the locations of hypoxic ROIs on the tumor section. 3D visualization of (b) hypoxic and (c) normoxic FOVs; hypoxic regions are displayed in red and Col1 fibers in green. The FOV image size was 334.91 x 334.91 x 60 μm<sup>3</sup> with a voxel size of 0.66 x 0.66 x 1 μm<sup>3</sup>. (d) Hypoxic FOVs showed a significantly lower fiber volume as compared to normoxic FOVs (\*\* $p$ -value = 0.000106,  $N = 10$ ). (e) Hypoxic FOVs have a significantly larger inter-fiber distance as compared to normoxic FOVs (\* $p$ -value = 0.000121,  $N = 10$ ).

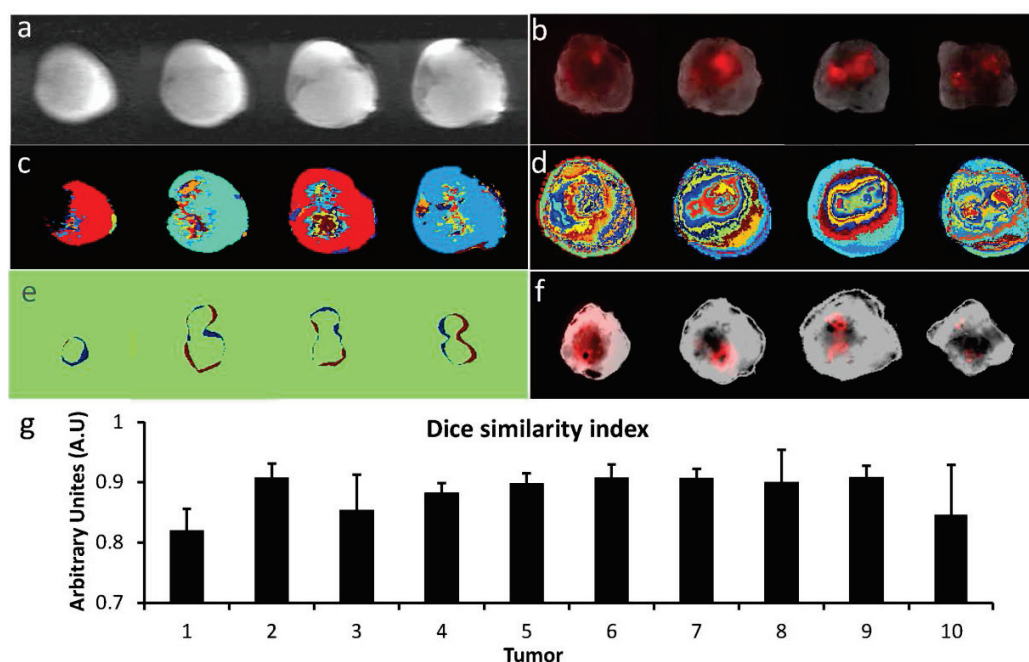
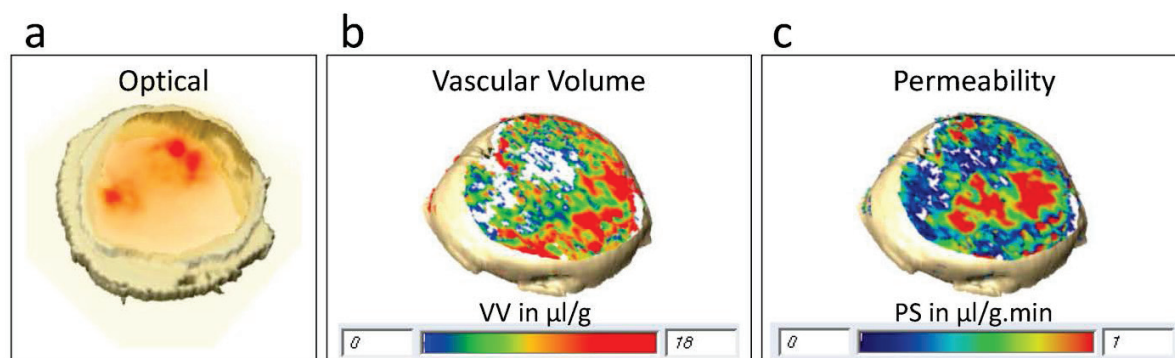


**Figure 3:** Co-registration results. (a) MR anatomical  $M_0$  images of the central four slices of the tumor as reference images ( $FOV = 16 \times 16 \times 4 \text{ mm}^3$ ). (b) Display of the optical bright field image overlaid with the fluorescence field image. Features extracted from (c) MR images and (d) optical images, respectively. (e) Display of the extracted features from the MR images overlaid with the optical images after co-registration. (f) Registered optical bright field images overlaid with the fluorescence field images. (g) The co-registration error represented by the Dice similarity index for all tumors ( $N = 10$ ) in this study.

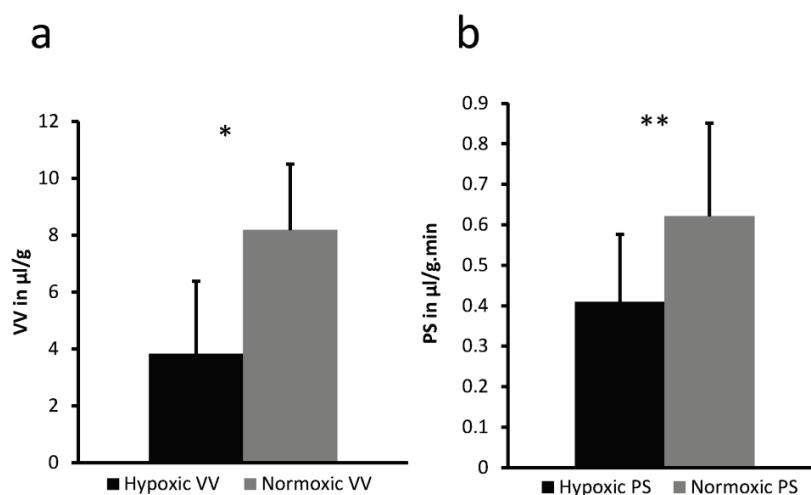
To understand how these differences in the Coll fibers functionally affect molecular transport through the tumor ECM, the optical images were co-registered to the corresponding MR sections. Figure 3a shows the  $M_0$  map of the central of four slices through the tumor; Figure 3b shows the corresponding fluorescence images overlaid on the bright field optical images before co-registration. Figures 3c and 3d show the feature clustering from the MR images and the fused optical images (bright and fluorescence field images), respectively. These extracted features were used to co-register the optical images to the corresponding MR sections. Figure 3e shows the extracted optical imaging features that were registered to the extracted MRI features. The difference in color shows the error of registration mismatch between the MR and optical images. Figure 3f shows the co-registered optical (fluorescence image overlaid with the

bright field images) and MR images. The registration error between the MR and optical images calculated as the Dice similarity index is shown in Figure 3g for all tumors. The indices were greater than 0.85, indicating successful co-registration between the MRI and optical images.

From the co-registered optical and MR imaging data, we observed that red fluorescing hypoxic regions co-localized with regions where the VV was low, as shown by 3D reconstruction of all four slices of the optical and VV data of a representative tumor in Figures 4a and 4b respectively. We also observed lower PS in the hypoxic regions as compared to normoxic regions, as seen in Figure 4c. We quantified these parameters and found that VV in hypoxic regions was significantly lower than that in normoxic regions ( $p$ -value = 0.000374,  $N = 10$ , Figure 5a). Similarly, PS values in the hypoxic regions were significantly lower than those in normoxic regions ( $p$ -value = 0.000215,  $N = 10$ , Figure 5b).



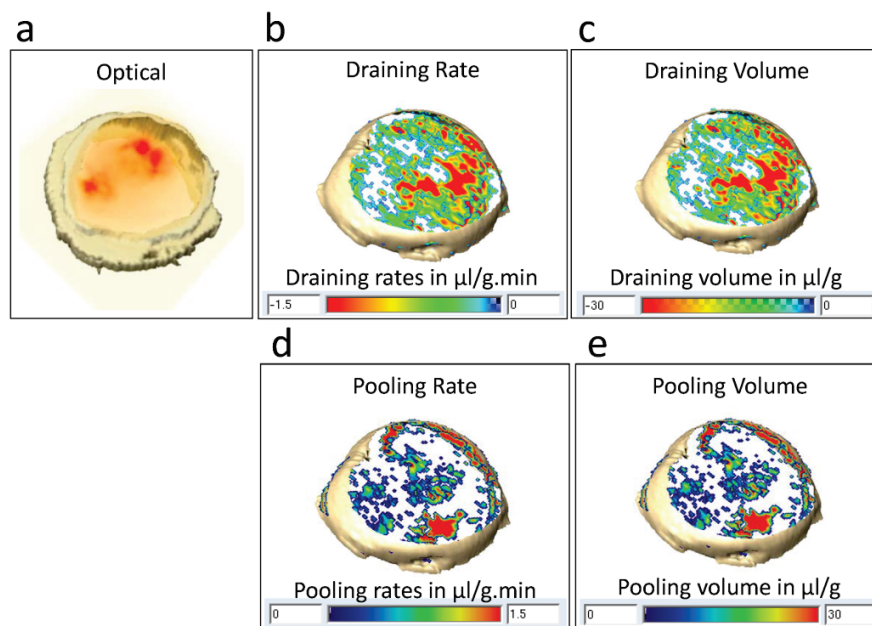
**Figure 4:** Representative 3D reconstructed view of vascular parameters. 3D reconstruction of (a) optical image with hypoxic regions displayed in red within the tumor, (b) corresponding display of VV and (c) PS in a breast cancer xenograft.



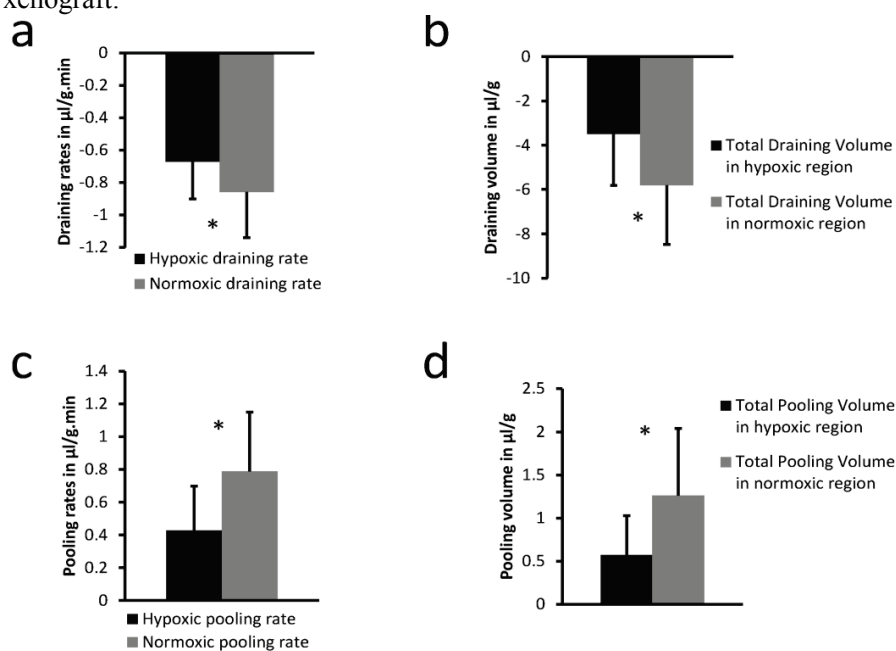
**Figure 5:** Quantification results of vascular parameters. Quantitative comparison of (a) VV and (b) PS for hypoxic and normoxic breast tumor regions. Columns: Mean  $\pm$  standard deviation (SD). We observed significantly lower VV (\**p-value* = 0.000374, N = 10) and PS (\*\**p-value* = 0.000215, N = 10) in hypoxic regions compared to normoxic regions. Columns: Mean  $\pm$  SD.

Representative 3D reconstructed optical images with the hypoxic regions displayed in red are shown in Figure 6a, along with the corresponding 3D molecular transport distributions of draining rate (Figure 6b), draining volume (Figure 6c), pooling rate (Figure 6d), and pooling volume (Figure 6e). We observed that the draining (or efflux) rates in hypoxic regions were significantly lower than those in normoxic regions (*p-value* = 0.003221, N = 10, Figure 7a), and the draining volume was significantly lower in hypoxic regions as compared to that in normoxic regions (*p-value* = 0.001887, N = 10, Figure 7b). Draining values are negative since the MMCA is leaving the voxel. The pooling (or influx) rate in hypoxic regions was significantly lower as compared to that in normoxic regions (*p-value* = 0.000109, N = 10, Figure 7c), and the pooling volume was significantly lower in hypoxic regions as compared to that in normoxic regions (*p-value* = 0.024693, N = 10, Figure 7d).





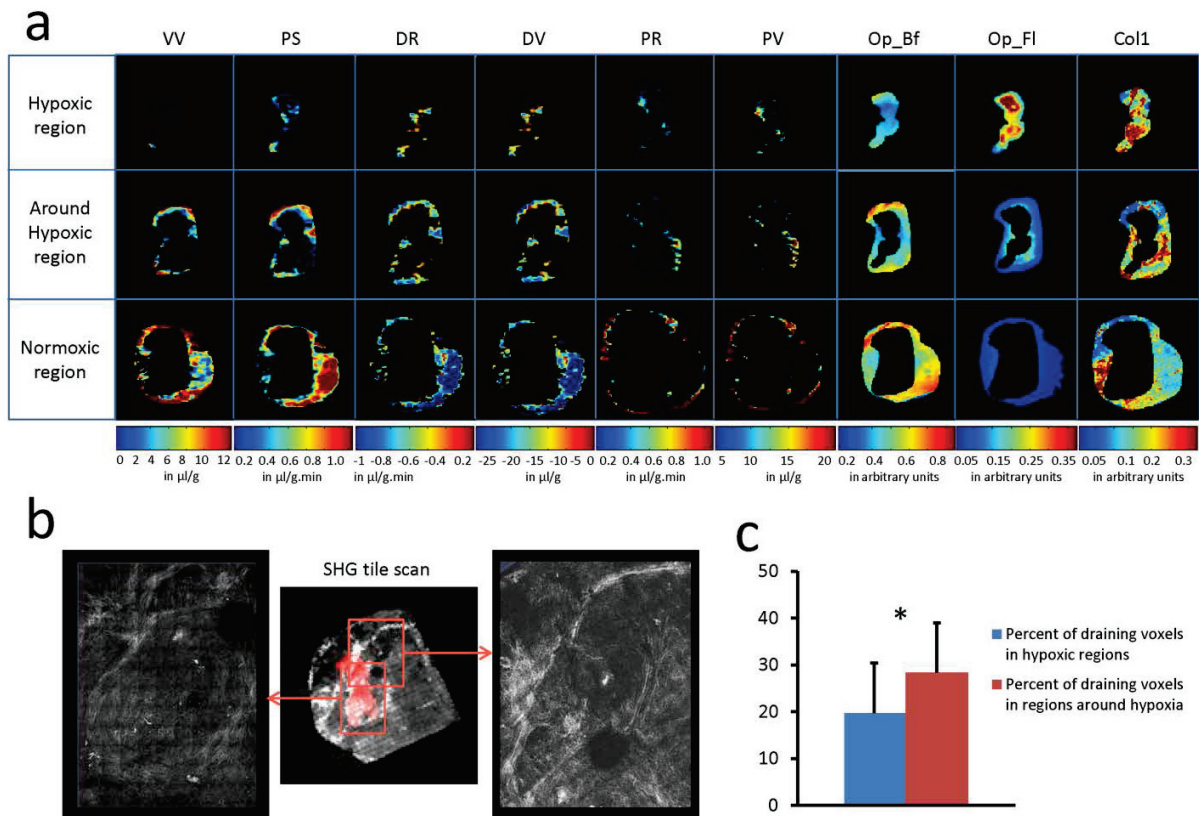
**Figure 6:** Representative 3D reconstructed view of transport parameters. 3D re-construction of (a) the optical image as in 4a with hypoxic regions displayed in red within the tumor, (b) corresponding display of draining rate, (c) draining volume distribution, (d) pooling rate and (e) pooling volume distribution in a breast cancer xenograft.



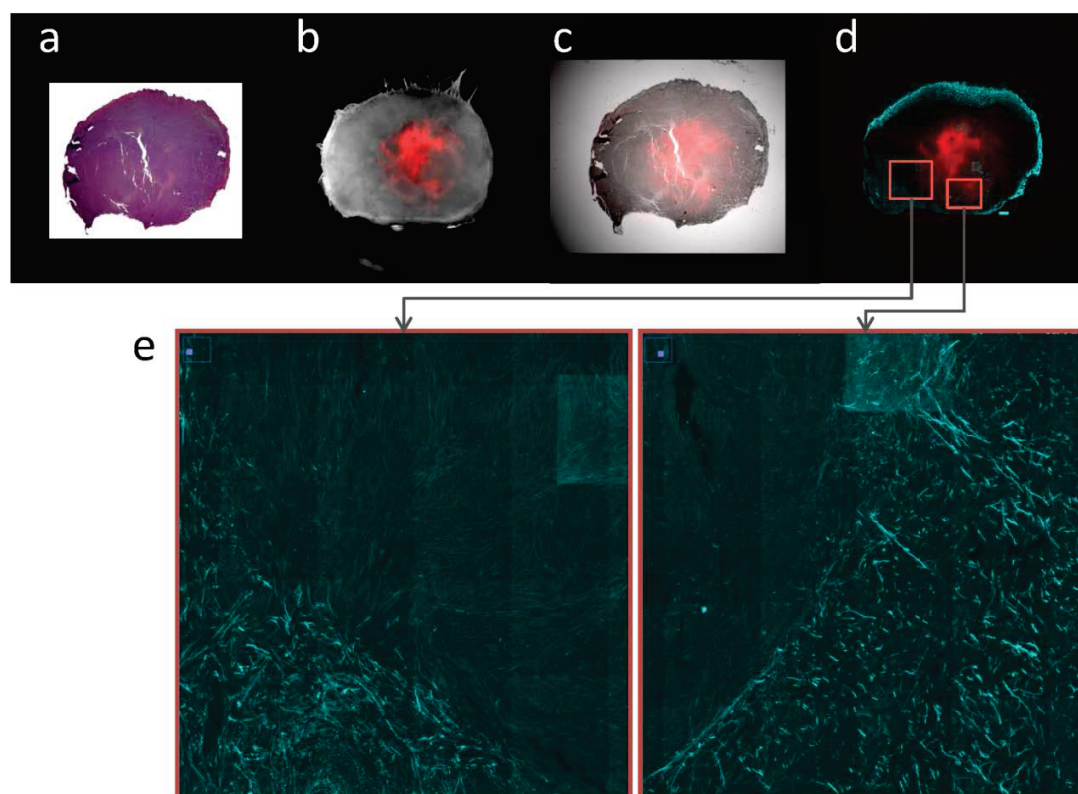
**Figure 7:** Quantification of transport parameters. Quantitative comparison of (a) draining rates, (b) draining volumes, (c) pooling rates and (d) pooling volumes. We observed significantly lower draining rates ( $p$ -value = 0.003221,  $N = 10$ ) and draining volumes ( $p$ -value = 0.001887,  $N = 10$ ) in hypoxic regions as compared to normoxic regions. We observed significantly lower pooling rates ( $p$ -value = 0.000109,  $N = 10$ ) and pooling volumes ( $p$ -value = 0.024693,  $N = 10$ ) in hypoxic regions as compared to normoxic regions. Columns: Mean  $\pm$  SD.

Figure 8 shows the analysis of different tumor regions. In Figure 8a, the 2D spatial distribution of VV and PS, draining rate (DR), draining volume (DV), pooling rate (PR), pooling volume (PV), optical bright field (OP\_Bf), optical fluorescence field (OP\_Fl) and fibers are shown for a representative tumor section in hypoxic (top panel),  $\sim 100 \mu\text{m}$  around hypoxic (middle panel), and normoxic (bottom panel) regions. Figure 8b displays a representative SHG tile image scan with an enlarged inserts showing the Coll fiber patterns adjacent to hypoxic regions. This circular pattern around hypoxic regions was observed in most tumors. As shown in Figure 8c, MMCA movement in regions adjacent to strongly hypoxic regions increased significantly ( $p\text{-value} = 0.014328$ ) as compared to hypoxic regions.

Since chronic or acute hypoxia will ultimately result in cell death and necrosis if the tissue is not rescued by revascularization, it was important to establish that the differences in macromolecular transport between hypoxic and normoxic observed were not primarily due to severely hypoxic red fluorescing regions consisting of largely dying regions. As shown in Figures 9a-c, red fluorescing regions contained viable cells. Trends in macromolecular transport were similar irrespective of the extent of necrosis in these regions. The presence of a ring of Coll fibers around these red fluorescing regions (Figure 9d) is again confirmed in the magnified high-resolution tiled images shown in Figure 9e.



**Figure 8:** Regional Analysis. (a) Displays of the distribution of vascular parameters (VV, PS), transport parameters (DR – draining rate, DV – draining volume, PR – pooling rate, PV – pooling volume) and optical imaging parameters (OP\_Bf – optical bright field, OP\_Fl – optical fluorescence field, Col1 – Col1 fibers) in hypoxic regions (top panel),  $\sim 100 \mu\text{m}$  around hypoxic regions (middle panel), and in normoxic regions (bottom panel) of a representative tumor section from a breast cancer xenograft. (b) Tile scan of SHG microscopy of Col1 fibers of the same section, showing Col1 fiber patterns in the magnified inserts. (c) Quantifications of draining voxels in percent showing a significant increase (\*  $p$ -value = 0.014329,  $N = 10$ ) in percent draining area in areas surrounding hypoxic regions.



**Figure 9:** Histological analysis. (a) Hematoxylin and eosin (H&E) stained 5  $\mu\text{m}$  thick section from a representative tumor, (b) corresponding overlaid bright field and fluorescence field images showing the tdTomato red fluorescence hypoxic regions, (c) overlay of H&E section with fluorescence field image, (d) overlay of corresponding SHG tile scan of Col1 fibers with fluorescence field image, and (e) magnified inserts from (d) displaying the Col1 fibers encircling the hypoxic regions.

## Discussion

Here, for the first time, we combined MRI with SHG microscopy to relate differences in collagen fibers between hypoxic and normoxic tumor regions to macromolecular fluid transport. Our purpose was to understand the role of hypoxia in modifying macromolecular fluid transport, using MRI, and collagen fiber distribution, using SHG microscopy. Higher MMCA draining voxels were observed in normoxic regions which also exhibited a dense mesh of collagen fibers. In contrast there were few draining voxels in hypoxic regions which also exhibited fewer and

structurally altered collagen fibers. These results suggest that collagen fibers may facilitate MMCA transport in tumors, for the size ( $\sim 90$  kDa) and charge of the agent used here, and their absence in hypoxic regions may reduce this transport.

For these studies, we developed an imaging pipeline to extract functional and structural information from the tumor microenvironment and quantify this information. From the MRI results, we observed a heterogeneous distribution of VV, PS, draining rate and volume, and pooling rate and volume, which were consistent with previous observations [19]. Also consistent with previous observations, we observed that the Col1 fiber distribution was heterogeneous within the tumor [9]. In severely hypoxic regions the Col1 fiber volume was significantly lower and the Col1 inter-fiber distance was significantly greater as compared to normoxic regions as previously described [9].

Since we used FCM features extraction and match features from MRI and optical imaging, it was necessary to validate the registration technique for these multimodality imaging data. We therefore calculated the registration error using the Dice similarity index. The registration was only considered acceptable for cases in which the Dice similarity index was greater than 0.85. Both elastic and non-rigid registration [25, 26] were also evaluated. However, in our case, the internal features were distorted by these techniques, which caused a loss of information as was evident from the low Dice similarity index. We therefore used rigid affine transformation for the registration of the optical and MRI data, which resulted in an overlap of greater than 85% ( $N = 10$ ) for the Dice similarity index. Dice similarity index values of greater than 85% of overlap were considered successful for multimodality co-registration.

Higher MMCA draining rates and draining volumes were observed in normoxic regions that also exhibited a denser mesh of collagen fibers. In contrast, there were lower draining rates and draining volume in hypoxic regions that also exhibited fewer and structurally altered collagen 1 fibers. Higher MMCA pooling rate and pooling volume were observed in the normoxic regions as compared to the hypoxic regions. These data suggest that hypoxic areas are like 'silent zones' with very little movement of MMCA as detected by this method. These data have significant implications in the transport of macromolecular therapeutic agents as they suggest that there is very little macromolecular trafficking in the ECM in hypoxic regions. This is most likely a combination of the low vascular volume and permeability resulting in low delivery as well as the sparse collagen fibers that seem to mediate transport.

In tumors such as pancreatic cancer, the dense mesh of Col1 fibers has been reported to act as a barrier to drug delivery, and Col1 depletion treatments are being developed to improve delivery [15, 27-29]. This fibrosis, which is typically observed in the desmoplastic stroma of pancreatic cancer, is very dense compared to what we observed in this human breast cancer xenograft model, and to what is typically observed in human breast cancers [16]. A Col1 fiber density of 25%, which we observed in normoxic regions, provides sufficient space for macromolecular transport, and in fact, our data suggest that these Col1 fibers act as guiding paths to the MMCA in the extracellular space. Since we are measuring phenomena on different spatial scales, we cannot comment on the relationship between sub-voxel variations in Col1 density and the corresponding macromolecular transport.

Immediately adjacent to the strongly hypoxic regions, a denser Col1 fiber network was observed together with increased macromolecular movement. These data suggest that these fibers may provide avenues for opportunistic hypoxic cells, which have several invasive genes upregulated due to hypoxia, escaping from this hostile environment. HIF stabilization under hypoxia transcriptionally activates several genes such as urokinase-type plasminogen-activator receptor (uPAR), matrix metalloproteinase-2 (MMP-2), autocrinemotility factor (AMF), transforming growth factor- $\alpha$  (TGF- $\alpha$ ), cathepsin-D (CATHD), fibronectin 1 (FN1), keratin 14 (KRT14), keratin 18 (KRT18), keratin 19 (KRT19), vimentin (VIM), c-MET tyrosine kinase that regulate invasion [2]. Col1 fibers have been shown to provide avenues for malignant cancer cells to travel along during their metastatic journey [7, 16, 30]. Cancer cells can rapidly traverse through tumors along linear Col1 fibers [30]. Since some of these fibers converge with blood vessels, this can promote intravasation in the metastatic cascade [30]. Integrins such as  $\alpha 2\beta 1$  facilitate breast cancer cell attachment to Col1 fibers [31]. Provenzano et al. [7] have observed that cancer cells travel along radially aligned Col1 fiber to metastasize and that more aggressive tumor types have characteristic tumor-associated Col1 structures (TACS). The TACS classified as TACS 3 displays aligned Col1 fibers that are oriented perpendicular to regions of tumor cells, which are moving along these Col1 fibers as guiding paths for metastasis [7, 32]. A study with 196 patients demonstrated that TACS 3 is described predictor of survival in human breast cancer patients [32]. It was also observed that the Col1 fiber density was 45% higher in lymph node positive (LN+ve) human samples as compared to the lymph node negative (LN-ve) tumor samples and the Col1 fiber distribution in the LN+ve patient samples was more densely packed than in the LN-ve patient samples [16]. The present study adds to an emerging picture that the

stimulus for invasion and migration occurs from hypoxia, and the Col1 fibers provide avenues to escape from a hostile environment.

In summary, we have co-registered and quantified *in vivo* MRI and *ex vivo* optical imaging data to obtain structural and functional information of the tumor microenvironment in a human breast cancer xenograft model. These data highlight the importance of hypoxia and Col1 fibers in macromolecular transport. Further investigations into the role of the ECM and mechano-transduction pathways as well as cancer cell/fibroblast interactions and Col1 deposition under hypoxic conditions are merited to understand the role of the tumor microenvironment in ECM mediated drug delivery and metastasis.

### **Acknowledgement**

This work was supported by NIH R01CA136576, R01CA138515, R01CA73850, R01CA82337, P50CA103175, and P30CA006973. We gratefully acknowledge the expert assistance of Dr. Dmitri Artemov and Desmond Jacob. We thank Gary Cromwell for maintaining the cells and inoculating the tumors.

### **References**

1. Brown, J.M. and W.R. Wilson (2004). Exploiting tumour hypoxia in cancer treatment. *Nat Rev Cancer*. 4(6): 437-47.



2. Semenza, G.L. (2003). Targeting HIF-1 for cancer therapy. *Nat Rev Cancer*. 3(10): 721-32.
3. Brown, E., T. McKee, E. diTomaso, A. Pluen, B. Seed, Y. Boucher, and R.K. Jain (2003). Dynamic imaging of collagen and its modulation in tumors in vivo using second-harmonic generation. *Nat Med*. 9(6): 796-800.
4. Krishnamachary, B., M.F. Penet, S. Nimmagadda, Y. Mironchik, V. Raman, M. Solaiyappan, G.L. Semenza, M.G. Pomper, and Z.M. Bhujwalla (2012). Hypoxia regulates CD44 and its variant isoforms through HIF-1alpha in triple negative breast cancer. *PLoS One*. 7(8): e44078.
5. Lochter, A. and M.J. Bissell (1995). Involvement of extracellular matrix constituents in breast cancer. *Semin Cancer Biol*. 6(3): 165-73.
6. Serebriiskii, I., R. Castello-Cros, A. Lamb, E.A. Golemis, and E. Cukierman (2008). Fibroblast-derived 3D matrix differentially regulates the growth and drug-responsiveness of human cancer cells. *Matrix Biol*. 27(6): 573-85.
7. Provenzano, P.P., K.W. Eliceiri, J.M. Campbell, D.R. Inman, J.G. White, and P.J. Keely (2006). Collagen reorganization at the tumor-stromal interface facilitates local invasion. *BMC Med*. 4(1): 38.
8. Provenzano, P.P., D.R. Inman, K.W. Eliceiri, J.G. Knittel, L. Yan, C.T. Rueden, J.G. White, and P.J. Keely (2008). Collagen density promotes mammary tumor initiation and progression. *BMC Med*. 6: 11.
9. Kakkad, S.M., M. Solaiyappan, B. O'Rourke, I. Stasinopoulos, E. Ackerstaff, V. Raman, Z.M. Bhujwalla, and K. Glunde (2010). Hypoxic Tumor Microenvironments Reduce Collagen I Fiber Density. *Neoplasia*. 12(8): 608-617.

10. Falanga, V., L. Zhou, and T. Yufit (2002). Low oxygen tension stimulates collagen synthesis and COL1A1 transcription through the action of TGF-beta 1. *Journal of Cellular Physiology*. 191(1): 42-50.
11. Gilkes, D.M., P. Chaturvedi, S. Bajpai, C.C. Wong, H. Wei, S. Pitcairn, M.E. Hubbi, D. Wirtz, and G.L. Semenza (2013). Collagen prolyl hydroxylases are essential for breast cancer metastasis. *Cancer Res*. 73(11): 3285-96.
12. Swartz, M.A. (2001). The physiology of the lymphatic system. *Adv Drug Deliv Rev*. 50(1-2): 3-20.
13. Jain, R.K. (1987). Transport of molecules in the tumor interstitium: a review. *Cancer Res*. 47(12): 3039-51.
14. Netti, P.A., D.A. Berk, M.A. Swartz, A.J. Grodzinsky, and R.K. Jain (2000). Role of extracellular matrix assembly in interstitial transport in solid tumors. *Cancer Res*. 60(9): 2497-503.
15. Ramanujan, S., A. Pluen, T.D. McKee, E.B. Brown, Y. Boucher, and R.K. Jain (2002). Diffusion and convection in collagen gels: implications for transport in the tumor interstitium. *Biophys J*. 83(3): 1650-60.
16. Kakkad, S.M., M. Solaiyappan, P. Argani, S. Sukumar, L.K. Jacobs, D. Leibfritz, Z.M. Bhujwala, and K. Glunde (2012). Collagen I fiber density increases in lymph node positive breast cancers: pilot study. *J Biomed Opt*. 17(11).
17. Cailleau, R., R. Young, M. Olive, and W.J. Reeves, Jr. (1974). Breast tumor cell lines from pleural effusions. *J Natl Cancer Inst*. 53(3): 661-74.
18. Raman, V., D. Artemov, A.P. Pathak, P.T. Winnard, Jr., S. McNutt, A. Yudina, A. Bogdanov, Jr., and Z.M. Bhujwala (2006). Characterizing vascular parameters in

- hypoxic regions: a combined magnetic resonance and optical imaging study of a human prostate cancer model. *Cancer Res.* 66(20): 9929-36.
19. Pathak, A.P., D. Artemov, B.D. Ward, D.G. Jackson, M. Neeman, and Z.M. Bhujwala (2005). Characterizing extravascular fluid transport of macromolecules in the tumor interstitium by magnetic resonance imaging. *Cancer Res.* 65(4): 1425-32.
  20. Dunn, J.C. (1973). A fuzzy relative of the ISODATA process and its use in detecting compact, well-separated clusters. *Journal of Cybernetics.* 3(3): 32-57.
  21. Miyamoto, S., H. Ichihashi, and K. Honda (2008). Algorithms for Fuzzy Clustering: Methods in c-Means Clustering with Applications. *Algorithms for Fuzzy Clustering: Methods in C-Means Clustering with Applications.* 229: 1-247.
  22. Pajares, G. and J.M. de la Cruz (2004). A wavelet-based image fusion tutorial. *Pattern Recognition.* 37(9): 1855-1872.
  23. Collignon, A., F. Maes, D. Delaere, D. Vandermeulen, P. Suetens, and G. Marchal (1995). Automated multi-modality image registration based on information theory. *Information Processing in Medical Imaging.* 3: 263-274.
  24. Dice, L.R. (1945). Measures of the Amount of Ecologic Association between Species. *Ecology.* 26(3): 297-302.
  25. Rueckert, D., L.I. Sonoda, C. Hayes, D.L.G. Hill, M.O. Leach, and D.J. Hawkes (1999). Nonrigid registration using free-form deformations: Application to breast MR images. *IEEE Trans Med Imaging.* 18(8): 712-721.
  26. Chappelow, J., B.N. Bloch, N. Rofsky, E. Genega, R. Lenkinski, W. DeWolf, and A. Madabhushi (2011). Elastic registration of multimodal prostate MRI and histology via multiattribute combined mutual information. *Medical Physics.* 38(4): 2005-2018.

27. Olive, K.P., M.A. Jacobetz, C.J. Davidson, A. Gopinathan, D. McIntyre, D. Honess, B. Madhu, M.A. Goldgraben, M.E. Caldwell, D. Allard, K.K. Frese, G. Denicola, C. Feig, C. Combs, S.P. Winter, H. Ireland-Zecchini, S. Reichelt, W.J. Howat, A. Chang, M. Dhara, L. Wang, F. Ruckert, R. Grutzmann, C. Pilarsky, K. Izeradjene, S.R. Hingorani, P. Huang, S.E. Davies, W. Plunkett, M. Egorin, R.H. Hruban, N. Whitebread, K. McGovern, J. Adams, C. Iacobuzio-Donahue, J. Griffiths, and D.A. Tuveson (2009). Inhibition of Hedgehog signaling enhances delivery of chemotherapy in a mouse model of pancreatic cancer. *Science*. 324(5933): 1457-61.
28. Provenzano, P.P., C. Cuevas, A.E. Chang, V.K. Goel, D.D. Von Hoff, and S.R. Hingorani (2012). Enzymatic targeting of the stroma ablates physical barriers to treatment of pancreatic ductal adenocarcinoma. *Cancer Cell*. 21(3): 418-29.
29. Li, J., M.G. Wientjes, and J.L. Au (2010). Pancreatic cancer: pathobiology, treatment options, and drug delivery. *AAPS J*. 12(2): 223-32.
30. Condeelis, J. and J.E. Segall (2003). Intravital imaging of cell movement in tumours. *Nat Rev Cancer*. 3(12): 921-30.
31. Maemura, M., S.K. Akiyama, V.L. Woods, and R.B. Dickson (1995). Expression and Ligand-Binding of Alpha-2-Beta-1 Integrin on Breast-Carcinoma Cells. *Clinical & Experimental Metastasis*. 13(4): 223-235.
32. Conklin, M.W., J.C. Eickhoff, K.M. Riching, C.A. Pehlke, K.W. Eliceiri, P.P. Provenzano, A. Friedl, and P.J. Keely (2011). Aligned Collagen Is a Prognostic Signature for Survival in Human Breast Carcinoma. *American Journal of Pathology*. 178(3): 1221-1232.

## Chapter 5

---

### Collagen fibers mediate water diffusion and anisotropy

Manuscript in preparation

Collagen fibers influence water diffusion and anisotropy.

**Samata M. Kakkad**, Jiangyang Zhang, Alireza Akhbardeh, Desmond Jacob, Meiyappan Solaiyappan, Mike Jacobs, Venu Raman, Dieter Leibfritz, Kristine Glunde, Zaver M. Bhujwalla

**Abbreviation footnote**

2D, two-dimensional

3D, three-dimensional

aDW, average diffusion weighted

ADC, apparent diffusion coefficient

Coll, collagen 1

DTI, diffusion tensor imaging

ECM, extracellular matrix

ER, estrogen receptor

FA, fractional anisotropy

FOV, field of view

H&E, hematoxylin and eosin

HER-2, human epidermal growth factor receptor 2

HIF-1, hypoxia inducible factor

HRE, hypoxia response element

IDC, invasive ductal carcinoma

LN, lymph node

MRI, magnetic resonance imaging

PR, progesterone receptor

RFP, red fluorescent protein

SCID, severe combined immunodeficient

SHG, second harmonic generation

VEGF-A, vascular endothelial growth factor A

## Abstract

Collagen 1 (Col1) fibers play an important role in macromolecular transport and cancer cell dissemination. Our goal in this study was to understand the influence of Col1 fibers on water diffusion, and to examine the potential of using noninvasive diffusion tensor imaging (DTI) to detect Col1 fibers in breast lesions. We have previously observed in genetically engineered human MDA-MB-231 breast cancer xenograft tumors that fluoresce under hypoxia that fluorescing hypoxic regions contain relatively low amounts of collagen 1 fibers. The same tumor model was used to further investigate the relationship between Col1 fibers, water diffusion and anisotropy, and hypoxia. We observed for the first time that water diffusion and anisotropy followed the Col1 fiber distribution in human breast cancer specimens. In regions with low Col1 fiber content, apparent diffusion coefficient (ADC) and fractional anisotropy (FA) values decreased significantly as compared to regions containing dense Col1 fibers (p-value < 0.05). In the breast cancer xenograft model, we observed that hypoxic regions with significantly lower Col1 fiber volume had significantly lower ADC and FA values as compared to normoxic tumor regions with higher Col1 fiber volume. Lastly, we performed *in vivo* DTI measurements to confirm that DTI patterns in tumors observed *in vivo* spatially co-localized with DTI patterns observed *ex vivo* in the same tumors. These studies have identified the potential use of noninvasive DTI as a biomarker to detect Col1 fiber density and further confirm the importance of Col1 fibers in molecular transport through the ECM.

## Introduction

Collagen 1 (Col1) fibers are a major structural component of the extracellular matrix of tumors [1]. Malignant breast cancers are characterized by significantly higher Col1 fiber density and an altered Col1 architecture [2]. Increased mammary Col1 fiber density was shown to cause mammary tumor initiation, progression, and metastasis [2]. Col1 fibers play an important role in macromolecular transport and cancer cell dissemination [3, 4]. Cancer cells travel along aligned Col1 fibers [4, 5], and tumor associated Col1 fiber alignment was identified to be a prognostic signature for survival in breast cancer patients [6]. Col1 fibers can be detected with second harmonic generation (SHG) microscopy [1]. SHG microscopy of Col1 fibers detects an intrinsic signal derived from the ability of the noncentrosymmetric molecular structure of Col1 fibers to give rise to frequency doubling called the second harmonic [1, 7]. Optical imaging such as SHG microscopy has limitations of depth penetration, and unless the tissue is superficial or exposed for *in vivo* imaging, or biopsied for *ex vivo* imaging, optical imaging cannot be used as a noninvasive imaging modality.

Diffusion tensor imaging (DTI) has been extensively used to examine tissue microstructure and white matter pathology in neurological diseases, as well as for white matter tractography [8]. Water molecules predominantly diffuse along neuronal fibers, as diffusion across fibers is restricted by axonal membranes and, in the case of myelinated axons, myelin sheaths. Several DTI parameters, e.g. ADC and FA, have been used to visualize fiber tracts and quantitatively measure white matter integrity [8]. Analogous to white matter tracts in the brain, the extracellular matrix (ECM) of breast cancers contains Col1 fibers that may mediate the



patterns of water diffusion in terms of the extent of water diffusion as measured by ADC, the degree of anisotropy as measured by FA, and the primary direction of water molecule diffusion as measured by the primary eigenvector of estimated diffusion tensor. It was recently shown that DTI was able to detect the Col1 architecture, as validated by SHG microscopy, in the carotid artery [9]. These studies identified the potential use of DTI as a noninvasive imaging technique to detect and map Col1 fibers [9]. Diffusion MRI is currently being evaluated to detect breast cancer, since cancers typically show restricted diffusion [10]. Here we have investigated the association between diffusion and anisotropy with breast cancer Col1 fiber distribution, to determine if DTI can provide noninvasive imaging indices of Col1 fibers that can be used as biomarkers for aggressiveness.

DTI was combined with SHG microscopy to determine the influence of the Col1 fiber density in breast cancer on water diffusion, and to evaluate the potential of diffusion MRI in studying Col1 fibers in cancer. We initially performed a retrospective study of human breast cancer samples to determine the correlation between Col1 fibers and water diffusion in these samples. We have previously observed that hypoxic regions, identified by red fluorescence in an MDA-MB-231 human breast cancer xenograft model engineered to express red fluorescent protein under hypoxia, typically contain few Col1 fibers [11]. We therefore characterized diffusion in hypoxic and normoxic regions of these tumors in *ex vivo* studies to further validate the relationship between Col1 fibers and diffusion. We also performed an *in vivo* – *ex vivo* DTI comparison of these tumors to verify that diffusion patterns observed *in vivo* spatially matched those observed *ex vivo*. It was important to establish that patterns observed *ex vivo* were

spatially similar to those observed *in vivo*, since our ultimate purpose was to determine if DTI parameters provided noninvasive indices of Col1 fiber distribution in tumors.

We found, for the first time, that high Col1 fiber density correlated with increased apparent diffusion coefficient (ADC) and fractional anisotropy (FA). Consistent with our previous observations, hypoxic regions contained significantly fewer Col1 fibers [11], and were characterized by a lower ADC and FA compared to normoxic tumor regions. Diffusion patterns observed *in vivo* were spatially similar to those observed *ex vivo*, suggesting that noninvasive DTI can be used to evaluate Col1 fiber density in tumors. These data also suggest that DTI can detect tumor hypoxia through a decrease in Col1 fiber density and highlight the importance of Col1 fibers in molecular transport through the ECM.

## Methods

An outline of the workflow is summarized in Figure 1. Three separate studies were performed here. In the first study, we investigated the correlation of water diffusion with Col1 fiber distribution in surgically resected human breast cancer samples. To study this, three-dimensional (3D) high-resolution DTI was performed on these samples (Figure 1, Human Sample *Ex Vivo* Studies). Following DTI acquisition, the sample was cryosectioned alternately at 100  $\mu\text{m}$  and 10  $\mu\text{m}$  thickness. Tile scan SHG microscopy to cover the entire tissue section was performed to quantify Col1 fibers throughout the 100  $\mu\text{m}$  sections. The 10  $\mu\text{m}$  sections were used for histological staining with hematoxylin and eosin (H&E) to identify necrosis. The ADC and FA maps were quantified from DTI. Col1 fibers were quantified for fiber density as

described subsequently in the “SHG and Confocal Microscopy” section. To correlate water diffusion and Col1 fiber distribution, SHG images were co-registered to the corresponding DTI sections as described in the “Co-registration Strategy for *Ex Vivo* and *In Vivo* Localization Quantification” section.

In the second study, MDA-MB-231 breast cancer xenografts genetically engineered to express tdTomato red fluorescent protein under hypoxia (MDA-MB-231-HRE-tdTomato) were used to further investigate the relationship between water diffusion and Col1 fibers. 3D high-resolution DTI was performed on excised breast cancer xenografts (Figure 1, Tumor xenograft *ex vivo* studies). Following DTI, the tumor was sectioned at 1 mm slice thickness using an acrylic adjustable tissue slicer (12 mm depth up to 25 mm width; Braintree Scientific, Inc., Braintree, MA) and tissue slicer blades (Braintree Scientific, Inc.). Fluorescence field optical images were acquired in the red channel to visualize hypoxic tumor regions. SHG tile scans were performed on these sections to quantify Col1 fibers. The slices were then given to our pathology laboratory for paraffin-embedding and sections were stained with hematoxylin and eosin (H&E).

In the third study, we correlated *in vivo* DTI data to *ex vivo* DTI data to validate our *ex vivo* data and evaluate the feasibility of clinically translating this method. *In vivo* DTI imaging was performed on MDA-MB-231-HRE-tdTomato breast cancer xenografts (Figure 1, Breast Cancer Xenograft *In Vivo* Studies). Following imaging, each tumor was excised and the same workflow as described in the second study was followed. Briefly, the tumor was fixed and *ex vivo* 3D high-resolution DT images were acquired, following which the tumor was sectioned at 1

mm slice thickness and hypoxic regions identified by optical imaging. SHG microscopy data were acquired to quantify Col1 fibers, and the sections were stained with H&E to mask out necrotic areas where present.

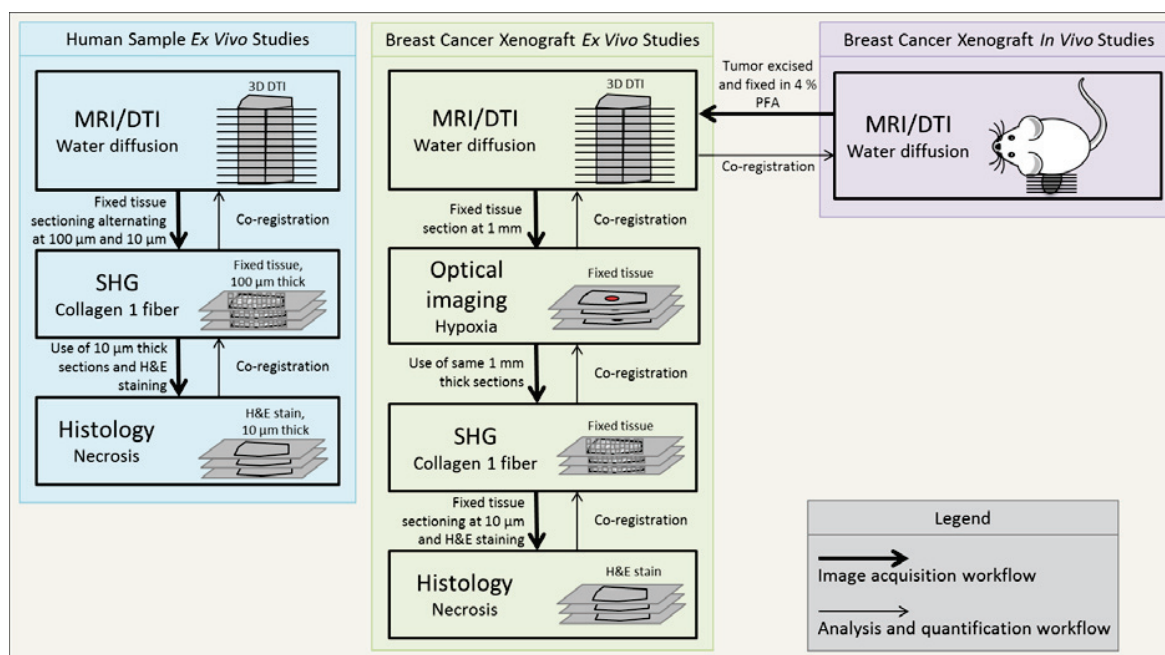


**Figure 1:** Schematic outline of the workflow. The blue box summarizes the workflow for our *ex vivo* study with human breast cancer specimens. Samples were fixed and 3D DTI images were acquired, after which the tumor was sectioned alternately at 100  $\mu\text{m}$  thickness and 10  $\mu\text{m}$  thickness to acquire SHG microscopic images of the Col1 fiber distribution and for H&E staining, respectively. For image analysis, H&E sections were co-registered to the corresponding SHG images to mask out any necrotic areas, and SHG sections were co-registered to the corresponding DTI sections to calculate ADC and FA values. The green box summarizes the workflow for our *ex vivo* study of breast cancer xenografts. 3D DTI was performed on fixed MDA-MB-231-HRE-tdTomato tumors excised from mice, following which tumors were sectioned at 1 mm slice thickness to visualize hypoxic regions using optical imaging. Col1 fiber distribution was obtained by SHG microscopy, after which tumor slices were further sectioned to prepare H&E stained sections. For data analysis, H&E sections were co-registered to the corresponding SHG images to mask out necrotic regions. SHG sections were registered to fluorescent images to map out hypoxic regions. Both SHG Col1 and hypoxia images were co-registered to the corresponding DTI sections to calculate ADC, FA and Col1 fiber distribution in hypoxic and normoxic tumor regions. The purple block summarizes the workflow for our *in vivo* study with MDA-MB-231-HRE-tdTomato breast cancer xenografts. DTI acquisitions were done *in vivo*, following which tumors were excised and fixed in 4% PFA. These excised tumors were put through the same experimental and analysis steps as described in the workflow for our *ex vivo* studies in breast cancer xenografts. Briefly, H&E sections were co-registered to SHG sections, which were co-registered to hypoxia images and *ex vivo* DTI images, all of which were then co-registered to *in vivo* DTI images. These co-registered *in vivo* and *ex vivo* images were used to calculate the correlation between *in vivo* and *ex vivo* measurements for ADC and FA values. Thick arrows indicate the image acquisition workflow, while thin arrows represent the quantification and analysis workflow.

### *Clinical Specimens*

In proof of principle studies, we performed DTI and SHG microscopy on two invasive ductal carcinoma (IDC) breast cancer specimens. One of the tumors was classified as stage IIB and the second tumor as stage IIIA. Both tumors were grade 3, estrogen receptor positive (ER+), progesterone receptor positive (PR+), Her2 positive (HER2+), and lymph node positive (LN+). Both samples were obtained from Integrated Laboratory Services - Biotech (Chestertown, MD, USA).

### *Breast Cancer Xenografts*

The triple-negative metastatic human MDA-MB-231 breast cancer cell line [12] was obtained from the American Type Culture Collection (ATCC, Rockville, MD) and maintained as previously described [13]. To obtain an optical reporter for hypoxia, MDA-MB-231 cells were stably transfected with a construct containing five copies of the hypoxia response element (HRE) of the human vascular endothelial growth factor A (VEGF-A) gene ligated to the cDNA of tdTomato red fluorescence protein (RFP), which produced MDA-MB-231-HRE-tdTomato cells as previously described and validated [14] [Also refer to Thesis Chapter 4]. Before inoculation, cells were routinely checked for hypoxia driven tdTomato fluorescence. Two million MDA-MB-231-HRE-tdTomato cells were orthotopically inoculated in the right upper thoracic mammary fat pad of anesthetized female severe combined immunodeficient (SCID) mice. MDA-MB-231-HRE-tdTomato tumor xenografts reached their final experimental size of

approximately 500 mm<sup>3</sup> within 8 weeks. *Ex vivo* studies were performed on 5 tumors and *in vivo-ex vivo* studies were performed on 2 tumors.

### *SHG and Confocal Microscopy*

For the first study, following diffusion imaging, the tumor was cryosectioned alternately at 100  $\mu\text{m}$  and 10  $\mu\text{m}$  slice thickness. Tile scan SHG microscopy was performed to acquire Col1 fibers from the entire tumor slice on the 100  $\mu\text{m}$  thick section. For the second and third study, tumors were sectioned at 1 mm slice thickness using an acrylic adjustable tissue slicer (12 mm depth up to 25 mm width; Braintree Scientific, Inc., Braintree, MA) and tissue slicer blades (Braintree Scientific, Inc.). Hypoxic regions were visualized by fluorescence microscopy in 1 mm thick slices using a 1 $\times$  objective attached to a Nikon inverted microscope, equipped with a Nikon Coolpix digital camera (Nikon Instruments, Inc., Melville, NY). Bright field images were acquired to assess tissue architecture and fluorescence images to detect hypoxic regions, followed by tile scan SHG microscopy of the entire slice to acquire Col1 fiber maps. We used a Zeiss 710 NLO Meta confocal microscope (Carl Zeiss Micro-Imaging, Inc.) and an Olympus Laser Scanning FV1000 MPE multiphoton microscope (Olympus Corp., US headquarters - Center Valley, PA) to acquire Col1 fibers in 3D by SHG microscopy. An incident laser line of 880 nm/860 nm (Zeiss/Olympus) was used, and the SHG signal from Col1 fibers was detected at 410-470 nm, as previously described [11, 15] (Chapter 4). On both microscope systems, a 25 $\times$  lens was used to acquire confocal z-stacks with tile scan acquisition performed in x and y directions to cover the entire tissue section (339.84  $\mu\text{m}$  x 339.84  $\mu\text{m}$  for the Zeiss microscope and 390  $\mu\text{m}$  x 390  $\mu\text{m}$  for the Olympus microscope), and z-intervals of approximately 5  $\mu\text{m}$ .

Col1 fiber quantification analysis was done in MATLAB R2011b (The MathWorks, Natick, MA). Two major structural characteristics of the Col1 fiber network in the ECM were computed using image processing techniques: (i) spatial characteristics were derived using Euclidean distance maps to collectively represent the sparseness and density of the distribution [11]; (ii) Col1 fiber textural patterns were characterized using texture analysis [16]. For spatial characterization, the inter-fiber distance was calculated to account for the empty spaces between fibers, and the fiber volume was calculated to assess fiber density [11]. Textural characteristics were computed by a statistics based texture analysis method that calculates the two-dimensional (2D) histogram of the image referred to as the co-occurrence matrix [16]. Haralick texture features were extracted from the resulting co-occurrence matrix [17]. Haralick texture features extract fibers and evaluate the spatial inter-relations of these fibers that vary across the tissue from straight and aligned fibers to wavy and crisscrossing fibers, which are described by 13 Haralick features [17]. The texture features entropy, energy, variance, maximum probability and inverse variance were able to distinguish between the different Col1 fiber patterns and gave a heterogeneous map matching the heterogeneous fiber patterns observed. Only these features were then used for further processing. By using fuzzy C-mean clustering [18], Haralick texture features were clustered and color-coded in 3D projected SHG images to represent the 3D fiber information in 2D.

Following SHG image acquisition, sections were given to our pathology laboratory for paraffin-embedding and sectioning with a microtome at 5  $\mu\text{m}$  thickness for immunohistochemistry. These sections were stained with H&E.

### *Ex Vivo DTI Acquisition*

The samples (human specimens, N=2, and excised xenograft tumors, N=7) were fixed for 24 hours in 4% paraformaldehyde, and washed with phosphate buffered saline for 72 h. The samples were spatially marked and placed in a 10 mm NMR tube immersed in Fomblin perfluoro polyether solution (Solvay Sollexis). MRI was performed on a Bruker Avance NMR spectrometer (Bruker Biospin, Billerica, MA, USA) equipped with a vertical 11.7 Tesla magnet and micro-imaging accessories. A Micro 2.5 gradient set capable of maximum 1500 mT/m gradient strength with a 10 mm birdcage volume coil was used. High-resolution T2- weighted MRI, and DTI of the sample were performed in three dimensions (3D) with an isotropic resolution of  $62.5 \times 62.5 \times 62.5 \mu\text{m}^3$ . DTI was performed using a modified 3D diffusion-weighted gradient and spin echo (DW-GRASE) sequence [19] with the following parameters: TE/TR = 36/1500 ms, 4 signal averages, two non-diffusion weighted images and six diffusion directions,  $b=1500 \text{ s/mm}^2$ , field of view (FOV) = 8 mm x 8 mm x 9 mm, a matrix size of 128 x 128 x 150, and. From these images, the average diffusion-weighted (aDW) images and maps of apparent diffusion coefficient (ADC) and fractional anisotropy (FA) were calculated using DTI Studio image processing software [20].

### *In Vivo DTI Acquisition*

To validate our *ex vivo* observations of water diffusion, we performed *in vivo* DTI on MDA-MB-231-5HRE-TdTomato breast cancer xenografts as described above. A horizontal 11.7T Bruker system (Bruker Corp., Billerica, MA, USA) was used to acquire the DTI with a 10



mm diameter solenoid coil. High-resolution T2-weighted anatomical images of the tumor were acquired followed by diffusion-weighted images. Coronal sections were acquired as shown in Figure 1, (Tumor Xenograft *In Vivo* Studies). Mice were anesthetized with isoflurane (1%) in air and oxygen mixed at 3:1 ratio via vaporizer and positioned in an animal holder (Bruker BioSpin, Billerica, MA, USA). Respiration was monitored via pressure sensor (SAII, Stony Brook, NY, USA) and maintained at 40–60 breaths per minute. T2-weighted images were acquired using a RARE sequence with imaging parameters of TE/TR = 12.31/3000 ms, 8 averages, FOV = 14 mm x 10 mm, and matrix of 192 by 144 with 20 z-slices of 0.4 mm thickness. For the same FOV, diffusion-weighted images were acquired using a modified EPI sequence with imaging parameters of TE/TR = 23.6/5000 ms, 2 repetitions, 5 non-diffusion weighted and 30 diffusion directions, b-value  $\sim 1500$  s/mm<sup>2</sup>, FOV = 14 mm x 10 mm, matrix size of 128 x 96, native imaging resolution = 0.105 mm x 0.105 mm, and 20 z-slices. Similar to *ex vivo* DTI image quantification, aDW, ADC, and FA maps were calculated for *in vivo* DTI images using DTI Studio software [20].

#### *Co-registration Strategy for Ex Vivo and In Vivo Localization Quantification*

For localization and correlation quantification of Coll fibers, hypoxia and water diffusion, affine transformation based co-registration was performed as previously described [21] (Chapter 4). For the third study, *ex vivo* DTI images were first co-registered to corresponding *in vivo* DTI data. After this, and similar to the second study, optical hypoxia images were co-registered to the registered *ex vivo* DTI data. In both second and third studies, SHG images were co-registered to the registered hypoxia images. For the first study, SHG images were co-

registered to the corresponding *ex vivo* DTI images for localization quantification. After every step of co-registration the Dice similarity index [22] was calculated to evaluate the co-registration error. For multimodal data of *ex vivo* DTI registered to *in vivo* DTI, and *ex vivo* optical data registered to *ex vivo* registered DTI, a Dice similarity index  $> 0.85$  was considered as a successful co-registration.

For the first study, we used a previously developed technique [23], where the histology image was used to predict the FA map. Here we used our SHG Col1 fiber distribution image to predict the water diffusion image. Briefly, we initially performed turkey window filtering and zero mean normalizing to the image to avoid edge and central spike effects, after which 2D fast Fourier transform was applied and a radial histogram was calculated from the resulting image, followed by principle component analysis to calculate anisotropy and primary orientation [23]. The predicted diffusion and water diffusion direction maps were compared to the DTI ADC, FA and color-coded water direction maps. This code was written in MATLAB and was developed and validated in Dr. Jiangyang Zhang's laboratory. Additionally, in the first study, ADC and FA values were calculated in masks of four segmented categories in the SHG images for density and sparseness and masks of three segmented categories for textural patterns. Fiber density and sparseness were classified into masks of dense fiber regions ( $75\% < \text{percent fiber volume}$ ,  $\text{inter-fiber distance} < 1 \mu\text{m}$ ), intermediate-1 fiber regions ( $50\% < \text{percent fiber volume} < 75\%$ ,  $2 \mu\text{m} < \text{inter-fiber distance} < 5 \mu\text{m}$ ), intermediate-2 fiber regions ( $25\% < \text{percent fiber volume} < 50\%$ ,  $2 \mu\text{m} < \text{inter-fiber distance} < 5 \mu\text{m}$ ) and sparse fiber regions ( $\text{percent fiber volume} < 25\%$ ,  $5 \mu\text{m} < \text{inter-fiber distance}$ ). The ADC and FA values were calculated in 10 equidistantly spaced regions of interests (ROIs) for each mask from each tumor. A two-sided t-test ( $\alpha = 0.05$ ) was used to

detect significant differences between ADC and FA values in the dense, intermediate-1, intermediate-2 and sparse fiber regions using Microsoft Office Excel 2007 (Microsoft, Redmond, WA). Similarly, three masks were segmented by fuzzy c-mean clustering [24, 25] from the combined Haralick texture feature maps into straight fibers, fibers of mixed patterns, and fibers of wavy pattern. ADC and FA values were calculated in 10 equidistantly spaced ROIs for each mask from each tumor. A two-sided t-test ( $\alpha = 0.05$ ) was used to detect significant differences between ADC and FA values for the straight, mixed and wavy Col1 fiber patterns using Microsoft Office Excel 2007 (Microsoft, Redmond, WA). P values  $< .05$  were considered to be significant.

In the second study, hypoxic regions were drawn out from co-registered optical bright field and fluorescence images. ADC and FA values were calculated in normoxic and hypoxic regions and compared for all mice (N=5). Percent fiber volume and inter-fiber distances were also calculated for hypoxic and normoxic regions. A two-sided t-test ( $\alpha = 0.05$ ) was used to detect significant differences between hypoxic and normoxic ROIs for ADC, FA and Col1 fiber quantification using Microsoft Office Excel 2007 (Microsoft, Redmond, WA). P values  $< .05$  were considered to be significant.

In the third study, *in vivo* DTI data were correlated with *ex vivo* DTI data. Pearson's correlation coefficient was calculated for *in vivo* and *ex vivo* ADC and FA maps for four slices from each tumor. In addition, ADC, FA and Col1 fibers were quantified in normoxic *versus* hypoxic regions as described for the second study. A one-sided t-test ( $\alpha = 0.05$ ) was used to

detect significant differences between hypoxic and normoxic ROIs using Microsoft Office Excel 2007 (Microsoft, Redmond, WA). P values < .05 were considered to be significant.

For all the studies, H&E sections from the imaged slices were co-registered to corresponding DTI images using affine transformation as described above. These co-registered H&E sections were used to detect necrotic regions. Necrotic regions, if present, were eliminated from quantification analysis.

## **Results**

### *Human Sample Ex Vivo Studies*

We observed distinct heterogeneities in the diffusion images of human breast cancer samples as apparent in the representative images shown in Figure 2. Displayed in Figure 2A-D are aDW image, ADC map, FA map, and the color-coded water diffusion directionality map, respectively. The corresponding H&E stained histological section is shown in Figure 2E. Coll fiber images acquired using SHG microscopy of the DT imaged slices displayed a similar distinct pattern as observed in the diffusion tensor images (Figure 2F). We simulated water diffusion and water diffusion directionality maps from the SHG data. The simulated results displayed in Figure 2G-H closely matched the actual ADC, FA and water diffusion directionality maps.

To characterize the Col1 fiber patterns, texture analyses of the SHG images were performed, and Haralick texture features were calculated. Using fuzzy c-mean clustering, Haralick texture features were clustered to color-code 2D projected SHG images with 3D fiber pattern information. This texture feature clustering was able to distinguish Col1 fiber patterns into three characteristic categories, which were straight fiber pattern, mixed patterns and wavy texture pattern (Figure 2I). An overlay of the ADC map (gray) with the SHG image (red) is displayed in Figure 2J, an overlay of the FA map (gray) with the SHG image (red) is displayed in Figure 2K, and an overlay of the FA map (gray) with the simulated diffusion map (red) is displayed in Figure 2L. These overlay images identified a close association between Col1 fibers and water diffusion and anisotropy.

Analysis of 10 ROIs for fiber content quantification and fiber distribution quantification are presented in Figure 3 for one of the tumors. We observed that regions with sparse fibers had significantly reduced ADC values ( $p$ -value  $< 0.01$ ,  $N = 10$ ) as compared to regions containing dense, intermediate-1 or intermediate-2 fiber content (Figure 3A). Fractional anisotropy values were significantly reduced ( $p$ -value  $< 0.01$ ,  $N = 10$ ) in regions with sparse fibers as compared to regions with dense, intermediate-1 or intermediate-2 Col1 fiber content (Figure 3B). The four fiber content masks of dense fibers regions (red), intermediate-1 fiber content (gray), intermediate-2 fiber content (green) and sparse Col1 fiber regions (blue) are shown in Figure 3C. Within the constraints of our texture analysis approach, we did not observe any differences in ADC or FA values for straight, mixed and wavy fiber patterns (Figure 3D-E,  $p$ -value  $> 0.05$ ,  $N = 10$ ). Texture analysis masks of straight (red), mixed (green) and wavy (blue) Col1 fiber patterns

are shown in Figure 3F. Similar differences were observed for both tumors but data from only one tumor are presented.

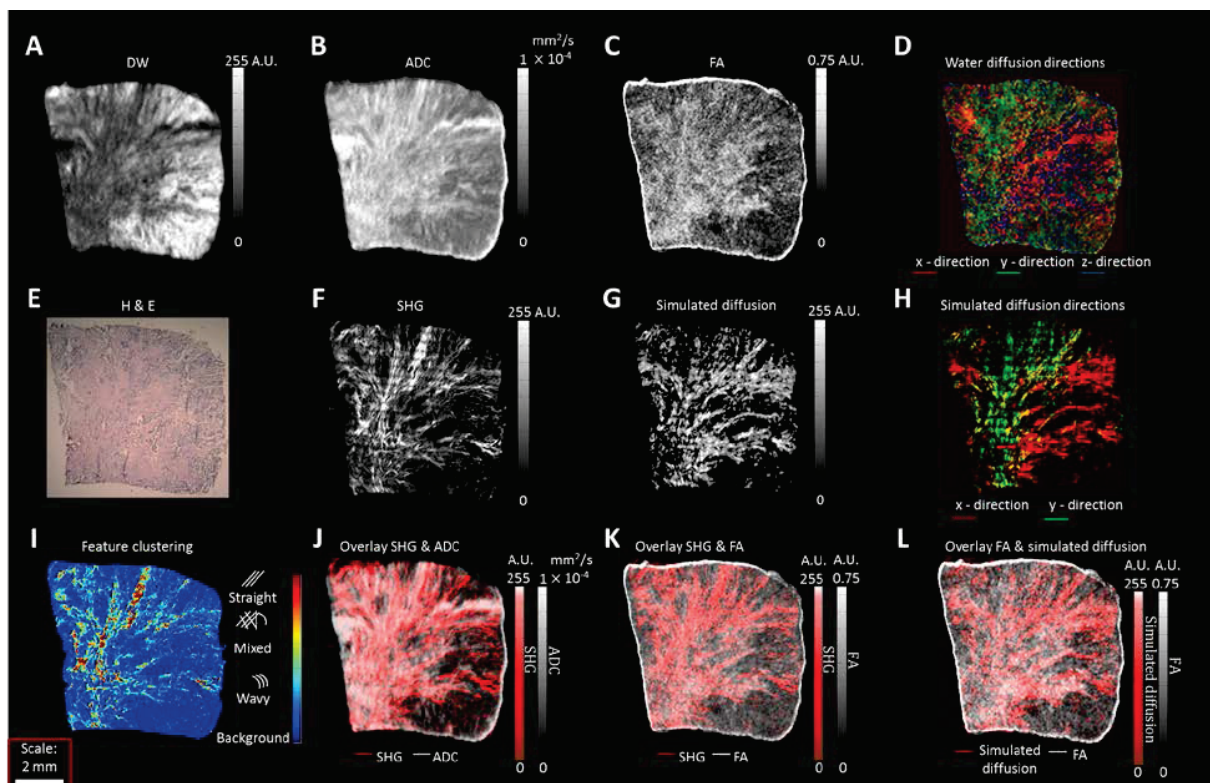


**Figure 2:** Representative images of a human breast cancer specimen. (A) A representative aDW image, (B) corresponding ADC map, (C) corresponding FA map, (D) corresponding water diffusion direction color map, (E) corresponding H&E section, (F) corresponding SHG map of Col1 fiber distribution. (G) Water diffusion and (H) water diffusion directionality simulated from SHG Col1 fiber images. (I) Color-coded SHG image for straight, mixed and wavy fiber patterns based on texture analysis, (J) overlay of ADC map (gray) and SHG image (red), (K) overlay of FA map (gray) and SHG image (red), and (L) overlay of measured FA map (gray) and simulated diffusion map (red). Scale bar of 2 mm for all images (A-L).

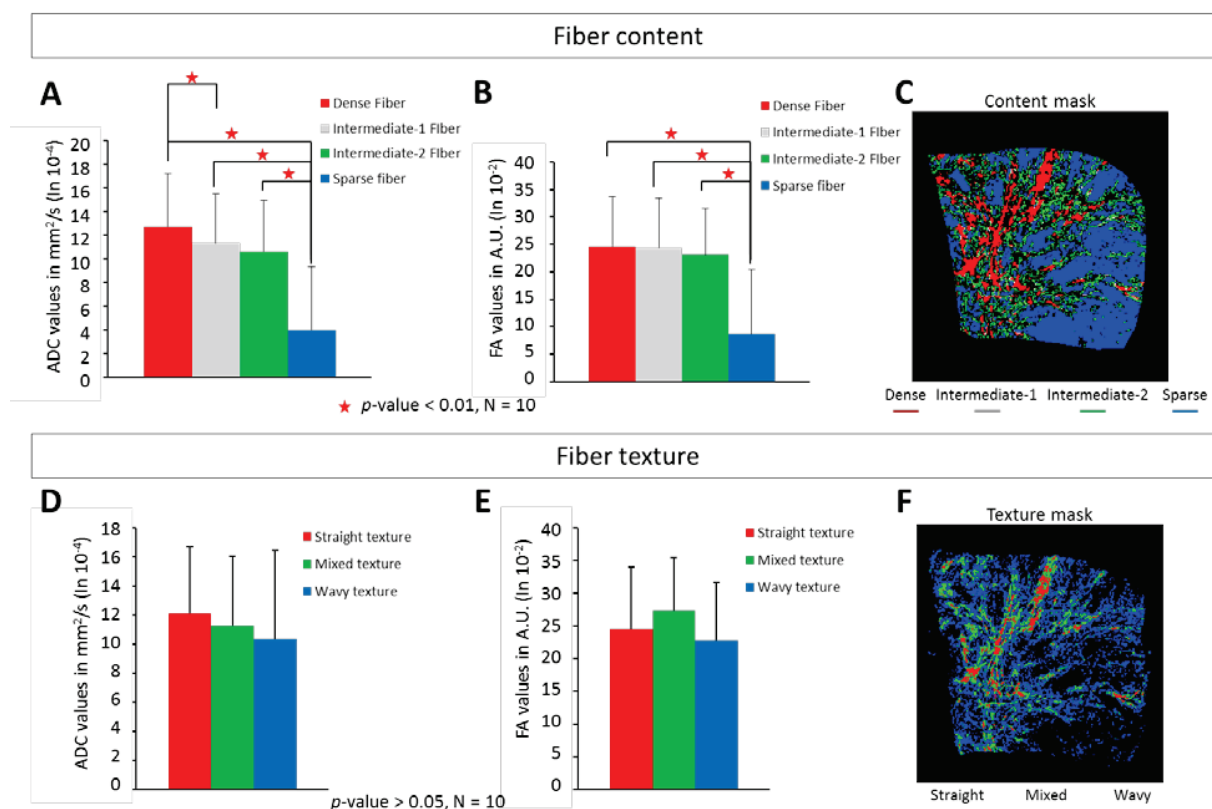


**Figure 3:** Quantification of DTI and Coll1 data obtained from a representative human breast cancer specimen. Significantly reduced (A) ADC values and (B) FA values were observed in regions that contained sparse Coll1 fibers as compared to regions with dense, intermediate-1 or intermediate-2 Coll1 fiber content ( $p$ -value < 0.01, N = 10). (C) Fiber content masks of dense (red), intermediate-1 (gray), intermediate-2 (green) and sparse fibers (blue). No differences in ADC and FA values were observed in the texture analysis shown in (D) and (E), respectively ( $p$ -value > 0.05, N = 10). (F) Texture analysis masks of straight (red), mixed (green) and wavy fibers (blue).

### Breast Cancer Xenograft Ex Vivo Studies

To further investigate the correlation between water diffusion and Coll1 fibers, and the influence of hypoxia on water diffusion, we performed additional studies in MDA-MB-231 breast cancer xenografts genetically engineered to express tdTomato red fluorescent protein under hypoxia. Representative images of *ex vivo* tumors are shown in Figure 4. Displayed in Figure 4A-D are aDW image, ADC map, FA map, and water diffusion directionality map,

respectively. The corresponding optical image showing hypoxic fluorescing regions in red is displayed in Figure 4E. Overlay images of ADC map (gray) and hypoxia (red), FA map (gray) and hypoxia (red), and SHG image (gray) and hypoxia (red) are displayed in Figure 4F-H, respectively, and demonstrate that hypoxic regions had lower ADC and FA values compared to normoxic regions. The H&E section obtained from the corresponding slice is shown in Figure 4I, and demonstrates that high ADC values were observed in frankly necrotic regions. These necrotic regions were eliminated from all analyses.

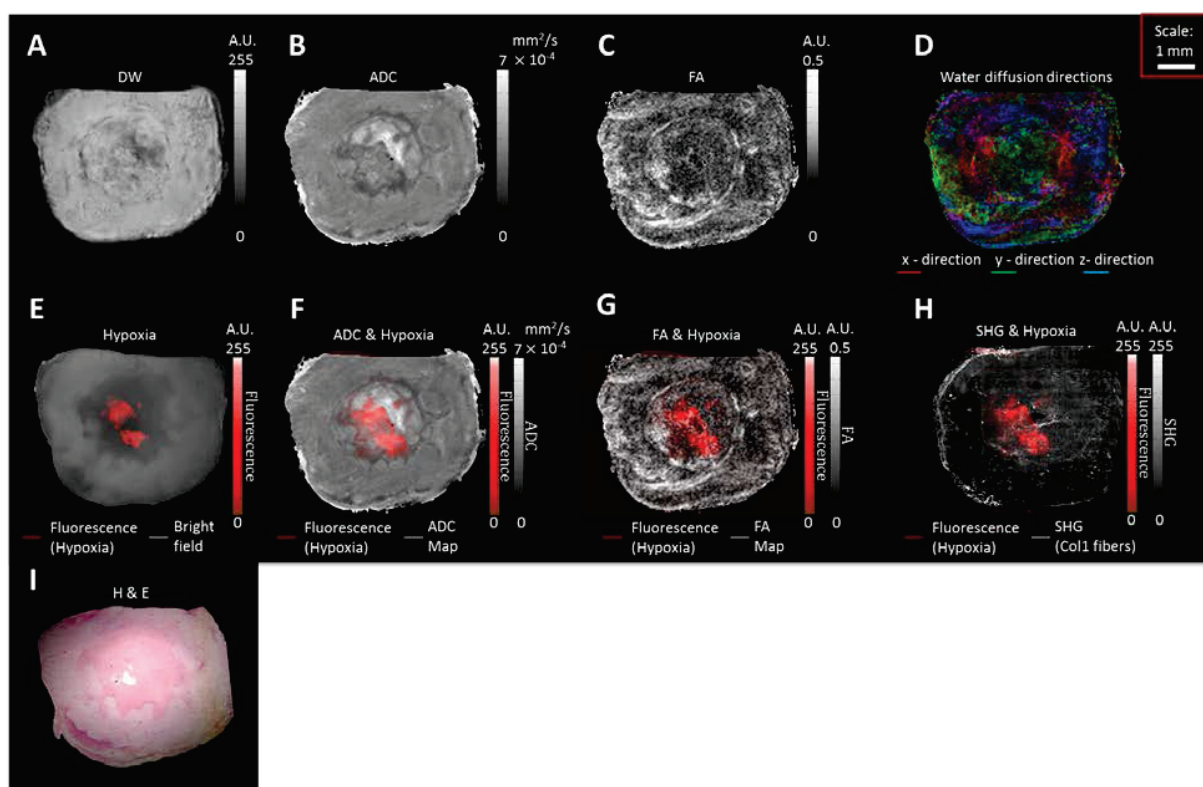


**Figure 4:** *Ex vivo* images from breast cancer xenografts. Representative corresponding (A) aDW image, (B) ADC map, (C) FA map, and (D) water diffusion directionality color map. (E) Corresponding optical image displaying hypoxic red fluorescing regions (red). (F-H) Overlay images of hypoxia (red) with ADC map (gray), FA map (gray), or SHG image (gray), respectively. (I) Corresponding H&E stained section.

Quantified data summarized for five tumors are shown in Figure 5. Hypoxic regions had significantly lower percent Col1 fiber volume as compared to normoxic regions (Figure 5A, p-



value = 0.0383, N = 3). Similar to our observation in human breast cancer specimens, these breast tumor models showed again that low Coll containing hypoxic areas had a significantly lower ADC value (Figure 5B, p-value = 0.0592, N = 5) and FA value (Figure 5C, p-value = 0.0308, N = 5) compared to normoxic regions.

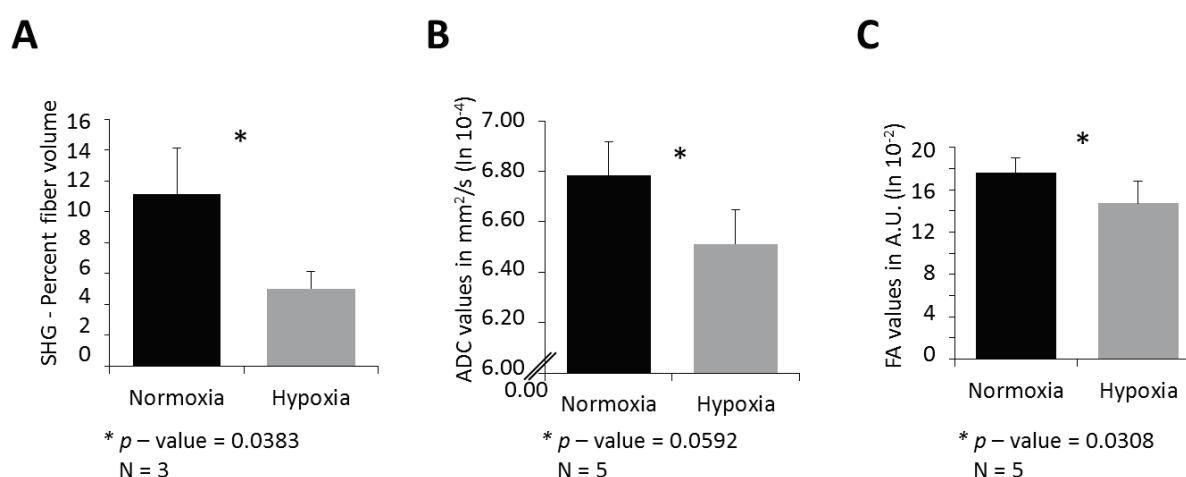


**Figure 5:** Quantification of DTI and hypoxia data obtained from breast cancer xenografts *ex vivo*. (A) Percent fiber volume was significantly lower in hypoxic regions as compared to normoxic regions (p-value = 0.0383, N = 3). Significantly lower (B) ADC and (C) FA values were observed in hypoxic regions as compared to normoxic regions (p-value = 0.0592 and p-value = 0.0308, respectively, N = 5).

### *Breast Cancer Xenograft In Vivo-Ex Vivo Studies*

Representative images of a comparison between *in vivo* and *ex vivo* DTI data from the same tumor are shown in Figure 6. A good spatial co-localization of ADC and FA features between *in vivo* and *ex vivo* images is evident from these representative images (Figure 6A-H). Comparisons were made for aDW images *in vivo* and *ex vivo* in Figure 6A, E, respectively, ADC maps *in vivo* and *ex vivo* in Figure 6B, F, respectively, FA maps *in vivo* and *ex vivo* in Figure 6C, G, respectively, and water diffusion directionality *in vivo* and *ex vivo* in Figure 6D, H,

respectively. The corresponding optical red fluorescence image and the H&E stained histological section are displayed in Figures 6I and J, respectively. Confirming our earlier data [11], we observed a reduction of Col1 fibers in hypoxic tumor regions as shown in Figures 6K-L. Overlay images of hypoxia (red) with *in vivo* ADC (gray) and FA (gray) maps and *ex vivo* ADC (gray) and FA (gray) maps are shown in Figures 6M-P, respectively.

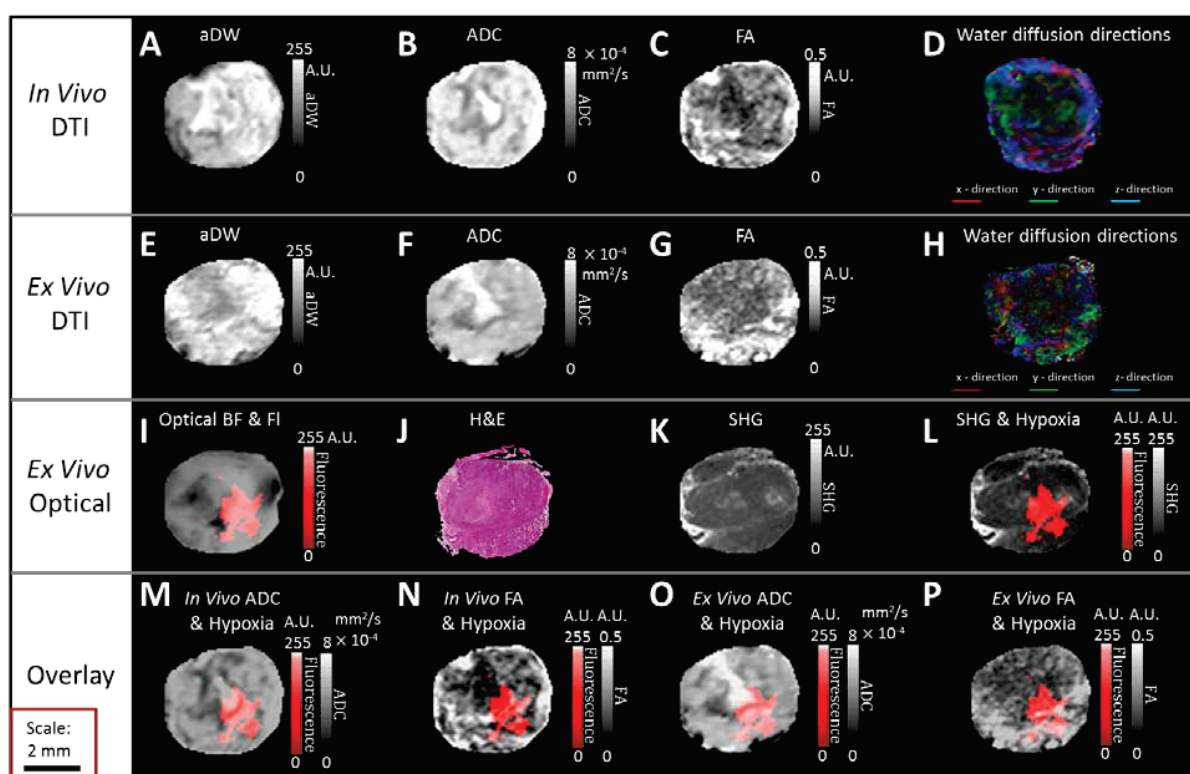


**Figure 6:** Comparison between *in vivo* and *ex vivo* DTI data in breast cancer xenografts. (A-D) Representative *in vivo* DT images of (A) aDW image, (B) ADC map, (C) FA map, and (D) water diffusion directionality color map. Corresponding *ex vivo* DT images of (E) aDW image, (F) ADC map, (G) FA map, and (H) water diffusion directionality color map. *Ex vivo* optical images of (I) hypoxic fluorescing regions, (J) H&E, (K) SHG Col1 fibers, and (L) overlay of SHG Col1 fibers with hypoxic regions. (M-P) Overlay of hypoxic regions (red) with (M) *in vivo* ADC map (gray), (N) *in vivo* FA map (gray), (O) *ex vivo* ADC map (gray), and (P) *ex vivo* FA map (gray).

Quantification of data from four slices obtained from two tumors are summarized in Figure 7 A-D. A strong correlation (Co-relation coefficient = 0.80) was observed between spatially co-localized *in vivo* and *ex vivo* ADC maps as shown in Figure 7A. Similarly, a good correlation (Co-relation coefficient = 0.56) was observed between spatially co-localized *in vivo* and *ex vivo*

FA maps as shown in Figure 7B. Significantly lower ADC values were observed in hypoxic regions as compared to normoxic regions for both *in vivo* and *ex vivo* data (Figure 7C,  $p$ -value < 0.05,  $N = 4$ ). Also, significantly lower FA values were observed in hypoxic regions as compared to normoxic regions for both *in vivo* and *ex vivo* data (Figure 7D,  $p$ -value < 0.04,  $N = 4$ ). The analysis was performed using a paired t-test on four slices per tumor. Significant differences were observed for both tumors but data from only one tumor are presented.

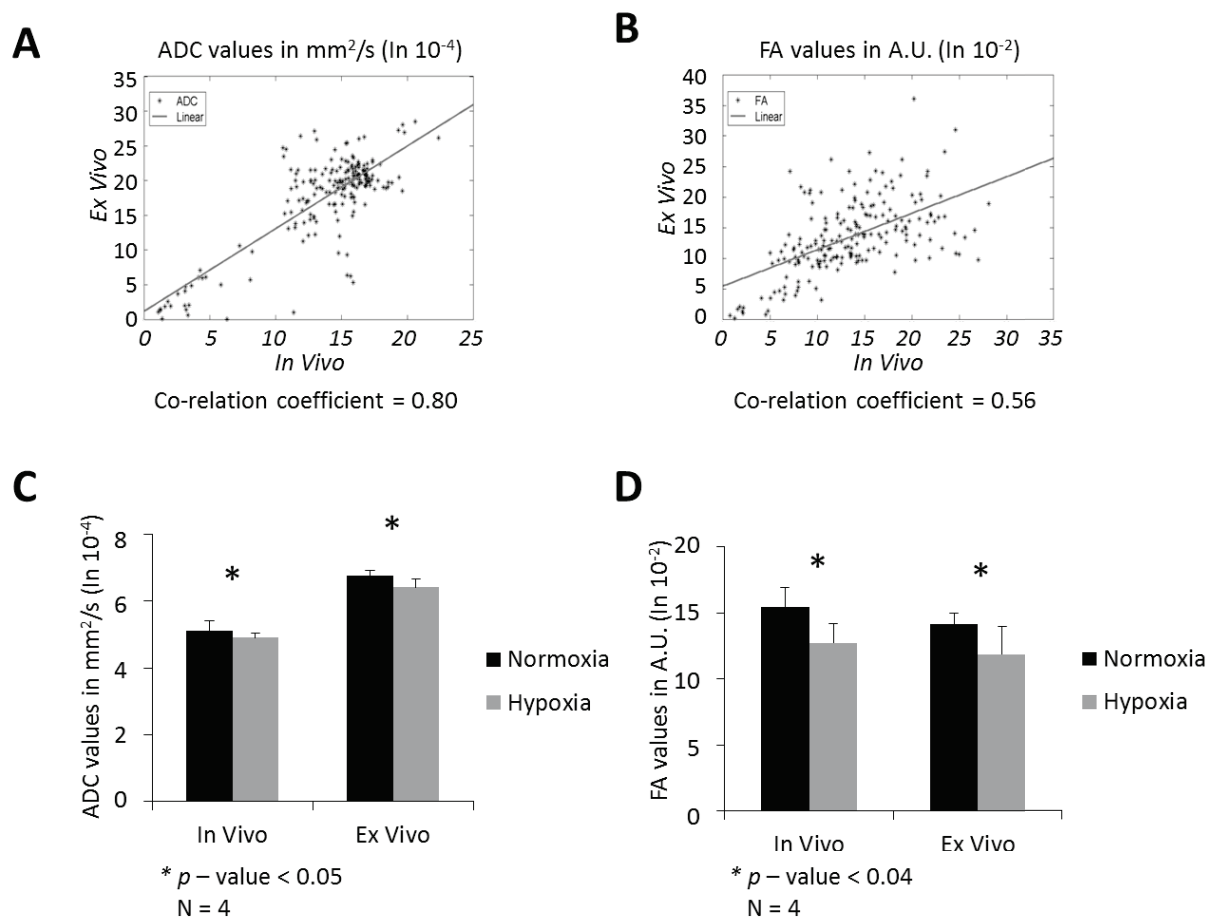


**Figure 7:** Quantification of *in vivo* and *ex vivo* DTI data comparison in breast cancer xenografts. (A) Correlation between spatially co-localized *in vivo* and *ex vivo* ADC maps. (B) Correlation between *in vivo* and *ex vivo* FA maps. Correlations are a composite from all images acquired from two tumors. (C) ADC ( $p$ -value < 0.05,  $N = 4$ ) and (D) FA ( $p$ -value < 0.04,  $N = 4$ ) values were significantly decreased in hypoxic versus normoxic regions quantified from both *in vivo* and *ex vivo* DTI data. Statistical analysis was performed using a paired t-test on four slices per tumor. Significant differences were observed for both tumors but data from only one tumor is presented.

## Discussion

Here we have demonstrated for the first time that Col1 fibers participate in mediating water diffusion and anisotropy. Data obtained from human breast cancers demonstrated that regions with high Col1 fiber content showed significantly increased ADC and FA values, as evident from our fiber content quantification analysis. Within the constraints of our texture analysis approach, we did not detect an influence of fiber textures on ADC and FA values, suggesting that fiber content rather than fiber texture mediates water diffusion. These data suggest that ADC and FA maps may provide noninvasive biomarkers of Col1 fiber density.

*Ex vivo* studies of human breast cancer xenografts further confirmed our observations made in human breast cancer specimens. In this tumor model, hypoxic low Col1 fiber containing regions showed decreased ADC and FA values compared to normoxic regions that had significantly higher percent fiber volume, which was comparable to our findings in human breast cancers in terms of Col1 fiber content. *In vivo* studies in tumor xenografts demonstrated a good agreement of ADC and FA patterns between *in vivo* and *ex vivo* images, supporting that conclusions drawn from *ex vivo* measurements of Col1 fibers, ADC and FA are likely to hold in corresponding *in vivo* measurements. These data also have implication for noninvasive detection of hypoxic regions, which could be deduced from ADC and FA maps obtained *in vivo*, as well as for the delivery of low molecular weight agents with similar polarity and charge as water, which would likely display diffusive patterns that resemble those of water as detected in ADC and FA maps.

Our finding that Col1 fiber density positively correlated with ADC values suggests that Col1 fibers enhance water diffusion in malignant breast cancers that are characterized by high Col1 fiber content [15]. In areas of dense Col1 fibers, we observed an increased fractional anisotropy as detected by DTI. This is in good agreement with two recent DTI studies of human articular cartilage [26], and porcine carotid artery [9], in which the directionality of water diffusion was consistent with the zonal distribution of Col1 fiber orientation. It has been shown that fiber network alignment does not affect the overall diffusion coefficient [27], but only affected diffusion anisotropy. This could be one reason why we did not observe differences in ADC values in different fiber texture patterns.

Recent clinical *in vivo* studies demonstrated that the ADC in breast cancers was significantly lower than that of benign breast lesions and normal breast tissue [10, 28], and is accompanied by decreased FA in cancer *versus* normal tissue [28]. A decrease in the ADC and FA values observed in breast cancer could be due to the presence of hypoxic regions within the tumor, in which Col1 fiber content is significantly lower as previously shown [11]. Our findings suggest that averaging the ADC and FA values in a breast lesion may not provide an accurate assessment for characterizing breast tumors, as information on spatial heterogeneity within the tumor is lost [29].

The results obtained here strongly encourage further investigation of using ADC and FA to noninvasively image Col1 fiber density as well as hypoxia. Additionally, these data extend our earlier studies, which demonstrated that Col1 fibers facilitate macromolecular transport

(Chapter 4) [30]. The results obtained here suggest that transport through the ECM of low molecular weight agents with comparable charge and polarity to water is also mediated by Col1 fibers, with implications for the delivery and transport of low molecular weight chemotherapy agents through the ECM. These results indicate that diffusion MRI may be used to assess Col1 fiber density in breast lesions, which is useful because high Col1 fiber density is a hallmark of malignant breast cancers and can facilitate metastatic dissemination from the primary lesion along Col1 fibers [2].

In conclusion, we have shown that dense and intermediate Col1 fibers in breast cancers can enhance water diffusion and increase diffusion anisotropy. Noninvasive DTI may be used as a surrogate marker to assess Col1 fiber density in breast cancers, which is important because high Col1 fiber density is associated with mammary tumor initiation, progression and metastasis [2]. A decrease in ADC and FA values observed within a lesion could be predictive of hypoxic regions and may contribute to better patient management. Future studies should focus on the dynamic range of ADC and FA that can quantitatively predict Col1 fiber density differences that influence breast cancer progression and metastasis.

### **Acknowledgements**

This work was supported by NIH R01 CA136576, R01 CA138515, R01 CA73850, R01 CA82337, R01 CA154725, R01 CA134695, P50 CA103175, and P30 CA006973. We gratefully acknowledge the expert assistance of Dr. Dmitri Artemov and Dr. Vadappuram Chacko. We

thank Gary Cromwell for maintaining cells and inoculating tumors, and Flonne Wildes for monitoring xenograft growth.

## References

1. Brown, E., T. McKee, E. diTomaso, A. Pluen, B. Seed, Y. Boucher, and R.K. Jain (2003). Dynamic imaging of collagen and its modulation in tumors in vivo using second-harmonic generation. *Nature Medicine*. 9(6): 796-800.
2. Provenzano, P.P., D.R. Inman, K.W. Eliceiri, J.G. Knittel, L. Yan, C.T. Rueden, J.G. White, and P.J. Keely (2008). Collagen density promotes mammary tumor initiation and progression. *BMC Med*. 6: 11.
3. McKee, T.D., P. Grandi, W. Mok, G. Alexandrakis, N. Insin, J.P. Zimmer, M.G. Bawendi, Y. Boucher, X.O. Breakefield, and R.K. Jain (2006). Degradation of fibrillar collagen in a human melanoma xenograft improves the efficacy of an oncolytic herpes simplex virus vector. *Cancer Research*. 66(5): 2509-13.
4. Provenzano, P.P., K.W. Eliceiri, J.M. Campbell, D.R. Inman, J.G. White, and P.J. Keely (2006). Collagen reorganization at the tumor-stromal interface facilitates local invasion. *BMC Med*. 4.
5. Cox, T.R. and J.T. Erler (2011). Remodeling and homeostasis of the extracellular matrix: implications for fibrotic diseases and cancer. *Dis Model Mech*. 4(2): 165-78.
6. Conklin, M.W., J.C. Eickhoff, K.M. Ricking, C.A. Pehlke, K.W. Eliceiri, P.P. Provenzano, A. Friedl, and P.J. Keely (2011). Aligned Collagen Is a Prognostic Signature

- for Survival in Human Breast Carcinoma. *American Journal of Pathology*. 178(3): 1221-1232.
7. Mohler, W., A.C. Millard, and P.J. Campagnola (2003). Second harmonic generation imaging of endogenous structural proteins. *Methods*. 29(1): 97-109.
  8. Mori, S. and J.Y. Zhang (2006). Principles of diffusion tensor imaging and its applications to basic neuroscience research. *Neuron*. 51(5): 527-539.
  9. Ghazanfari, S., A. Driessen-Mol, G.J. Strijkers, F.M. Kanters, F.P. Baaijens, and C.V. Bouten (2012). A comparative analysis of the collagen architecture in the carotid artery: second harmonic generation versus diffusion tensor imaging. *Biochem Biophys Res Commun*. 426(1): 54-8.
  10. El Khouli, R.H., M.A. Jacobs, S.D. Mezban, P. Huang, I.R. Kamel, K.J. Macura, and D.A. Bluemke (2010). Diffusion-weighted Imaging Improves the Diagnostic Accuracy of Conventional 3.0-T Breast MR Imaging. *Radiology*. 256(1): 64-73.
  11. Kakkad, S.M., M. Solaiyappan, B. O'Rourke, I. Stasinopoulos, E. Ackerstaff, V. Raman, Z.M. Bhujwalla, and K. Glunde (2010). Hypoxic Tumor Microenvironments Reduce Collagen I Fiber Density. *Neoplasia*. 12(8): 608-617.
  12. Cailleau, R., R. Young, M. Olive, and W.J. Reeves (1974). Breast Tumor-Cell Lines from Pleural Effusions. *Journal of the National Cancer Institute*. 53(3): 661-674.
  13. Glunde, K., C. Jie, and Z.M. Bhujwalla (2004). Molecular causes of the aberrant choline phospholipid metabolism in breast cancer. *Cancer Research*. 64(12): 4270-4276.
  14. Krishnamachary, B., M.F. Penet, S. Nimmagadda, Y. Mironchik, V. Raman, M. Solaiyappan, G.L. Semenza, M.G. Pomper, and Z.M. Bhujwalla (2012). Hypoxia



- Regulates CD44 and Its Variant Isoforms through HIF-1 alpha in Triple Negative Breast Cancer. *PLoS One*. 7(8).
15. Kakkad, S.M., M. Solaiyappan, P. Argani, S. Sukumar, L.K. Jacobs, D. Leibfritz, Z.M. Bhujwalla, and K. Glunde (2012). Collagen I fiber density increases in lymph node positive breast cancers: pilot study. *J Biomed Opt*. 17(11): 116017.
  16. Castellano, G., L. Bonilha, L.M. Li, and F. Cendes (2004). Texture analysis of medical images. *Clinical Radiology*. 59(12): 1061-1069.
  17. Haralick, R.M., Shanmuga.K, and I. Dinstein (1973). Textural Features for Image Classification. *Ieee Transactions on Systems Man and Cybernetics*. Smc3(6): 610-621.
  18. Bezdek, J.C., *Pattern recognition with fuzzy objective function algorithms*. Advanced applications in pattern recognition 1981, New York: Plenum Press. xv, 256 p.
  19. Aggarwal, M., S. Mori, T. Shimogori, S. Blackshaw, and J. Zhang (2010). Three-dimensional diffusion tensor microimaging for anatomical characterization of the mouse brain. *Magn Reson Med*. 64(1): 249-61.
  20. Jiang, H.Y., P.C.M. van Zijl, J. Kim, G.D. Pearlson, and S. Mori (2006). DtiStudio: Resource program for diffusion tensor computation and fiber bundle tracking. *Computer Methods and Programs in Biomedicine*. 81(2): 106-116.
  21. Collignon, A., F. Maes, D. Delaere, D. Vandermeulen, P. Suetens, and G. Marchal (1995). Automated multi-modality image registration based on information theory. *Information Processing in Medical Imaging*. 3: 263-274.
  22. Dice, L.R. (1945). Measures of the Amount of Ecologic Association between Species. *Ecology*. 26(3): 297-302.

23. Budde, M.D., L. Janes, E. Gold, L.C. Turtzo, and J.A. Frank (2011). The contribution of gliosis to diffusion tensor anisotropy and tractography following traumatic brain injury: validation in the rat using Fourier analysis of stained tissue sections. *Brain*. 134(Pt 8): 2248-60.
24. Dunn, J.C. (1973). A Fuzzy Relative of the ISODATA Process and Its Use in Detecting Compact Well-Separated Clusters. *Journal of Cybernetics*. 3(3): 32-57.
25. Miyamoto, S., H. Ichihashi, and K. Honda (2008). Algorithms for Fuzzy Clustering Methods in c-Means Clustering with Applications Introduction. *Algorithms for Fuzzy Clustering: Methods in C-Means Clustering with Applications*. 229: 1-+.
26. Deng, X., M. Farley, M.T. Nieminen, M. Gray, and D. Burstein (2007). Diffusion tensor imaging of native and degenerated human articular cartilage. *Magn Reson Imaging*. 25(2): 168-71.
27. Stylianopoulos, T., B. Diop-Frimpong, L.L. Munn, and R.K. Jain (2010). Diffusion anisotropy in collagen gels and tumors: the effect of fiber network orientation. *Biophys J*. 99(10): 3119-28.
28. Partridge, S.C., A. Ziadloo, R. Murthy, S.W. White, S. Peacock, P.R. Eby, W.B. DeMartini, and C.D. Lehman (2010). Diffusion tensor MRI: preliminary anisotropy measures and mapping of breast tumors. *J Magn Reson Imaging*. 31(2): 339-47.
29. Marusyk, A., V. Almendro, and K. Polyak (2012). Intra-tumour heterogeneity: a looking glass for cancer? *Nature Reviews Cancer*. 12(5): 323-334.
30. Kakkad, S.M., M.-F. Penet, A. Akhbardeh, A.P. Pathak, M. Solaiyappan, V. Raman, D. Leibfritz, K. Glunde, and Z.M. Bhujwalla (2013). Hypoxic tumor environments exhibit

disrupted collagen I fibers and low macromolecular transport. *PLoS One*. 2013 Dec 12;8(12)

**Curriculum vitae**

Born 7<sup>th</sup> January 1984 in Mumbai, India

**Education:**

10/2010 - 10/2013 Doctoral thesis under supervision of Prof. Dr. Dieter Leibfritz  
University of Bremen, Germany

10/2006 - 12/2007 Masters in Science  
New Jersey Institute of Technology (NJIT), New Jersey, USA

10/2002 – 06/2006 Bachelors in Engineering (Biomedical engineering)  
D. J. Sanghvi College of Engineering, Mumbai University, India

**Experience:**

06/2008 - 10/2013 Research scientist under supervision of Dr. Zaver Bhujwalla

01/2007 - 12/2007 Research assistant under supervision of Dr. Bharat Biswal

06/2007 - 12/2007 Teaching assistant in the laboratory of Dr. Bharat Biswal

**List of publications**

Shah T, Wildes F, Penet MF, Winnard PT Jr, Glunde K, Artemov D, Ackerstaff E, Gimi B, **Kakkad S**, Raman V, Bhujwalla ZM. Choline kinase overexpression increases invasiveness and drug resistance of human breast cancer cells. *NMR Biomed*. 2010 Jul;23(6):633-42. doi: 10.1002/nbm.1510.3.

**Kakkad SM**, Solaiyappan M, O'Rourke B, Stasinopoulos I, Ackerstaff E, Raman V, Bhujwalla ZM, Glunde K. Hypoxic tumor microenvironments reduce collagen I fiber density. *Neoplasia*. 2010 Aug;12(8):608-17.

Stasinopoulos I, Penet MF, Chen Z, **Kakkad S**, Glunde K, Bhujwalla ZM. Exploiting the tumor microenvironment for theranostic imaging. *NMR Biomed*. 2011 Jul;24(6):636-47. Review.

Shah T, Stasinopoulos I, Wildes F, **Kakkad S**, Artemov D, Bhujwalla ZM. Noninvasive imaging identifies new roles for cyclooxygenase-2 in choline and lipid metabolism of human breast cancer cells. *NMR Biomed*. 2012 May;25(5):746-54.

**Kakkad SM**, Solaiyappan M, Argani P, Sukumar S, Jacobs LK, Leibfritz D, Bhujwalla ZM, Glunde K. Collagen I fiber density increases in lymph node positive breast cancers: pilot study. *J Biomed Opt*. 2012 Nov;17(11):116017.

Penet MF, Chen Z, **Kakkad S**, Pomper MG, Bhujwalla ZM. Theranostic imaging of cancer. *Eur J Radiol*. 2012 Sep;81 Suppl 1:S124-6.

**Kakkad, S.M.**, M.-F. Penet, A. Akhbardeh, A.P. Pathak, M. Solaiyappan, V. Raman, D. Leibfritz, K. Glunde, and Z.M. Bhujwalla. Hypoxic tumor environments exhibit disrupted collagen I fibers and low macromolecular transport. *PLoS One*. 2013 Dec 12;8(12).

**Kakkad, S.M.**, J. Zhang, A. Akhbardeh, D. Jacob, M. Solaiyappan, M. Jacobs, V. Raman, D. Leibfritz, K. Glunde, and Z.M. Bhujwalla. Collagen fibers influence water diffusion and anisotropy. *Journal of the National Cancer Institute*. (Manuscript in preparation).